THE UNIVERSITY *of* EDINBURGH

Planet Formation in Self-Gravitating Discs

Peter Gibbons

Doctor of Philosophy
The University of Edinburgh
2013

Abstract

The work performed here studies particle dynamics in local two-dimensional simulations of self-gravitating accretion discs with a simple cooling law. It is well known that the structure which arises in the gaseous component of the disc due to a gravitational instability can have a significant effect on the evolution of dust particles. Previous results using global simulations indicate that spiral density waves are highly efficient at collecting dust particles, creating significant local over-densities which may be able to undergo gravitational collapse. This thesis expand on these findings, using a range of cooling times to mimic the conditions at a large range of radii within the disc. The PENCIL Code is used to solve the 2D local shearing sheet equations for gas on a fixed grid together with the equations of motion for solids coupled to the gas solely through aerodynamic drag force. The work contained here shows that spiral density waves can create significant enhancements in the surface density of solids, equivalent to 1-10cm sized particles in a disc following the profiles of Clarke (2009) around a solar mass star, causing it to reach concentrations several orders of magnitude larger than the particles mean surface density. These findings suggest that the density waves that arise due to gravitational instabilities in the early stages of star formation provide excellent sites for the formation of large, planetesimal-sized objects. These results are expanded on, with subsequent results introducing the effects of the particles self-gravity showing these concentrations of particles can gravitationally collapse, forming bound structures in the solid component of the disc.

Lay Summary

The core accretion model of planet formation models planet growth through a bottom up process, where collisions between particles result in growth, which leads to the formation of large kilometre size objects, often referred to as planetesimals. The details of this process are unfortunately not well understood at present, and there are several obstacles which a successful theory of planet formation must overcome in this growth regime. In order to form kilometre size objects, collisions between particles must remain constructive. This is not a problem for small particles, where the energies involved are low, however objects with radii of around 1m, which typically travel at velocities of tens of meters per second, it is not clear how collisions lead to growth. During this period of growth, small bodies within the disc will feel a strong headwind from the gas in the disc, which travels at lower orbital speeds. This causes the bodies to fall inward toward the star. The timescale this process occurs on is relatively short, suggesting that this period of growth must be rapid. The growth time scale must also be rapid to allow for the growth of giant planets within disc lifetimes.

The work contained in this thesis attempts to explain the mechanisms which enable the formation of these large bodies, known as planetesimals. In massive discs, the gravity of the disc causes instabilities, which leads to the formation of density waves in the disc. This structure traps small dust particles, causing local concentrations of solid material. These concentrations can be very large, as large as 1,000 times larger than the mean particle density, at which point the gravitational forces between particles are sufficient to cause the dust particles to gravitationally collapse, resulting in gravitationally bound solid structures comparable to large asteroids, or even dwarf planets.

Declaration

I declare that this thesis was composed by myself, that the work contained herein is my own except where explicitly stated otherwise in the text, and that this work has not been submitted for any other degree or professional qualification except as specified.

Parts of this work have been published in Gibbons et al. (2012).

(*Peter Gibbons, 2013*)

Acknowledgements

I would like to thank everyone who has helped me in one way or another during the course of my Ph.D. Firstly I would like to thank my supervisor Ken Rice, who has been an invaluable guide in my studies over the course of my degree and I am extremely grateful for the lessons and assistance received from him during this period of time. In addition I would like to thank the remaining members of our research group, Duncan Forgan and George Mamatsashvili, who provided much support and interesting discussion throughout my studies.

I would also like to thank Bob Mann and Avery Meiksen, my end of year examiners, for the advice they have provided throughout the course of my studies, as well as my viva examiners Anders Johansen and Sadegh Kochfar, for making the viva process as enjoyable as possible! I also thank the Graduate School Secretary Jane Patterson and the IfA Teaching Secretary Paula Wilkie for helping me out with all the forms! I would also like to thank all my office mates from the IfA, particularly Jack, Victoria, Alasdair and Vinod, for helping me stay sane during my time there and providing no end of distractions!

I must also take the opportunity to thank everyone at the karate club for their support and friendship during my time here, in particular my teachers Ger O'Dea, Kaicho Amor and Coach Torres who have taught me more than I could have imagined when I first arrived here. I would also like to thank my fellow coaches at the club Dave Orr, Paul Skelding and Jason O'Toole, along with my training partners and fellow teammates Diarmuid Lloyd, Andrew Rosevear, Zachary Janes, Joe Farrimond, Yusuke Onishi, Laurence Cohen and Bogdan Trimbitas, along with everyone else who I don't have the space to mention here.

Last but not least, I would like to thank my friends and family back home in Shrewsbury for all their support during my Studies, without whom I wouldn't be where I am today.

Contents

Abstract i

Lay Summary ii

Declaration iii

Acknowledgements iv

Contents v

List of Figures x

1 Introduction 1

1.1 Circumstellar Disc Formation 1

1.2 Structure of Circumstellar Discs 5

1.2.1 Disc Mass 5

1.2.2 Disc Size 8

1.3 Disc Dynamics 9

1.3.1 Gravitational Instability 15

1.3.2 Vortices 20

1.3.3 Magneto-rotational Instability 22
1.4 Planet Formation in Discs 24
1.4.1 Dust Grain Evolution 25
1.4.2 Planetesimal Evolution 31
1.4.3 Gas Giant Formation 34
1.5 Migration 37
1.5.1 Impulse Approximation 37
1.5.2 Resonant Torques 41
1.5.3 Types of Migration 42
1.5.4 Consequences of Migration 46
1.6 Summary 47

2 Model 49

2.1 Hydrodynamics and the Shearing Sheet Approximation 49
2.2 The Pencil Code 52
2.2.1 Spatial Derivatives 53
2.2.2 Viscosity and Diffusion 53
2.2.3 Shocks 54
2.2.4 Particles 55
2.2.5 Time Step 57
2.2.6 Poisson Equation 58

3 Particle Trapping in Self-Gravitating Discs 60

3.1 Introduction 60

3.2 Model 64

3.2.1 Gas Density 65

3.2.2 Gas Velocity 66

3.2.3 Self-gravity 67

3.2.4 Entropy 67

3.2.5 Dust Particles 67

3.2.6 Units and Initial Conditions 68

3.3 Results 70

3.3.1 Gas Evolution 70

3.3.2 Particle Concentration 70

3.3.3 Particle Velocities 81

3.3.4 Effects of Radial Drift 85

3.4 Discussion and Conclusions 86

4 Planetesimal Formation in Spiral Density Waves 89

4.1 Introduction 89

4.2 Model 92

4.2.1 Gas Velocity 93

4.2.2 Dust Particles 94

4.2.3 Units and Initial Conditions 95

4.3 Results 96
4.3.1 Gas Evolution 96
4.3.2 Particle Concentration 97
4.4 Discussion and Conclusions 110

5 Particle Trapping by Vortices in Self-gravitating Discs 113

5.1 Introduction 113
5.2 Model 115
5.2.1 Units and Initial Conditions 116
5.3 Results 116
5.3.1 Gas Evolution 116
5.3.2 Particle Concentration 117
5.4 Conclusion 128

6 3D Shearing Boxes 131

6.1 Introduction 131
6.2 Model 133
6.2.1 Gas Density 134
6.2.2 Gas Velocity 134
6.2.3 Entropy 135
6.2.4 Self-gravity 136
6.2.5 Units and Initial Conditions 136
6.3 Progress to Date 137

7 Conclusion & Discussion 141

Bibliography 146

List of Figures

(1.1) Classification and basic properties of Young Stellar Objects (YSOs) 3

(1.2) Representation of an accretion disc around central object divided into a series of anulli. 11

(1.3) Evolution of the surface density of an initially thin ring of material initially located at a radius r_0 spreading under the action of a constant viscosity, ν. Each curve shows the surface density profile of the ring as the non-dimensional time parameter $\tau = 12\nu r_o^{-2} t$ increases. Figure adapted from Armitage (2010) 12

(1.4) Surface density structure of a self-gravitating disc in both global (left) and local (right) simulations. In both images we see strong density wave structure present as a result of self-gravity. 16

(1.5) Potential outcomes of a disc unstable to self-gravity. the left hand image shows a disc which has undergone fragmentation, the right hand image has settled into a quasi-steady state, developing spiral density waves. 16

(1.6) The radial drift velocity of particles as a function of stopping time for a typical protoplanetary disc. Very small particles drift inwards at constant rate,which starts to increase for intermediate size objects, reaching a maximum at $\tau_f = 1$, larger particles decouple from the disc and the drift rate falls. Figure adapted from Armitage (2010) 29

(1.7) Timescale for radial drift for meter-sized particles ($\tau_f \sim 1$) as a function of radius for a range of disc scale heights. 30

(1.8) Growth timescale as a function of object mass for collisional growth and Bondi accretion. Small dust grain's growth is dominated by collisions with other particles, however larger objects will tend to grow via accretion of material from the disc. 31

(1.9) Outcomes of a collision between two objects (Armitage, 2010). . . 32

(1.10) Gravitational focusing 33

(1.11) The evolution of core mass (solid line) and total planet mass (dashed line) for an object at 5.2AU in a simplified version of the Pollack core accetion simulation from Rice et al. (2003). 36

(1.12) A parcel of gas of mass m passes by a planet with an impact parameter (distance of closest approach) b and a relative velocity Δv. 38

(1.13) A low mass planet interacting with the gaseous disc. We see a faint spiral structure in the disc due to the presence of the planet, however the planet does not cause any major change to the structure in the disc. The plot in the lower left hand corner shows the surface density profile within the disc. Figure taken from Armitage (2010) 43

(1.14) A high mass planet of mass $M \sim M_J$ interacting with the disc. Here the spiral structure emanating from the planet is much more pronounced than in the low mass case. In addition to this the structure of the disc has been drastically altered by the planets presence, with a gap starting to open up around planets orbit. Figure taken from Armitage (2010) 44

(2.1) Illustration of the local coordinate frame (x,y) used in the shearing sheet approximation, which co-rotates with the disc matter at the distance r_0 with velocity $r_0\Omega$. In this local frame, the discs Keplerian differential rotation appears as a parallel azimuthal shear flow $u_0 = (0, -q\Omega x)$. 51

(3.1) Logarithmic surface density of the gas after 40 orbits in the $t_c = 10\Omega^{-1}$ run. At this stage the disc is already in a quasi-steady state. 71

(3.2) Logarithmic surface density of the $\tau_f = 0.01\Omega^{-1}$ and $\tau_f = 0.1\Omega^{-1}$ particles for the $t_c = 10\Omega^{-1}$ run at $t = 40T$, when the disc is already in a quasi-steady state. 72

(3.2) **(Continued)** Logarithmic surface density of the $\tau_f = 1.0\Omega^{-1}$ and $\tau_f = 10.0\Omega^{-1}$ particles for the $t_c = 10\Omega^{-1}$ run at $t = 40T$, when the disc is already in a quasi-steady state. 73

(3.2) **(Continued)** Logarithmic surface density of the $\tau_f = 100.0\Omega^{-1}$ particles and the combined particle surface density for the $t_c = 10\Omega^{-1}$ run at $t = 40T$, when the disc is already in a quasi-steady state, or 30 after the drag force between the gas and particles has been turned on. The surface density of gas at this time is shown in Figure 1. From these panels we see that intermediate-sized particles with $\tau_f \sim 1.0\Omega^{-1}$ are captured most effectively in density structures. 74

(3.3) Maximum particle density, relative to the mean, as a function of time for a range of friction times in the $t_c = 10\Omega^{-1}$ simulation. Particles with $\tau_f = 1.0\Omega^{-1}$ exhibit the highest degree of concentration in gas over-densities. 77

(3.4) Maximum particle density, relative to the mean, as a function of time for a range of cooling times. Particles are somewhat more effectively concentrated in spiral density waves at short cooling times, with the $t_c = 80\Omega^{-1}$ and the $t_c = 160\Omega^{-1}$ simulations showing a decrease in particle concentration than the shorter times considered. 78

(3.5) Analytically derived profile for t_c as a function of radius for different mass accretion rates. The effective cooling times we consider here correspond to the radial range $\sim 20 - 60$AU. 79

(3.6) Histograms showing the spread of particle velocities, relative to the initial sound speed, for each friction time at the end of the $t_c = 10$ simulation. As the friction time lengthens, the distribution of velocities narrows due to the diminishing effect of the drag force. The peak of the distribution also tends to occur at lower velocities. 83

(3.7) Histograms showing the spread of the $\tau_f = 1$ particles velocities, relative to the initial sound speed, at the end of our simulations for the four shortest cooling times considered. As the cooling time lengthens, the distribution of particle velocities narrows, with the peak of the distribution occurring at smaller velocities. 84

(3.8) Maximum particle density, relative to the mean, against time for a range of drift values, $\Delta v = 0.0, 0.02, 0.05$ and 0.5 for cooling time $t_c = 20\Omega^{-1}$. Even in the presence large amounts of radial drift, there are still significant over-densities in the particle density field due to the gravitational instabilities. 85

(4.1) Surface density of the gas (top) and particles (bottom) in the low mass ($\Sigma_p = 10^{-3}\Sigma_0$), $t_c = 10\Omega^{-1}$ simulation. The dust particles are collected in the density waves that form due to gravitational instabilities in the gas. 98

(4.2) Surface density of the gas (top) and particles (bottom) in the standard $t_c = 10\Omega^{-1}$ simulation. As a result of the particles' gravitational interaction with each other bound clumps of particles form within the spiral density waves. If these clumps reach high enough densities the back reaction on the gas results in the wake of the clumps motion becoming visible in the gas. 99

(4.3) Surface density of the gas (top) and particles (bottom) in the $t_c = 20\Omega^{-1}$ simulation. As a result of the particles' gravitational interaction with each other bound clumps of particles form within the spiral density waves. If these clumps reach high enough densities the back reaction on the gas results in the wake of the clumps motion becoming visible in the gas. 100

(4.4) Surface density of the gas (top) and particles (bottom) in the $t_c = 40\Omega^{-1}$ simulation. As a result of the particles' gravitational interaction with each other bound clumps of particles form within the spiral density waves. If these clumps reach high enough densities the back reaction on the gas results in the wake of the clumps motion becoming visible in the gas. 101

(4.5) Surface density of the gas (top) and particles (bottom) in the $t_c = 80\Omega^{-1}$ simulation. As a result of the particles' gravitational interaction with each other bound clumps of particles form within the spiral density waves. If these clumps reach high enough densities the back reaction on the gas results in the wake of the clumps motion becoming visible in the gas. 102

(4.6) Logarithmic surface density of the $\tau_f = 0.01\Omega^{-1}$ and $\tau_f = 0.1\Omega^{-1}$ particles in the top right corner of the $t_c = 10\Omega^{-1}$ run at $t = 40T$, when the disc is already in a quasi-steady state, or 30 orbits after the drag force between the gas and particles has been turned on. . 104

(4.6) **(Continued)**Logarithmic surface density of the $\tau_f = 1.0\Omega^{-1}$ and $\tau_f = 10.0\Omega^{-1}$ particles in the top right corner of the $t_c = 10\Omega^{-1}$ run at $t = 40T$, when the disc is already in a quasi-steady state, or 30 orbits after the drag force between the gas and particles has been turned on. 105

(4.6) **(Continued)**Logarithmic surface density of the $\tau_f = 100.0\Omega^{-1}$ particles and total particle surface density in the top right corner of the $t_c = 10\Omega^{-1}$ run at $t = 40T$, when the disc is already in a quasi-steady state, or 30 orbits after the drag force between the gas and particles has been turned on. We clearly see a number of highly dense structures which are gravitationally bound. these structure are primarily made up of $\tau_f = 0.1\Omega^{-1}$ and $\tau_f = 1.0\Omega^{-1}$ particles. 106

(4.7) Maximum surface density of the dust particles within the sheet, as a function of time, for each cooling time. There is little correlation between cooling time and the maximum surface density reached, suggesting the particles self-gravity can enable significant density enhancements, even for longer cooling times 108

(4.8) Mass of the largest gravitationally bound collection of particles within the sheet, as a function of time, for each cooling time. The shorter cooling times tend to produce more massive particle clumps, with the shortest cooling time considered 109

(4.9) Number of gravitationally bound concentrations of particles in the sheet over time for each cooling time 109

(4.10) Total mass of gravitationally bound concentrations of particles in the sheet over time for each cooling time 110

(5.1) Surface Density of the gas at the end of the massless particle run. The Potential Vorticity field of the simulation at this time is shown in Figure 5.2, the dust particles are shown in Figure 5.3. 118

(5.2) Potential Vorticity field at the end of the simulation with massless particles. The colourmap is restricted to the range -10 to $+10$ to emphasise the presence of vortex structure. 118

(5.3) Logarithmic surface density of the $\tau_f = 0.01\Omega^{-1}$ and $\tau_f = 0.1\Omega^{-1}$ particles at the end of the massless particle run. 121

(5.3) **(Continued)** Logarithmic surface density of the $\tau_f = 1.0\Omega^{-1}$ and $\tau_f = 10.0\Omega^{-1}$ particles at the end of the massless particle run. . . 122

(5.3) **(Continued)** Logarithmic surface density of the $\tau_f = 100.0\Omega^{-1}$ particles and the combined particle surface density for the massless particle run. The surface density of gas at this time is shown in Figure 1 and the vorticity field is shown From these panels we see that intermediate-sized particles are captured effectively in density waves, preferentially surrounding anti-cyclonic vortices. 123

(5.4) Logarithmic surface density of the $\tau_f = 0.01\Omega^{-1}$ and $\tau_f = 0.1\Omega^{-1}$ particles at the end of the massive ($\Sigma_p = 10^{-2}\Sigma_0$) particle run. . . 125

(5.4) **(Continued)** Logarithmic surface density of the $\tau_f = 1.0\Omega^{-1}$ and $\tau_f = 10.0\Omega^{-1}$ particles at the end of the massive ($\Sigma_p = 10^{-2}\Sigma_0$) particle run. 126

(5.4) **(Continued)** Logarithmic surface density of the $\tau_f = 100.0\Omega^{-1}$ particles and the combined particle surface density for the massive ($\Sigma_p = 10^{-2}\Sigma_0$) particle run. As a result of the augmented particle concentration, gravitationally bound clumps of particles form within the structures present on the gaseous component of the disc. 127

(5.5) Maximum surface density of the particles within the sheet as a function of time for both simulations performed. 128

(5.6) Logarithmic surface density of the $\tau_f = 0.1\Omega^{-1}$ and $\tau_f = 1.0\Omega^{-1}$ particles seven orbits after the dust particles are released in the massive ($\Sigma_p = 10^{-2}\Sigma_0$) particle run. This is two orbits after the particle self-gravity term is introduced. The most dense particle structures appear to preferentially form from the rings which develop around vortices. 129

(6.1) Surface density of the gas in the $t_c = 3\Omega^{-1}$ simulation. The top image shows the $x - y$ plane averaged over z, whilst the bottom two images show $x - z$ and $y - z$ cross-sections. 139

(6.2) Surface density of the gas in the $t_c = 10\Omega^{-1}$ simulation. The top image shows the $x - y$ plane averaged over z, whilst the bottom two images show $x - z$ and $y - z$ cross-sections. 140

Chapter 1

Introduction

1.1 Circumstellar Disc Formation

Planets form from protoplanetary discs made up of dust and gas that are observed to form around young stars during the star formation process. Stars form when the gas that exists in giant molecular clouds undergoes gravitational collapse. These molecular clouds are relatively cool, diffuse structures, consisting primarily of H_2 gas with particle number densities $n \sim 10^5 \mathrm{cm}^2$. Within molecular clouds, stars form from over-dense regions known as molecular cloud cores. As a typical core in a molecular cloud starts to collapse under its own gravity, it contracts from an initial size of $\sim$ 0.1pc to that comparable to the solar system ($\sim$ 100AU). As these molecular clouds initially possess nonzero angular momentum, the collapsing core will tend to form a disc around the growing star. Observations by Goodman et al. (1993) estimated that molecular cloud cores rotate uniformly with angular velocity $\sim 10^{-13}\mathrm{s}^{-1}$. For a typical core of radius 0.1pc, with a mass of $M_\odot$, the angular momentum of the cloud is several orders of magnitude greater than that of the solar system. This much angular momentum within the system requires that a significant portion of the material in the collapsing cloud will form a disc, as the cloud collapses parallel to the net angular momentum vector, **J**, of the cloud, whilst the angular momentum of the cloud prevents collapse perpendicular to **J**. In order for material to continue to move inward and be

accreted onto the growing star, angular momentum needs to be transported from the inner regions of the disc outward.

This early collapse phase relates to Class 0 & Class I Young Stellar Objects (YSOs) (Figure 1.1). YSOs are classified based on the infra-red part of the spectral energy distribution (SED) of the object via the parameter,

$$\alpha_{IR} \equiv \frac{\Delta \log(\lambda F_\lambda)}{\Delta \lambda}. \tag{1.1}$$

Objects are generally divided up into different classes based on the value of α_{IR} as follows (Armitage, 2010).

- **Class 0** sources are typically objects very early in the collapse phase (top image of Figure 1.1), where the bulk of their emission is in the far IR and mm part of the spectrum, with little to no flux from the near-IR part of the spectrum ($\alpha_{IR} \sim 0$). Any protostar present within the molecular cloud is still shrouded by gas and dust.

- **Class I** sources are objects where the envelope of gas and dust, while still present, is no longer thick enough to obscure the central object (second image of Figure 1.1). There is a disc of rotationally supported material present. The SED between near and mid-IR has $\alpha_{IR} > -0.3$.

- **Class II** sources represent what are classically known as T Tauri stars. The gaseous envelope has been almost entirely accreted onto the circumstellar disc (third image of Figure 1.1). Sources of this class lie in the range $-1.6 < \alpha_{IR} < -0.3$.

- **Class III** sources are the final evolutionary stage YSOs pass through before becoming a main sequence star. There is little or no disc material remaining (fourth image of Figure 1.1), resulting in an IR SED similar to that of a stellar photosphere, with little or no IR emission, $\alpha_{IR} < -1.6$.

Through this classification scheme we can build up a picture of how circumstellar discs form around protostars in molecular clouds. During the initial collapse phase, whilst the mass of the protostar is still relatively small, the disc mass is

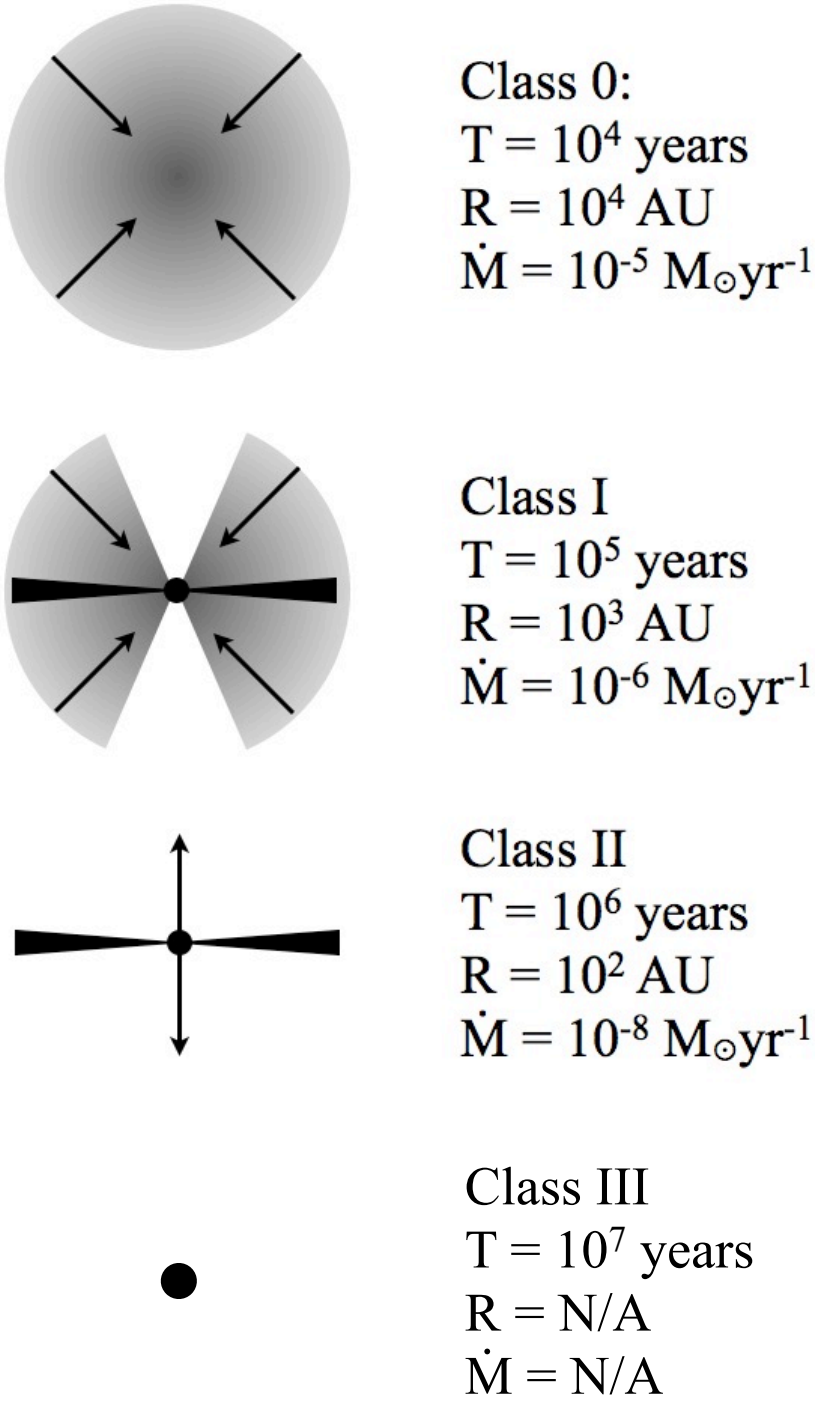

Figure 1.1 *Classification and basic properties of Young Stellar Objects (YSOs)*

comparable to the central objects mass. At this stage, the disc is susceptible to gravitational instabilities, which can have a significant effect on the evolution of the disc, particularly in the role of planet formation. Whilst the disc is massive, self-gravity can dominate the discs dynamics, and is thought to be crucial in the transportation of angular momentum outward (Forgan et al., 2011), subsequently leading to mass transport inward, allowing the central protostar to continue to accrete mass. It is during this stage, where the accretion rate is highest ($\dot{M}_* = 10^{-4}-10^{-6} M_\odot \mathrm{yr}^{-1}$) that the central object grows fastest. This evolutionary phase relates to the Class 0 and Class I sources observed. This phase lasts $\sim 10^4 - 10^5$ years. As material is accreted from the disc onto the growing protostar, the disc mass starts to become negligible compared to the central objects mass, resulting in the effects of the discs self-gravity also becoming negligible as the dynamics of the disc become dominated by the protostars gravity. As the effects of disc self-gravity decline, angular momentum is no longer efficiently transported through the disc, resulting in the mass accretion rate of the protostar dropping from $\sim 10^{-4} - 10^{-6} M_\odot \mathrm{yr}^{-1}$ to $\sim 10^{-7} - 10^{-9} M_\odot \mathrm{yr}^{-1}$. At this point the source enters the Class II phase, the gaseous envelope around the star and disc is almost entirely depleted, resulting in little infall of material, resulting in low accretion rates. The disc is a small fraction of the central objects mass (M_{disc} is typically no more than a few percent of the central objects mass), and is entirely dynamically supported. Such discs are often referred to as protoplanetary discs, as it is thought that at this stage that the disc is a prime location for the formation and evolution of a planetary system. Finally, after a period of several Myrs, any remaining gas in the disc disperses over a period of $\sim 10^4$yrs, leaving a relic debris disc, composed of rocks and pebbles left over from the planet formation process. The main mechanism for the dispersal of the gas in the disc is photoevaporation, ultraviolet light from the central star heats the gas, allowing it to escape from the disc into space. The timescales for this process have been observationally inferred, as very few protoplanetary discs are seen to be older than 10Myrs. By this point, the source has reached the Class III stage, where the formation of the star and accompanying planetary system have ceased.

1.2 Structure of Circumstellar Discs

Here the basic physical properties of circumstellar accretion discs throughout their evolution from the collapse/Class 0 stage, through to the dispersion of the bulk of the disc at the end of the Class II stage and the resulting debris disc around Class III protostars are outlined. These accretion discs are typically observed in a number of ways:

- Detection of infrared excess in the near-/mid-IR. Such a detection indicates the presence of warm dust close (typically no more than $\sim$ 1AU) to the star.
- Detection of an excess of ultraviolet radiation, Hα emission (with a large linewidth), along with certain other emission lines are all indicators of gas being accreted onto the star.
- Observations of mm/sub-mm flux indicate cool dust in the outer regions of the disc
- Direct imaging of the disc, either via scattered, viable light from the parent star, or against a bright background nebula.
- Line emission from molecules, e.g. CO or NH_3.

Each of these techniques yield different information about the discs structure and using combinations of these observing techniques, a detailed picture of protoplanetary discs can be obtatined. The following sections describe the key properties of accretion discs that are used in subsequent Chapters.

1.2.1 Disc Mass

One of the earliest estimates for protoplanetary disc masses, along with the distribution of this mass, comes from our own solar system. Through observations, the masses, orbital radii and chemical composition of the planets in our solar system

can be determined. Using these it is possible to place a lower bound on the amount of material that was present in the disc surrounding the young sun, as well as gain a crude estimate on the distribution of this material. Weidenschilling (1977) obtained estimates for this 'Minimum Mass Solar Nebula', or MMSN by first taking the inferred masses of the heavier elements in each planet, and augmenting its mass with gas until the planet reaches solar composition. By then spreading this mass around an annulus centred on the semi-major axis of the planet it is possible to obtain a characteristic surface density Σ for the disc at the location of each planet. This analysis finds that the surface density scales with disc radius as $\Sigma(r) \propto r^{-\frac{3}{2}}$.

A number of different normalisations for this surface density profile have been derived, but the most commonly used is that quoted by Hayashi (1981)

$$\Sigma_{gas}(r) = 1.7 \times 10^3 \left(\frac{r}{1\text{AU}}\right)^{-\frac{3}{2}} \text{ g cm}^{-2} \tag{1.2}$$

which gives $\sim 0.01 M_\odot$ of material enclosed within 30AU (the semi-major axis of Neptune). This is in the range of inferred masses of protoplanetary discs around other stars. Hayashi (1981) also estimates the surface density profile of dust in the disc,

$$\Sigma_{dust}(r) = \begin{cases} 7.1 \left(\frac{r}{1\text{AU}}\right)^{-\frac{3}{2}} \text{ g cm}^{-2} \text{ for } r < 2.7\text{AU}, \\ 30 \left(\frac{r}{1\text{AU}}\right)^{-\frac{3}{2}} \text{ g cm}^{-2} \text{ for } r > 2.7\text{AU}. \end{cases} \tag{1.3}$$

Note the discontinuity at 2.7AU, this is due to icy materials present in the outer regions that cannot survive inside this point, which is known as the snow line, causing the surface density of solids beyond this location to increase by a factor of ~ 4.

This minimum mass solar nebula is a useful lower limit on protoplanetary disc masses around stars at the end of the formation process (Class II sources). In reality the disc undergoes substantial evolution over time, and it is likely that the initial mass of the disc was several times larger the the MMSN, especially during the early collapse phase (Class 0/I sources)

Beyond our own solar system, disc masses are determined from observations as previously described. Disc masses are usually determined by observations in the mm/sub-mm part of the spectrum. These observations allow us to estimate the total mass of dust within a disc. By adopting a gas to dust mass ratio for the disc (typically taken to be 100:1), we can obtain an estimate for the total mass of the disc. Around typical Class II sources with solar mass stars, discs are estimated to range from $\sim 10^{-4} - 10^{-1} M_{\odot}$. Across this range, most discs have masses ranging from $0.005 M_{\odot}$ to $0.01 M_{\odot}$, with higher mass discs occurring only rarely around class II sources (Andrews et al., 2010). This is in good agreement with the MMSN estimate.

At these mass ranges, the dynamics of the disc are likely to be Keplerian, dominated by the stellar gravity, with the self-gravity of the disc being negligible (typically gravitational instabilities set in when the mass of the disc is greater then $\sim 0.1 M_{*}$). In the earlier collapse phase, when the star is less massive, and the disc is more massive, this ratio will be much higher, with disc-to-star mass ratios reaching unity for very young (Class 0) objects.

Finally, it should be noted, that disc mass measurements at mm wavelengths are still subject to fairly large uncertainties. These uncertainties arise from multiple areas, however the major sources or error are as follows;

- In the inner regions of the disc, column densities of dust are high, therefore the disc becomes optically thick, reducing the emission from the inner regions of the disc, resulting in the disc mass being underestimated.
- The gas-to-dust mass ratio, canonically taken to be 100:1, can vary depending on the environment the disc was born from.
- The presence of large dust grains ($\geq$ 1cm) can cause the opacity of the disc to decrease, these large dust grains radiate at longer wavelengths, and due to their large mass-to surface area ratio, tend to conceal mass from observations.

Consequently, mm and sub-mm observations tend to underestimate physical disc masses (Andrews & Williams, 2005; Hartmann et al., 2006; Andrews & Williams,

2007). Therefore even in many standard T Tauri discs gravitational instabilities might still play an important role in angular momentum transport.

As outlined in the overview of the Minimum Mass Solar Nebula model, typically the distribution of material within discs is described through the use of a power-law, $\Sigma(r) \propto r^{-n}$. In the MMSN, $n = 1.5$, however observations of protoplanetary discs around T-Tauri stars suggest that many discs may follow a shallower surface density profile, with typically falling between 0.5 and 1. More recently, it has been suggested that discs are truncated at large radii, following a profile as (Hughes et al., 2008; Andrews et al., 2010),

$$\Sigma(r) \propto r^{-n} \exp\left[-\left(\frac{r}{r_c} \right)^{2-n} \right] \tag{1.4}$$

here r_c is known as the truncation radius, and defines the discs outer radius. Applying this formalism to previously observed discs yields values of n from $0.1 - 0.9$ (Andrews et al., 2010).

1.2.2 Disc Size

Estimates of the physical size of circumstellar discs are obtained via observations of both cold gas ($T \sim 10$K) in the millimetre and sub-millimetre wavelength, and continuum emission from dust particles. Generally the gaseous component of the disc extends out much further than the solid, dust based component (Isella et al., 2007; Hughes et al., 2008).

As outlined in the previous Section, the gas surface density profile follows a power-law throughout most of the disc, but decays approximately exponentially near the outer boundary (Hughes et al., 2008). This outer boundary slowly moves further outwards because of the discs viscous evolution, see Lynden-Bell & Pringle (1974); Hartmann et al. (1998); Armitage (2010) and Chapter 2 below. Equation 1.4 shows the most important quantity in determining the physical size of the disc is the discs truncation radius r_c. Observations of discs around T-Taurii stars indicate that $30\text{AU} < r_c < 230\text{AU}$ for the majority of YSO's (Hughes et al., 2008; Andrews et al., 2009; Isella et al., 2009; Andrews et al., 2010), with older discs

having larger radii due to the viscous spreading previously mentioned, covered in greater detail in the following section, while younger discs, including the youngest ones around Class I objects, tend to have smaller radii, typically $r_c \sim 70$AU, as they have not yet undergone substantial slow viscous evolution.

1.3 Disc Dynamics

The dynamical evolution of discs proceeds primarily through the redistribution of angular momentum within the disc. The redistribution of angular momentum is key in the accretion of material from the disc onto the central star. By transporting angular momentum from the inner regions of the disc to the outer regions, material can fall inward, ultimately being accreted onto the central object. How angular momentum is transported within accretion discs is an active area of research, within several mechanisms for transport proposed. In reality, all probably play a part in angular momentum transfer at some point in the evolution of the disc, however the exact role each mechanism plays is not yet fully understood. The currently favoured mechanisms for angular momentum transport are outlined below in this section.

The angular momentum transport within accretion discs is characterised by a turbulent (rather than molecular) viscosity, the concept of which was introduced to accretion disc theory by Shakura & Sunyaev (1973). To demonstrate the role viscosity plays in the redistribution of angular momentum, consider the case of a simple razor-thin (2D) disc, rotating around a central body of mass M_*. Here, the equilibrium structure of a gaseous disc is determined by solving the hydrodynamical equations in conjunction with the Poisson equation for the gravitational potential of the system and finding a steady state solution. For low mass disks, where $M_{disc} \ll M_*$ we can ignore the gravity of the disc, and need only consider the gravitational potential of the star. In order to formally define this limit below which self gravity is negligible we must consider the aspect ratio of the disc, h/r, where h is the vertical disc scale-height, and is defined as,

$$h \equiv \frac{c_s}{\Omega}. \tag{1.5}$$

Here c_s is the sound speed and Ω is the Keplerian angular velocity,

$$\Omega = \sqrt{\frac{GM_*}{r^3}}. \tag{1.6}$$

When the aspect ratio of the disc satisfies $h/r \ll 1$ it is referred to a thin disc. By applying Gauss' theorem it can be shown that the self gravity of the disc is negligible provided,

$$\frac{M_{disc}}{M_*} < \left(\frac{h}{r}\right). \tag{1.7}$$

Assuming the self gravity of our disc is negligible, we can begin to describe how a simple 2D disc will evolve due to purely viscous effects. By visualising the disc as a series of annuli (Figure 1.2) we can derive the equation describing the evolution of the surface density of the disc. First consider an annulus between r and $r+\Delta r$ with a mass ΔM,

$$\Delta M = 2\pi r \Delta r \Sigma, \tag{1.8}$$

and angular momentum ΔL,

$$\Delta L = 2\pi r \Delta r \Sigma r^2 \Omega. \tag{1.9}$$

Mass conservation within the annulus gives

$$\frac{\partial}{\partial t}(2\pi r \Delta r \Sigma) = 2\pi r \Sigma(r) v_r(r) - 2\pi(r+\Delta r)\Sigma(r+\Delta r)v_r(r+\Delta r) \tag{1.10}$$

Expanding $\Sigma(r+\Delta r) = \Sigma(r) + \dfrac{\partial \Sigma}{\partial r}\Delta r$, etc and taking the limit $\Delta r \to 0$, we obtain the continuity equation for our annulus,

$$\frac{\partial \Sigma}{\partial t} + \frac{1}{r}\frac{\partial}{\partial r}(r\Sigma v_r) = 0. \tag{1.11}$$

Following the same procedure, conservation of angular momentum results in,

$$\frac{\partial}{\partial t}(\Sigma r^2 \Omega) + \frac{1}{r}\frac{\partial}{\partial r}(r\Sigma v_r r^2 \Omega) = \frac{1}{2\pi r}\frac{\partial G}{\partial r}. \tag{1.12}$$

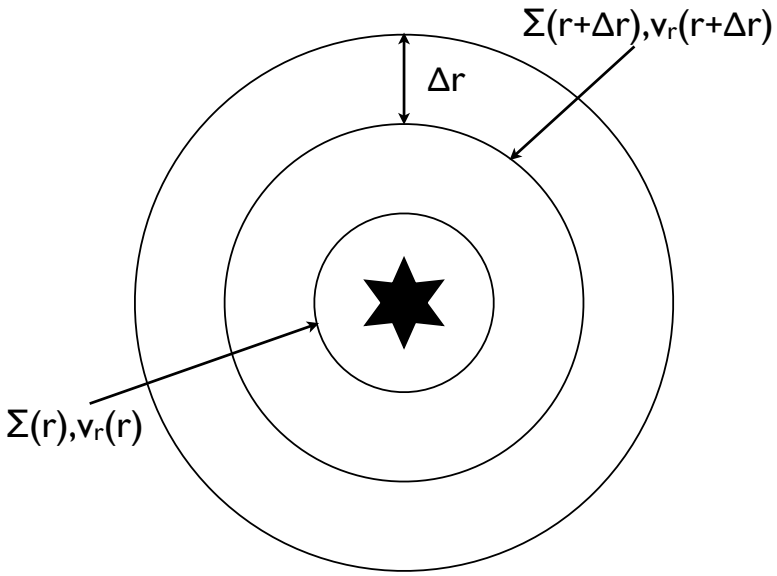

Figure 1.2 *Representation of an accretion disc around central object divided into a series of anulli.*

where G is the torque exerted on an annulus by its neighbours,

$$G = 2\pi r \cdot \nu \Sigma r \frac{\mathrm{d}\Omega}{\mathrm{d}r} \cdot r, \tag{1.13}$$

for a viscous fluid of kinematic viscosity ν.

Combining equations 1.12 and 1.13 to eliminate v_r give the evolution equation for the surface density of a thin disc under angular momentum transport,

$$\frac{\partial \Sigma}{\partial t} = \frac{3}{r}\frac{\partial}{\partial r}\left[r^{\frac{1}{2}} \frac{\partial}{\partial r}(\nu \Sigma r^{\frac{1}{2}}) \right]. \tag{1.14}$$

The evolution equation is a diffusive equation for the surface density of the disc, Σ, where the diffusion constant $D \sim \nu/r$. The corresponding timescale for material to cross a radial distance Δr via diffusion is then simply,

$$\tau_\nu = \frac{(\Delta r)^2}{\nu} \tag{1.15}$$

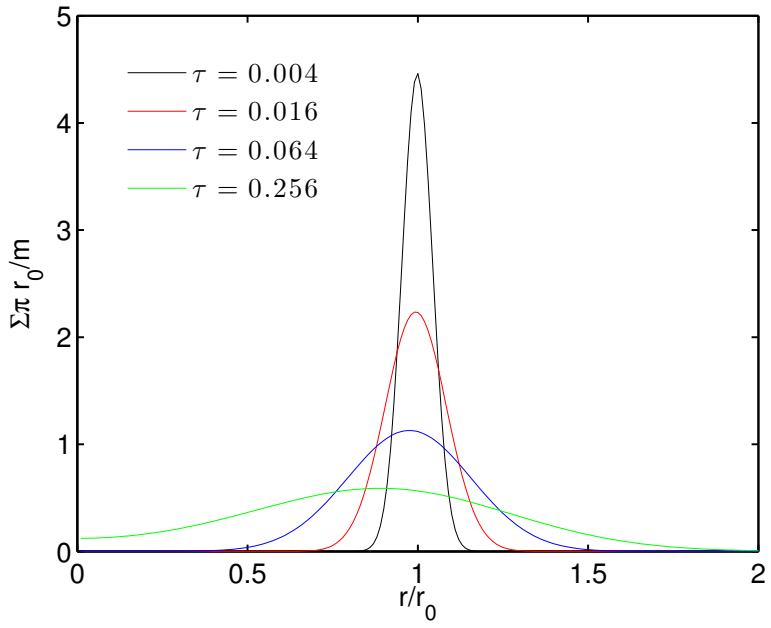

Figure 1.3 *Evolution of the surface density of an initially thin ring of material initially located at a radius r_0 spreading under the action of a constant viscosity, ν. Each curve shows the surface density profile of the ring as the non-dimensional time parameter $\tau = 12\nu r_o^{-2} t$ increases. Figure adapted from Armitage (2010)*

To visualise the way a disc will evolve under viscous effects, let us return to the case presented in Figure 1.2 and consider a thin ring of material of mass m located at an orbital radius r_0. If we assume the viscosity ν is constant, the ring of gas evolves under viscous diffusion as shown in Figure 1.3.

Figure 1.3 shows that over time, the material contained in the inner regions of the ring tends to lose angular momentum, resulting in the material moving inwards, eventually being accreted onto the central star. Conversely, material in the outer regions of the disc receives angular momentum from the inner region of the disc, resulting in the material moving to larger radii. Eventually almost all the material is accreted onto the central star, with a negligibly small amount of material carrying the angular momentum out to infinitely large radii.

From this we see that viscosity plays an important role in the evolution of accretion discs, being the dominant mechanism for the redistribution of angular

momentum within the disc. However, the physical origin of the viscosity is not well understood, with several possible mechanisms currently proposed. The first candidate that was considered, and subsequently ruled out, was viscosity arising from molecular collisions. This arises due to the finite mean free path, λ, in the gas. This molecular viscosity is simply described by the product of the mean free path and the velocity of the molecules, which is of order the sound speed of the gas,

$$\nu_m = \lambda c_s. \tag{1.16}$$

The mean free path of the gas is,

$$\lambda = \frac{1}{n\sigma_{mol}}, \tag{1.17}$$

where n is the number density of the gas, and σ_{mol} is the collisional cross-section of the molecules, which is approximately equal to the physical size of the molecules. In a typical proto-planetary disc, with a number density $n \sim 10^{13}\text{cm}^{-3}$ and $\sigma_{mol} \sim 10^{-15}\text{cm}^2$, the mean free path is 10^2cm. Taking the sound speed in the disc to be 500ms^{-1} at 10AU, we find $\nu_m = 5\times10^6\text{cm}^2\text{s}^{-1}$, which gives the timescale for molecular viscosity,

$$t_\nu \sim \frac{r^2}{\nu_m} \sim 10^{13}\text{yr}. \tag{1.18}$$

As stated previously, the observed lifetime for proto-planetary discs is typically no more than 10^7yrs, approximately a million times shorter than the timescale for disc evolution due to molecular viscosity. Molecular viscosity can not therefore be the dominant mechanism for angular momentum transport in accretion discs, there must be other mechanisms capable of creating viscosity many orders of magnitude larger that will be consistent with observed disc lifetimes.

One consequence of such a small molecular viscosity however is a large Reynolds number, Re,

$$\text{Re} \equiv \frac{RU}{\nu_m}, \tag{1.19}$$

where R and U are characteristic length and velocity scales for the system. By adopting $R = h$ and $U = c_s$ and assuming a typical disc with $h = 0.05r$, we find $\text{Re} \sim 10^{10}$ at an orbital radius of 10AU. Such a large Reynolds number results in a highly turbulent disc, resulting in the dissipation of fluid motions

occurring on scales comparable to the disc scale height. Assuming the disc is turbulent, the turbulent fluid motions result in the mixing of fluid elements at neighbouring radii. This can act as an effective viscosity, often referred to as a turbulent viscosity. Since turbulence is generally a highly complex phenomena, we cannot determine the characteristic length-scales and velocities associated with the turbulent fluid without a good understanding of the physical process causing the turbulence to develop. Despite this, we can use physical arguments to constrain these quantities. If the turbulence is isotropic, the turbulent flow cannot be larger than the smallest scale in the disc, the scale height h. The velocity of the turbulent flow can also be limited to be no larger than the sound speed c_s, as the development of supersonic motion would result in shocks and the rapid dissipation of turbulent motion. Based on these two arguments, Shakura & Sunyaev (1973) parametrized turbulent viscosity as,

$$\nu_t = \alpha c_s h, \tag{1.20}$$

where α is a dimensionless parameter, referred to as the Shakura-Sunyaev α parameter, which measures how efficient angular momentum transport due to turbulence is.

Through this parametrization of the turbulent viscosity, we effectively replace one unknown parameter ν_t, with another, α. which is measured in terms of the local pressure within the disc. If α exceeds unity, the turbulence must be non-local. One of the biggest advantages of the α parameter is that it can be observationally measured, allowing for any model of turbulent viscosity to be tested against real data. Observations of circumstellar discs indicate that $\alpha \sim 0.01$ (Hartmann et al., 2006; Andrews et al., 2010), which predicts disc lifetimes of $\sim$ 10Myr, a value which is also consistent with observations.

It is crucial to have a proper understanding of disc turbulence and its origin, as apart from driving the accretion process, it can also have a significant effect on other processes occurring in discs. This, in turn, allows us to determine α in different parts of the disc and make comparisons with observations. Recently, much progress has been made in identifying possible mechanisms which can induce turbulence in accretion discs. As accretion discs possess a Keplerian

rotation profile (unless they are strongly self-gravitating), much of this research has been focussed on investigating the stability of this profile, what can cause it to become turbulent, and the properties of this turbulent state.

Mechanisms which can cause angular momentum transport in discs, can generally be placed in one of two categories; magneto-hydrodynamic (MHD) mechanisms primarily give rise to magneto-rotational instability (MRI). Alternatively non-magnetic mechanisms, such as a purely hydrodynamical turbulence, spiral density waves that can arise in due to self gravity in massive discs, as well as coherent vortices can all result in angular momentum transport.

In the following sections, we outline these mechanisms individually, concentrating primarily on the mechanisms that are relevant to the later sections of the thesis.

1.3.1 Gravitational Instability

Gravitational instability arises in very massive discs, where the disc mass is comparable to the mass of the central star. Its influence results in the formation of density perturbations within the disc, usually in the form of spiral density waves (Figure 1.4). These density waves exert torques on the disc, resulting in the transfer of angular momentum outwards and mass flow inward. However these spiral density waves are often large scale structures, potentially spanning the radius of the disc. In this case the α prescription previously employed may not necessarily be valid, as it is a local description. Under certain conditions, the self-gravity of the disc can also cause the disc to break up, or fragment, potentially playing an important role in the planet formation process (Figure 1.5). As the disc must be massive, the role of self-gravity is thought to dominate angular momentum transfer in the early phase of the discs lifetime, during the Class I phase, whilst playing a diminishing role in the later phases of the disc lifetime, giving way to other transport mechanisms, such as MRI.

The fundamental physics responsible for gravitational instability in discs is essentially the same as the Jeans instability in a homogeneous fluid. Any over-density in the disc will tend to be enhanced by the gravitational collapse of surrounding material. This process is opposed by pressure forces within the over-

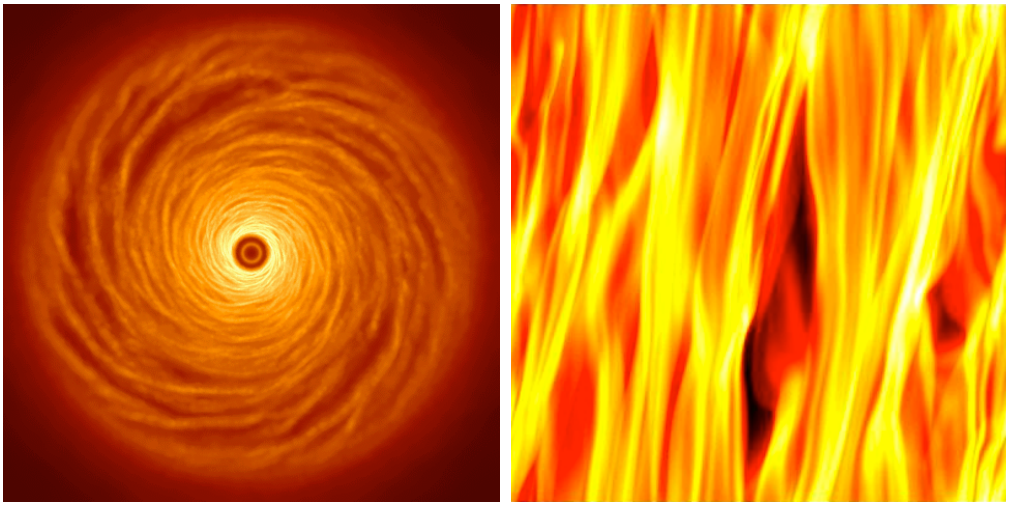

Figure 1.4 *Surface density structure of a self-gravitating disc in both global (left) and local (right) simulations. In both images we see strong density wave structure present as a result of self-gravity.*

Figure 1.5 *Potential outcomes of a disc unstable to self-gravity. the left hand image shows a disc which has undergone fragmentation, the right hand image has settled into a quasi-steady state, developing spiral density waves.*

density. In this scenario, there are two possible outcomes. If the initial mass of the over-dense region is greater than some characteristic value, known as the Jeans mass, then the pressure forces are insufficient to oppose the gravitational forces and gravitational collapse ensues. If however the mass of the region is less than the Jeans mass, the pressure forces are sufficient to balance the gravitational forces, preventing collapse.

In an accretion disc this scenario is modified slightly by the differential rotation and geometry of the disc. By making two simplifying assumptions, namely that the perturbations have radial wavelengths much smaller than the disc radius and the perturbations are axisymmetric (Safronov, 1960), the dispersion relation for density waves for a two dimensional disc is,

$$\omega^2 = c_s^2 k^2 - 2\pi G\Sigma k + \Omega^2. \tag{1.21}$$

Here ω and k are the frequency and (radial) wavenumber of the density wave, c_s and Σ are the sound speed and surface density within the disc, Ω is the angular frequency of the disc and G is the gravitational constant. When $\omega^2 < 0$, instabilities develop and grow at an exponential rate. By noting that equation 1.21 is quadratic in k, it becomes clear that a range of wavenumbers exist for which $\omega^2 < 0$ provided,

$$Q \equiv \frac{c_s \Omega}{\pi G \Sigma} < 1. \tag{1.22}$$

This parameter, often known as the Toomre Q parameter Toomre (1964), provides a measure of the strength of self-gravity in a thin disc and is therefore a key component in the study of gravitational instabilities in discs. The Q parameter fundamentally tells us that at a given radius within the disc, the disc will develop gravitational instabilities if it is either massive (large Σ), or cool (small c_s). In the slightly more general case of non-axisymmetric perturbations, such as spiral density waves, the disc becomes less stable against gravitational perturbations. In this case, the disc tends to develop gravitational instabilities at values of $Q \sim 1.5-2$. Goldreich & Tremaine (1978) proposed that Q tends to self-regulate, where a massive disc starts to collapse under its own self-gravity, causing the disc to heat up, and raising the sound speed within the disc. This tends to raise the local value of Q until it is above the critical value required for gravitational instability,

and self-gravity switches off until the disc has sufficiently cooled, lowering the sound speed, and causing self-gravity to return. Through this cycle, Q tends to oscillate around the critical value required for gravitational instability. The stability criteria is often recast in a slightly more intuitive form by recalling the disc scale height $h = c_s/\Omega$. For a disc with a surface density profile $\Sigma(r)$, the total mass of the disc is,

$$M_{disc} = \int_{r=0}^{r=r_{out}} 2\pi r \cdot \Sigma(r) \mathrm{d}r. \tag{1.23}$$

For a power law surface density profile,

$$\Sigma(r) = \Sigma_0 \left(\frac{r}{r_0} \right)^{-q}, \tag{1.24}$$

the disc mass contained within a radius r_{out} is,

$$M_{disc} = \frac{2\pi\Sigma_0}{(2-q)r_0^{-q}} \, r_{out}^{(2-q)}. \tag{1.25}$$

By using this expression for the disc mass, the criteria for disc instability becomes,

$$\frac{M_{disc}}{M_*} > \frac{2}{(2-q)r_0^{-q}} \frac{h}{r_{out}^{(q+1)}}. \tag{1.26}$$

This is often reduced to the simple $q = 0$ case corresponding to a flat surface density profile.

$$\frac{M_{disc}}{M_*} > \frac{h}{r_{out}}. \tag{1.27}$$

As observations indicate h/r_{out} is typically in the range $0.05-0.1$ for circumstellar discs, it now becomes readily apparent that we require massive discs for gravitational instabilities to set in.

If self-gravity sets in within the disc, there are two possible outcomes, analogous to the case previously described for a homogenous fluid. If the perturbations are large enough the resulting gravitational collapse will continue, with the pressure forces within the disc insufficient to balance the gravitational forces. This will cause the disc to break apart, or fragment, forming bound clumps of material, potentially forming gas giant planets. Alternatively if the collapse is

relatively slow, heating within the material as it contracts may yield pressures high enough to prevent total collapse, leaving the disc in a quasi steady state, where gravitational collapse is balanced by pressure due to the heating. The resulting instabilities tend to result in a number of spiral density waves developing within the disc, which transport angular momentum outwards. The boundary that separates these two outcomes is defined by the thermal properties of the disc. If the disc can rapidly radiate away its thermal energy, pressure cannot build up within contracting clumps, allowing the disc to collapse and fragment. Slow cooling results in a quasi stable disc.

The study of this process has been an active area of research in recent years. Boss (1998) confirmed using numerical simulations of global discs that discs can indeed fragment as a result of self-gravity, and that the resulting fragments are sufficiently massive to be considered giant planets, or potentially even brown dwarves. Using local, shearing sheet (see Chapter 3), simulations, Gammie (2001) investigated the conditions required for fragmentation to occur, and investigated the rate at which gravitational instabilities can transport angular momentum in this local approximation if the disc does not fragment. By defining a simple timescale upon which the disc cools,

$$t_c = \frac{U}{\dot{U}}, \tag{1.28}$$

where U and $\dot{U}$ represent the internal energy of the gas and its time derivative, Gammie (2001) showed that the disc will fragment if the cooling timescale is of order the dynamical timescale of the disc,

$$\Omega t_c < \beta \tag{1.29}$$

where β is a constant, initially found by Gammie (2001) to be ~ 3, though the exact value of this figure is an active area of research.

Gammie (2001) also showed that the angular momentum transfer within the disc can be determined by considering the cooling time of the disc, locally, the disc will be heated at a rate,

$$Q_+ = \frac{9}{4}\nu\Sigma\Omega^2, \tag{1.30}$$

and cool at a rate,

$$Q_{-} = 2\sigma T_{disc}^4. \tag{1.31}$$

If the disc does not fragment, these two terms balance and we obtain an expression for the gravitational viscosity,

$$\nu = \frac{8\sigma T_{disc}^4}{9\Sigma\Omega^2}. \tag{1.32}$$

By relating this to the Shakura-Sunyaev expression,

$$\nu = \alpha c_s h, \tag{1.33}$$

Gammie (2001) showed that α can be expressed purely in terms of the cooling time of the disc,

$$\alpha = \frac{4}{9\gamma(\gamma-1)\Omega t_c}, \tag{1.34}$$

where γ is the two dimensional adiabatic index relating the pressure and internal energy as $P = (\gamma - 1)U$. This relationship was tested by both Gammie (2001) and Rice et al. (2003) in both local and global simulations, both cases found the relationship to hold for discs in a quasi steady state, within numerical errors. From this relation, we see that the viability of gravitational instability as a mechanism for angular momentum transport is also dependent on the cooling time of the disc. For relatively short cooling times, $\beta < 100$, the rate of angular momentum transfer is consistent with observations, and gravitational instability is likely to be the dominant mechanism for angular momentum transfer. Studies indicate that such cooling times are typically confined to the outer regions of the disc ($r \gtrsim 10 - 20$AU) (Clarke, 2009). For longer cooling times, the transport rate starts to rapidly drop off, and another mechanism is required to sustain observations.

1.3.2 Vortices

Vortices in protoplanetary discs have also been studied recently, as they provide a potential mechanism for the transport of angular momentum, as well as being a potential site for the formation of planets within the disc. The formation and

evolution of vortices in a disc has been studied through numerical simulations in both a global and local setting. In these studies, vortices are often characterised by the z-component of their Potential Vorticity (PV), I_z,

$$I_z \equiv \frac{1}{\Sigma}\big(\nabla \times \mathbf{u} + (2-q)\Omega\big). \tag{1.35}$$

It has been shown in simulations of both self-gravitating and non self-gravitating discs that only anticyclonic vortices can survive for prolonged periods of time (Johnson & Gammie, 2003; Mamatsashvili & Rice, 2009). Anti cyclonic vortices are those which rotate in the same orientation as the background shear. In non self-gravitating discs, these structures can survive for several hundred orbital periods, and can be considered stable structures over short time scales. The alternative case of cyclonic vortices, which rotate against the shear, are quickly destroyed by the differential rotation of the disc. In simulations, the PV field is initially seeded either with random perturbations continuing small positive and negative fluctuations such as those performed in Johnson & Gammie (2003), or a single, well defined vortex e.g. Johansen et al. (2004). Simulations show that initial random fluctuations are initially sheared out, which then curl up into vortices. These vortices can grow via mergers with other vortices until they are approximately the size of the scale height of the disc.

Anticyclonic vortices radiate energy in the form of density waves, triggering shocks in the disc, and it is through these shocks that vortices can greatly enhance the rate of angular momentum transport through the disc. Li et al. (2001) showed that shocks generated by the emission of density waves by vortices can result in $\alpha \sim 10^{-3} - 10^{-2}$, resulting in vortices also being a viable candidate for the observed transport rate in discs. Anticyclonic vortices have also been shown to be effective at trapping dust particles present in the disc (Johansen et al., 2004; Klahr & Bodenheimer, 2006; Lyra et al., 2009). As a result of this, vortex structure has been proposed as a preferred site for planetesimal formation in protoplanetary discs, though the particle trapping properties of vortices in self-gravitating discs are not yet understood.

1.3.3 Magneto-rotational Instability

Magneto-rotational Instability (MRI) is an instability that occurs in ionised gaseous discs that have a magnetic field present. Although the main body of this thesis does not study the effects of MRI, MRI is generally accepted to be the dominant cause of turbulence in most accretion discs, especially in the later stages of their evolution, when discs are unlikely to be massive enough for gravitational instabilities to set in, and is discussed here for completeness.

In order for MRI to set in, the disc is required to have regions where the gas is sufficiently ionized to couple effectively with magnetic field, so that the field can affect the gas dynamics.

The condition for a weakly magnetised disc flow to be linearly unstable is that the angular velocity decrease with radius,

$$\frac{\mathrm{d}}{\mathrm{dr}}(\Omega^2) < 0, \tag{1.36}$$

which is satisfied by Keplerian discs. Let us now consider an axisymmetric, incompressible disc threaded by a vertical magnetic field. The equations of motion of a parcel of gas (in cylindrical polar coordinates) are then,

$$\ddot{r} - r\dot{\phi}^2 = -\frac{\mathrm{d}\Phi}{\mathrm{dr}} + f_r, \tag{1.37}$$

$$r\ddot{\phi} + 2\dot{r}\dot{\phi} = f_\phi, \tag{1.38}$$

where f_r and f_ϕ are forces describing the coupling of the gas to the magnetic field. In order to make these equations clearer, we define a local Cartesian coordinate system in a small parch of the disc at a radius r_0, co-rotating with the disc with angular velocity Ω,

$$r = r_0 + x, \tag{1.39}$$

$$\phi = \Omega t + \frac{y}{r_0}, \tag{1.40}$$

we obtain,

$$\ddot{x} - 2\Omega y = -x\frac{\mathrm{d}\Omega^2}{\mathrm{d}\ln r} + f_x, \tag{1.41}$$

$$\ddot{y} + 2\Omega\dot{x} = f_y, \tag{1.42}$$

after discarding quadratic terms. Here we clearly see the second term on the left-hand side of these equations represents the Coriolis force, in order to understand the effects of MRI, we must define the magnetic force (f_x, f_y). By modelling perturbations as plane waves varying with height, z, and time, t as,

$$\mathbf{s} \propto e^{-i(kz-\omega t)}, \tag{1.43}$$

the magnetic force is,

$$\mathbf{f} = -(kv_A)^2\mathbf{s} \tag{1.44}$$

where v_A is the Alfvén speed,

$$v_A = \sqrt{\frac{B_z^2}{4\pi\rho}}, \tag{1.45}$$

for a magnetic field $\mathbf{B}$ and gas density ρ. By using this expression for $\mathbf{f}$, and combining equations 1.41 and 1.42, we can obtain a dispersion relation which is quadratic in ω^2,

$$\omega^4 - \omega^2\left[\frac{\mathrm{d}\Omega^2}{\mathrm{d}\ln r} + 4\Omega^2 + 2(kv_A)^2\right] + (kv_A)^2\left[(kv_A)^2 + \frac{\mathrm{d}\Omega^2}{\mathrm{d}\ln r}\right] = 0. \tag{1.46}$$

Here we see that the instability criterion is,

$$(kv_A)^2 + \frac{\mathrm{d}\Omega^2}{\mathrm{d}\ln r} < 0. \tag{1.47}$$

The maximum growth rate of these instabilities in a Keplerian disc can then be shown to be,

$$|\omega_{max}| = \frac{3}{4}\Omega. \tag{1.48}$$

This growth rate is extremely rapid, any instability that develops grows exponentially, with a time scale less than an orbital period. As a result, it is

likely that the evolution of any disc where MRI sets in is likely to be dominated by the resulting turbulence.

The existence of MRI turbulence was first realised by Velikhov (1959), and further studied by Chandrasekhar (1960), however it was not until Balbus & Hawley (1991) demonstrated that MRI can operate in discs threaded by a stellar magnetic field that its significance was recognised. Since then, the non-linear effects of MRI have been investigated using numerical simulations. Brandenburg et al. (1995); Hawley et al. (1995) investigated the effects of MRI using local simulations, studying the effects of MRI on the evolution of α, similarly Armitage (1998); Hawley (2001) have investigated MRI turbulence using global simulations. In all these studies, the MRI results in the breakdown on the Keplarian flow into MHD turbulence, causing angular momentum to be transferred from the inner regions of the disc to the outer regions via Maxwell stresses. The values of α measured in these studies are also within the required range for agreements with observations, with α typically lying in the range $10^{-3} < \alpha < 10^{-1}$. For these reasons, MRI is the currently favoured mechanism for the origin of turbulent viscosity and transport of angular momentum through the disc.

1.4 Planet Formation in Discs

The main aim of this thesis is to show how instabilities that arise in self-gravitating discs can aid the planet formation process. Here we outline the two proposed models of planet formation, and discuss how the work presented in this thesis fits into the models. These two models are usually referred to as the core accretion and disc fragmentation models. In the core accretion model, initially small dust grains grow via collisional growth until they reach asteroid (m-km) sizes. Such bodies are often referred to as planetesimals. These objects continue to grow until they reach terrestrial planet sizes. If they reach a critical mass (usually around 10 Earth masses), these planets will start to rapidly accrete gas from the disc onto their surfaces, and form gas giants. The alternative disc fragmentation model suggests that gas giants may be able to form directly in massive discs where gravitational instabilities are present. The following sections

discuss these models in more detail, separating the evolution of bodies within the disc into three separate stages, depending on the physical size of the object, and the processes dominant in its evolution.

1.4.1 Dust Grain Evolution

Proto-planetary discs are initially constructed from gas and micron sized dust particles. In order to construct terrestrial planets or the cores of giant planets, typically 1000's of kilometers in size, these dust particles must grow by many orders of magnitude. The first stage of growth is the growth of objects from small dust grains into planetesimals. Planetesimals are loosely defined as objects with radii between 1-100 kilometers. Such objects are large enough that their orbital evolution is governed by gravitational interactions with each other rather than aerodynamic coupling to the disc. The formation of planetesimals is one of the most poorly understood parts of the core accretion process, as although the forces acting on individual particles are thought to be reasonably simple, there is no solid explanation as to how these particles grow to km size scales.

Here we describe the evolution of dust particles, and outline how planetesimals can grow from these small particles. By making the simplifying assumption of spherical dust particles the drag force that solid particles feel due to interactions with the disc is given by ,

$$\mathbf{F}_D = -\frac{1}{2} C_D \pi a^2 \rho u^2 \hat{\mathbf{u}}, \tag{1.49}$$

where $u = |\mathbf{u}|$, $\hat{\mathbf{u}} = \mathbf{u}/u$, a is the mean radius of planetesimals and C_D is the drag coefficient, describing how aerodynamic the particles are. The following piecewise expression for C_D is often used (Weidenschilling, 1977; Rice et al., 2003), although

it should be noted other prescriptions for modelling drag force exist.

$$C_D = \begin{cases} \frac{8}{3}\frac{c_s}{u} \text{ for } a < 9\lambda/4 \\ 24R_e^{-1} \text{ for } R_e < 1 \\ 24R_e^{-0.6} \text{ for } 1 < R_e < 800 \\ 0.44 \text{ for } R_e > 800 \end{cases} \tag{1.50}$$

The first case is known as Epstein regime, which applies to particles smaller than λ, the mean free path of the gas molecules within the disc.

$$\lambda = \frac{m_{H_2}}{\rho A} \tag{1.51}$$

where m_{H_2} and A are the mass of a hydrogen molecule and its cross sectional area respectively.

The remaining three cases define Stokes drag, which applies to larger particles, and solely depend on the Reynolds number R_e, given by

$$R_e = 4\left(\frac{a}{\lambda}\right)\left(\frac{u}{c_s}\right). \tag{1.52}$$

The aerodynamic drag force detailed above provides a reasonable description of the dynamical evolution of particles within a disc. However, in order to form large planetesimals, there must be a mechanism through which particles can grow to planetesimal sized scales. The simplest mechanism for particle growth is through a series of constructive collisions with other particles. Whether or not this is actually a feasible method for planetesimal formation depends on two factors, how often particles collide with one another, and are these collisions likely to result in growth? For particles of number density n, moving at relative velocities, Δv the collisional time scale is,

$$t_{collide} = \frac{1}{n\sigma\Delta v}, \tag{1.53}$$

where σ is the cross-section for collisions. Approximating the dust particles as spheres of radius a, with mass $m = (4/3)\pi a^3 \rho_d$, the cross section is simply,

$$\sigma = \pi(2a)^2. \tag{1.54}$$

The particle number density is

$$n = \frac{f\rho}{m}, \tag{1.55}$$

where ρ is the gas density and f is the density ratio of solids to gas. For smaller particles ($s \sim 1\mu$m) the velocity distribution is determined by brownian motion, equation 1.53 can be expressed as,

$$t_{collide} \simeq \frac{1}{4f}\left(\frac{a}{1\mu m}\right)^{\frac{5}{2}} \text{ yr.} \tag{1.56}$$

This time scale is very short, inevitably leading to many collisions between particles. If such collisions result in growth, planetesimal formation will be rapid under this regime. The likelihood of collisions resulting in growth is dependent on the properties of the dust particles. Small particles typically have low velocities ($\sim$ 1 cm/s) and the total energy of the collision is typically low, the outcome of the collision is determined by surface properties of the dust grains. As particles sizes and relative velocities increase, the likelihood of particles sticking together upon collision decreases.

One other important behaviour that dust particles embedded in a gaseous disc exhibit is inward radial drift. This behaviour arises due to velocity differences between the solid component of the disc and the gaseous component. Due to the radial pressure gradient present in the disc, the gas is partially pressure supported, with the radial component of the momentum equation becoming,

$$\frac{v_\phi^2}{r} = \frac{GM}{r^2} + \frac{1}{\rho}\frac{\mathrm{d}P}{\mathrm{d}r} \tag{1.57}$$

where P is the pressure in the disc. By taking a power law profile for P,

$$P = P_0\left(\frac{r}{r_0}\right)^{-n}, \tag{1.58}$$

where $P_0 = \rho_0 c_s^2$ is the pressure in the mid plane of the disc, we find,

$$v_\phi = v_{Kep}(1-\eta)^{1/2} \tag{1.59}$$

where v_{Kep} is the unperturbed Keplerian velocity and $\eta = n(c_s^2/v_{Kep}^2)$. For a typical disc, this results in a tiny ($< 1\%$) deviation from Keplerian velocities, which does not significantly alter the evolution of the gaseous component of the disc, however for dust particles that are aerodynamically coupled to the gas, this deviation can have a significant effect. These dust particles travel with Keplerian velocities as their motion is not directly affected by the pressure gradient in the disc, (i.e typically $v_\phi \neq v_{\phi,gas}$). As a result of the assorted mechanisms which can transport angular momentum outward discussed in Section 1.3, material falls inward, resulting in the gas having a radial component to it's velocity, $v_{r,gas}$. By taking the equations of motion for a dust particle in both the radial and azimuthal directions,

$$\frac{\mathrm{d}v_r}{\mathrm{d}t} = \frac{v_\phi^2}{r} - \Omega_K^2 r - \frac{1}{t_f}(v_r - v_{r,gas}), \tag{1.60}$$

$$\frac{\mathrm{d}(rv_\phi)}{\mathrm{d}t} = -\frac{r}{t_f}(v_\phi - v_{\phi,gas}), \tag{1.61}$$

where t_f is the friction time of the particle, $t_f = mv/|F_D|$, it can be shown that the radial velocity of the dust particle is given by,

$$v_r = \frac{\tau_f^{-1} v_{r,gas} - \eta v_K}{\tau_f + \tau_f^{-1}}. \tag{1.62}$$

Here we have recast the friction time in term of a dimensionless stopping time, $\tau_f = t_f \Omega$. In Figure 1.6 we plot this radial drift rate as function of stopping time for a typical protoplanetary disc. Small particles ($\tau_f \lesssim 10^{-2}$) drift in at a constant rate that is independent of stopping time, larger particles drift in at an increasingly rapid rate, with ($\tau_f \sim 1$) particles experiencing the fastest radial velocities. Beyond this value, the particles begin to decouple form the gas, and the effect of the drag force starts to rapidly drop. The τ_f particles usually correspond to $\sim$ 1m objects, though the exact physical size of these particles will depend on the disc parameters. In Figure 1.7 we plot the drift timescale for the $\tau_f = 1$ particles as a function of radius for a range of disc parameters. This

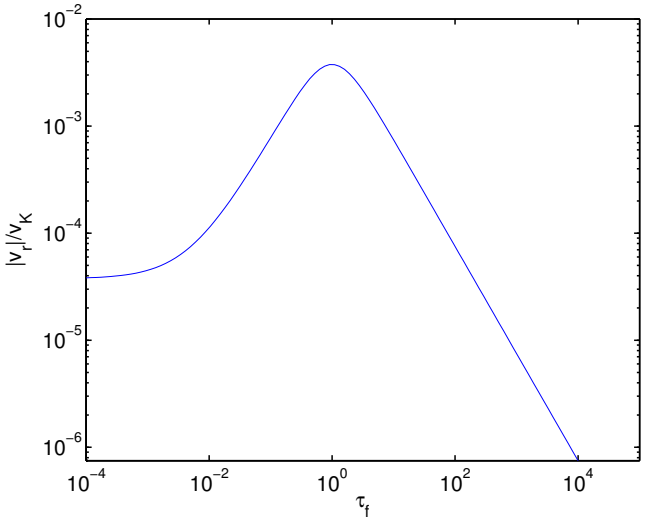

Figure 1.6 *The radial drift velocity of particles as a function of stopping time for a typical protoplanetary disc. Very small particles drift inwards at constant rate,which starts to increase for intermediate size objects, reaching a maximum at $\tau_f = 1$, larger particles decouple from the disc and the drift rate falls. Figure adapted from Armitage (2010)*

drift timescale is very short compared to disc lifetimes, typically no longer than $\sim$ 1000 years in the planet forming regions of the disc. From this we infer two key points,

- Growth from dust particles to km-scale planetesimals must be rapid, in order to avoid the destruction/accretion of solids.
- Solids will be redistributed throughout the disc due to aerodynamic drag forces.

From Figure 1.6 we can also infer the relative velocities, and subsequently the collisional timescale of larger dust particles, whose relative velocities are dominated by aerodynamic drag. By assuming that larger dust particles are close to the peak of the curve in Figure 1.6, we see that,

$$\Delta v \sim 10^{-3} v_K, \tag{1.63}$$

giving a collisional timescale of $\sim 10^3$ years for a dust to gas ratio of $f = 10^{-2}$.

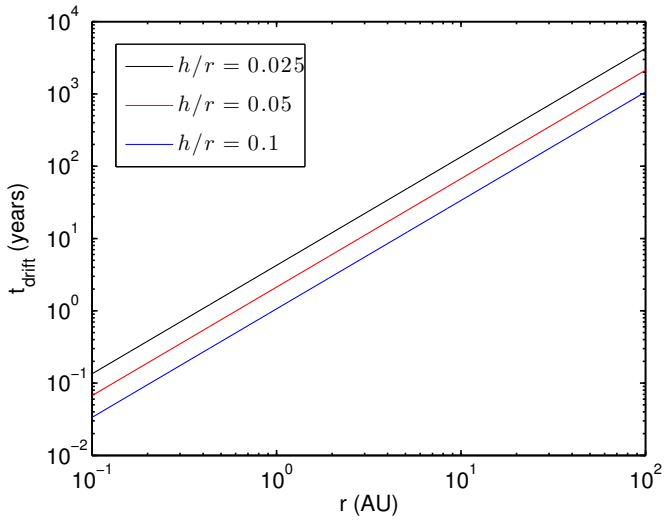

Figure 1.7 *Timescale for radial drift for meter-sized particles ($\tau_f \sim 1$) as a function of radius for a range of disc scale heights.*

At this point it is worthwhile to compare the growth rates of objects in the disc via collisions to the accretion of material as it passes through the disc. The accretion rate of a solid particle in a medium with sound speed c_s is (Bondi, 1952)

$$\dot{m} = \pi R^2 \rho_p c_s. \tag{1.64}$$

The capture radius R of the particle can be calculated from the expression for the escape velocity of the object,

$$R = \frac{2Gm}{c_s^2}, \tag{1.65}$$

The accretion rate is then,

$$\dot{m} = \frac{4\pi \rho_p G^2 m^2}{c_s^3}. \tag{1.66}$$

Figure 1.8 plots the different growth timescales due to collisions in a disc with varying dust to gas ratios, along with Bondi accretion. For smaller dust particles accretion is negligible, their growth is dominated by collisions with other particles. For larger planetesimal-sized objects, accretion starts to play a larger role, and is much more likely to be the dominant mechanism for the growth of larger planetesimals/terrestrial planets.

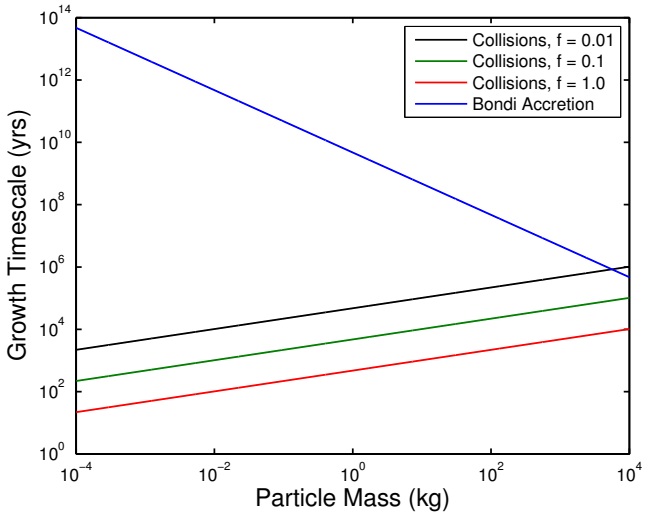

Figure 1.8 *Growth timescale as a function of object mass for collisional growth and Bondi accretion. Small dust grain's growth is dominated by collisions with other particles, however larger objects will tend to grow via accretion of material from the disc.*

How planetesimals can be formed quickly enough to avoid this rapid inward drift is a key problem in the theory of planet formation, and is one of the major issues the work contained in subsequent chapters attempts to resolve.

1.4.2 Planetesimal Evolution

Putting aside the above problems in growing to kilometre sizes, once a large population of planetesimals has formed inside the disc their evolution is dominated by gravity. This is probably one of the best understood areas of the core accretion process, as it is predominantly described by Newtonian gravity.

Terrestrial planets form from a series of collisions between these planetesimals. When two objects of this size collide, there are three possible outcomes (Figure 1.9) illustrates these three outcomes. If the relative velocities of two colliding objects of fixed masses are low, then the objects coalesce, although small fragments may be lost, the resulting body is larger than the impactors, and is still solid. For more energetic collisions, the impact shatters the initial bodies into

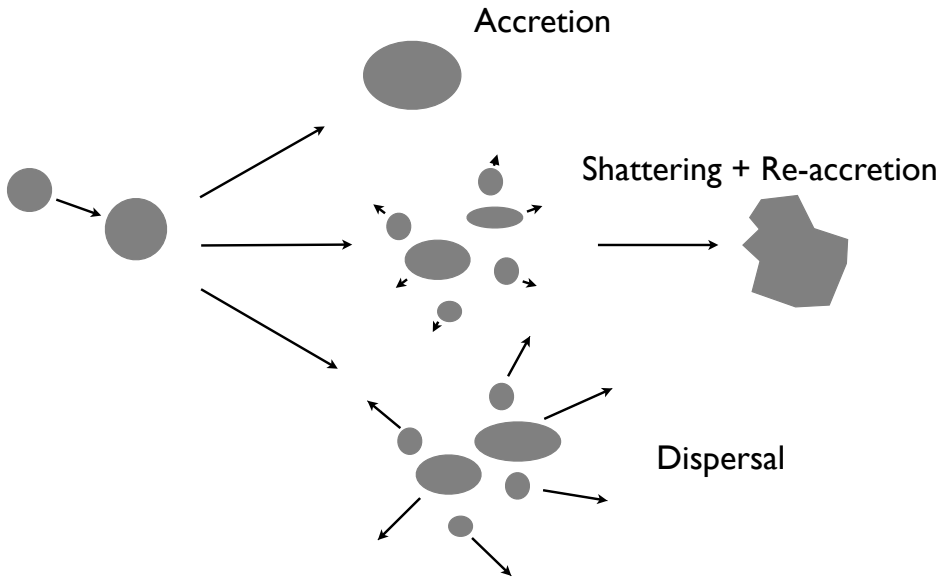

Figure 1.9 *Outcomes of a collision between two objects (Armitage, 2010).*

several pieces, however these pieces remain gravitationally bound to one another, and proceed to reassemble into a rubble pile. For very energetic collisions, the two objects are destroyed upon impact, with the resulting fragments dispersing, rather than remaining bound to one another. Defining the exact boundary between these three outcomes can be difficult, as it depends on a number of factors including the masses and velocities of the impactors, as well as their physical make up. Smaller bodies tend to be able to withstand impact better than larger ones due to the greater prevalence of structural defects in larger objects. Larger objects have greater gravitational potentials, allowing rubble piles to withstand dispersion for a wider range of impacts. For planetesimal sized objects the gravitational interaction between two colliding bodies is usually strong enough to ensure that most of the mass involved remains in a single object or rubble pile. This allows us to neglect the details of collisions and simply consider how often collisions occur, and how quickly objects grow as a result.

Due to their gravitational attraction, the collisional cross-section between two objects is increased through gravitational focusing, potentially increasing it far beyond the physical cross-section of the objects. The magnitude of this effect can

be estimated by considering the simple scenario illustrated in Figure 1.10.

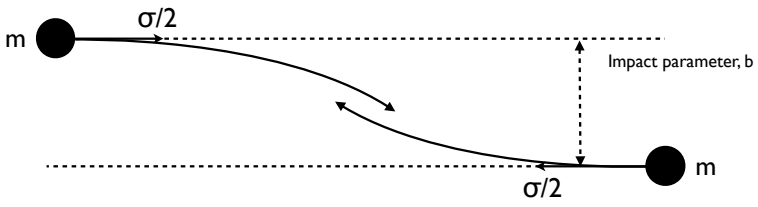

Figure 1.10 *Gravitational focusing*

By considering conservation of energy and angular momentum during the interaction, the gravitational cross-section, Γ, can be shown to be,

$$\Gamma = \pi R_s^2 \left(1 + \frac{v_{esc}^2}{\sigma^2}\right), \tag{1.67}$$

where R_s is the sum of the physical radii of the bodies and $vesc$ is the escape velocity from the point of collision. From this expression it is clear that in regions of the disc of planetesimals where $\sigma \ll v_{esc}$, gravitational focussing will dramatically increase the collisional cross-section.

Simulations of planet formation in discs cannot currently model each planetesimal individually. In order to model collisions in the disc, a statistical method is applied (Pollack et al., 1996) where the accretion rate of a growing protoplanet with mass M is assumed to be given by the rate at which planetesimals cross its orbit,

$$\frac{\mathrm{d}M}{\mathrm{d}t} = \pi R_c^2 \Sigma \Omega F_g. \tag{1.68}$$

Here R_c is the radius of the protoplanet, Ω is its orbital frequency and Σ is the average surface density of planetesimals within the area the protoplanet can accrete from, sometimes referred to as the feeding zone. F_g is the ratio of the gravitational cross section to the geometric cross-section (Pollack et al., 1996).

The limit on how large a protoplanet can grow is given by the properties of the planetesimals in the disc. When all the planetesimals within a planets feeding zone have been accreted, the body is said to have reached isolation mass. The

maximum extent of the feeding zone scales with the radius of the protoplanets Hill sphere, r_H as,

$$\Delta a_{max} = C r_H. \tag{1.69}$$

Simulations indicate $C = 2\sqrt{3}$. The mass of planetesimals within this feeding zone is (Lissauer, 1993; Kokubo & Ida, 2002),

$$M_{feed} = (4\pi \Sigma a \Delta a_{max})^3. \tag{1.70}$$

Combining equations 1.69 and 1.71 it can be shown that the isolation mass of a planet at a fixed radius a is (Ida & Lin, 2004),

$$M_{iso} = \frac{8}{\sqrt{3}} \pi^{\frac{3}{2}} C^{\frac{3}{2}} M_*^{-\frac{1}{2}} \Sigma^{\frac{3}{2}} a^3. \tag{1.71}$$

In reality a planets radius is not permanently fixed in the disc, as we detail in Section 1.5, therefore the isolation mass provides only a rough estimate of the potential size a protoplanet can grow to, but nonetheless is a useful lower bound of a planets potential mass.

1.4.3 Gas Giant Formation

As previously mentioned, there are two potential mechanisms through which gas giants can form. In the core accretion model once a protoplanet has reached terrestrial planet size (its mass is of order an Earth mass) it begins to interact gravitationally with the disc. For objects up to a certain value M_{crit} this results in eccentricity damping and the exchange of orbital angular momentum with the gas (See Section 1.5). Once an objects mass exceeds M_{crit} its gravitational pull becomes strong enough to accrete gas onto its surface from the proto-planetary disc. Based on numerical calculations, Ikoma et al. (2000) derived the following dependence for M_{crit},

$$M_{crit} \simeq 7 \left(\frac{\dot{M}}{10^{-7} M_\oplus \mathrm{year}^{-1}} \right)^{0.2-0.3} \left(\frac{\kappa}{1 \mathrm{cm}^2 \mathrm{g}^{-1}} \right)^{0.2-0.3} M_\oplus. \tag{1.72}$$

where κ is the opacity in the disc. For typical disc, this gives $M_{crit} \sim 10 M_{\oplus}$. Once this value has been reached, the planet will begin to accrete gas at a rate

$$\frac{\mathrm{d}M}{\mathrm{d}t} = \frac{M}{\tau_{grow}} \tag{1.73}$$

where the growth timescale is (Ikoma et al., 2000)

$$\tau_{grow} \sim 10^8 \left(\frac{M_{core}}{M_{\oplus}} \right)^{-2.5} \left(\frac{\kappa}{1 \mathrm{cm}^2 \mathrm{g}^{-1}} \right) \mathrm{yr} \tag{1.74}$$

Following this prescription for giant planet growth, Pollack et al. (1996) modelled the growth of a planet on a Jupiter-like orbit in a disc a few times as massive as the minimum mass solar nebula. They found that the growth of a giant planet's envelope follows two distinct phases. Whilst $M_{env} < M_{core}$, the overall accretion rate is low, leading to a slow increase in the planets mass and accretion zone. Pollack et al. (1996) found the length of this phase is dependent on either the gravitational contraction of the envelope or the time-scale for accretion of planetesimals. Both these processes liberate energy, which must be transported through the envelope via radiative diffusion Once $M_{env} > M_{core}$ the rate of accretion is no longer limited by the cooling properties of the envelope and is instead simply limited by the amount of material present in the planets feeding zone, leading to runaway growth of the envelope (Figure 1.11). This continues until the disc is depleted either locally, due to the planets accretion, or global disc dispersal sets in.

The alternative method that has been proposed has already been touched on in Section 1.3.1. In very massive discs, which are unstable to against their own self-gravity, i.e.,

$$Q \equiv \frac{c_s \Omega}{\pi G \Sigma} < Q_{crit}. \tag{1.75}$$

instabilities lead to one of two outcomes. Either the disc settles into a quasi steady state, where the instability manifests as spiral density waves, or the disc will fragment. The boundary between these two outcomes has been studied in local simulations (Gammie, 2001), and global simulations (Rice et al., 2003). Both studies found that the disc cannot support stable angular momentum transport via spiral density waves if the cooling time in the disc is below some critical value,

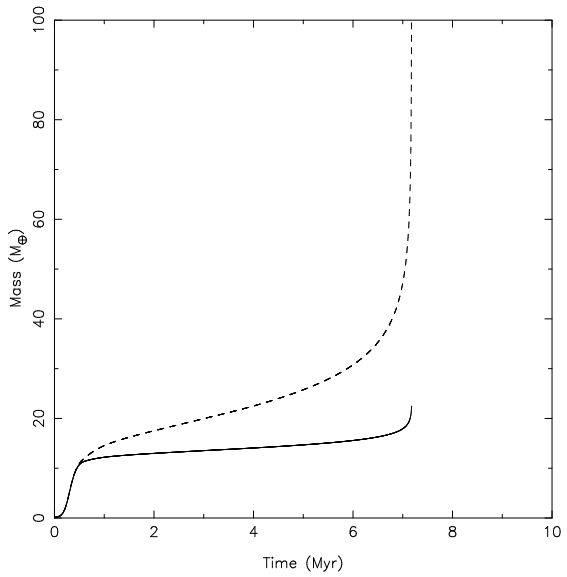

Figure 1.11 *The evolution of core mass (solid line) and total planet mass (dashed line) for an object at 5.2AU in a simplified version of the Pollack core accetion simulation from Rice et al. (2003).*

$$t_{c,crit} < 3\Omega^{-1}. \tag{1.76}$$

Alternatively this can be expressed as a critical shear stress α using,

$$\alpha = \frac{4}{9\gamma(\gamma-1)\Omega t_c}, \tag{1.77}$$

where $\alpha_{crit} \sim 0.1$, depending on the ratio of specific heats, γ, adopted. Recent studies suggest that this threshold may not be fully converged, with recent high resolution simulations suggesting that the critical cooling time, $t_{c,crit}$ may exceed $10\Omega^{-1}$ (Meru & Bate, 2011). It has, however, been suggested that this result is numerical (Paardekooper et al., 2011; Lodato & Clarke, 2011; Rice et al., 2012). Paardekooper (2012) do, however, suggest that there may be an intermediate range of cooling times for which fragmentation may be stochastic, observing fragmentation in some simulations with cooling times as high as $t_c = 20\Omega^{-1}$. Much of this discrepancy in the numerically obtained fragmentation limit arises from the treatment of shock in high resolution simulations, a problem discussed further in Chapter 2. Regardless of the precise value of the fragmentation

threshold, it is widely accepted that there is a critical value for t_c above which the disc will not fragment, as the physical justification for this boundary is well understood.

Therefore for fragmentation to occur we require both $Q < Q_{crit}$ and $t_{cool} < t_{cool,crit}$. How often these conditions are actually met in protoplanetary discs has not yet been determined via observations, the first is likely satisfied for young discs in the Class I phase however the second is less well understood. In the inner regions of the disc where the disc is exposed to large amounts of heating by the central star predicted values of t_c are much larger than $t_{c,crit}$, preventing fragmentation, but this is not necessarily the case in the outer regions ($r > 50$AU) of the disc (Rafikov, 2005; Clarke, 2009). Therefore any planets formed by gravitational instability are likely to be massive, at large initial orbital radii, though as we discuss in the following section, processes in the disc can cause planets to drift inwards, possibly accounting for the observed distribution of extrasolar planets.

1.5 Migration

Regardless of the which of the two proposed mechanisms through which planets form, it is clear that at some point in their evolution, planets will co-exist with a gaseous disc. As we will see, the gravitational interaction between the planet and the disc can have a significant effect on the evolution of the planets orbit. Any complete theory of planet formation must be able to account for this stage of the planets evolution. Indeed radial motion of planets within discs can help alleviate potential problems for planet formation theories.

1.5.1 Impulse Approximation

Although the physics describing the gravitational interaction between a planet and the surrounding disc is complicated, much insight can be gained by simply considering the interaction as a close encounter between two bodies. By calculating the change in angular momentum that occurs as a parcel of gas is

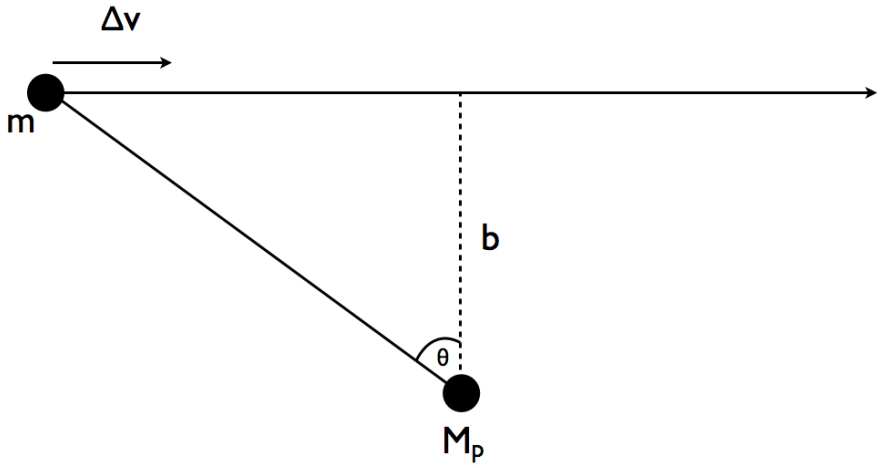

Figure 1.12 *A parcel of gas of mass m passes by a planet with an impact parameter (distance of closest approach) b and a relative velocity Δv.*

deflected by a planet, we can estimate the rate at which angular momentum is transported due to the planet. This is known as the impulse approximation.

Starting from the setup shown in Figure 1.12, we consider the gravitational interaction between a planet of mass M_p and a parcel of gas m in the rest frame of the planet. The parcel of gas has some velocity Δv relative to the planet and passes by the the planet with an impact parameter b. The component of gravitational force which is perpendicular to the gas' velocity is,

$$F_\perp = \frac{GmM_p}{d^2}\cos\theta, \tag{1.78}$$

where d is the instantaneous separation between the two bodies. By defining time $t = 0$ at $d = b$, then the distance travelled along the trajectory is simply $\Delta v t$, then the perpendicular component of the gravitational force is,

$$F_\perp = \frac{GmM_p}{b^2}\left[1 + \left(\frac{\Delta v t}{b}\right)^2\right]^{-\frac{3}{2}}. \tag{1.79}$$

The change to the perpendicular velocity of the gas, $\delta v_\perp$ is,

$$\delta v_\perp = \int_{-\infty}^{\infty} \frac{F_\perp}{m} \mathrm{d}t \tag{1.80}$$

evaluating this integral gives us,

$$\delta v_\perp = \frac{2GM_p}{b\Delta v}. \tag{1.81}$$

This increase in radial velocity corresponds to a decrease in parallel velocity. By equating the kinetic energy before and after the interaction we obtain.

$$\Delta v^2 = \delta v_\perp^2 + (\Delta v - \delta v_\parallel)^2. \tag{1.82}$$

If the deflection angle is small we then obtain,

$$\delta v_\parallel \simeq \frac{1}{2\Delta v} \left(\frac{2GM_p}{b\Delta v} \right)^2. \tag{1.83}$$

For a planet of semi-major axis a, the change in angular momentum per unit mass for the gas is

$$\Delta j = \frac{2G^2 M_p^2 a}{b^2 \Delta v^3}. \tag{1.84}$$

The effect of this change in angular momentum will depend on whether the gas is interior or exterior to the planets orbit. If the gas is exterior to the planet, then the planet will overtake the gas as it orbits faster. The resulting reduction in Δv results in the gas gaining angular momentum from the planet. The planet will tend to drift inwards, whilst the gas is repelled outwards. Alternatively if the gas is interior to the planet, the reduction in Δv results in the gas losing angular momentum to the planet. The interior gas is repelled further into the disc, however the planet migrates outward. The net direction of migration will depend on which of these effects dominates.

In order to obtain the total torque on the planet we first consider an annulus gas of width db exterior to the planet. The total mass of gas enclosed in this annulus

is,

$$\mathrm{d}m = 2\pi a \Sigma \mathrm{d}b. \tag{1.85}$$

where Σ is the surface density of gas within the annulus. If the gas has some angular velocity Ω, and the planet has an angular velocity Ω_p then the planet will encounter all the gas in the annulus in a time,

$$\Delta t = \frac{2\pi}{|\Omega - \Omega_p|}. \tag{1.86}$$

Provided $b << a$, we can re-write $|\Omega - \Omega_p|$ as,

$$|\Omega - \Omega_p| \simeq \frac{3\Omega_p}{2a} b \tag{1.87}$$

Taking our previous expression for Δj, we then multiply by $\mathrm{d}m$ and divide by Δt, then integrate with respect to the impact parameter b to obtain an expression for the total torque,

$$\frac{\mathrm{d}J}{\mathrm{d}t} = -\int_{b_{min}}^{\infty} \frac{8G^2 M_p^2 a \Sigma}{9\Omega_p^2 b^4} \mathrm{d}b \tag{1.88}$$

Evaluating this integral gives an expression for the total torque exerted by the outer disc,

$$\frac{\mathrm{d}J}{\mathrm{d}t} = -\frac{8G^2 M_p^2 a \Sigma}{27\Omega_p^2 b_{min}^3}. \tag{1.89}$$

We can repeat this procedure for the interior gas to obtain the torque from the interior part of the disc. Through this process we can can see that for most plausible surface density profiles the next torque will result in the planet losing angular momentum and drifting inward. Finally, we can estimate the timescale within which the planet will migrate inwards.

$$\tau = \frac{J}{|\mathrm{d}J/\mathrm{d}t|} \tag{1.90}$$

which gives a migration timescale of order 1Myr for a low mass planet core and around 10^5 years for a giant Jupiter mass planet. Given that typical protoplanetary discs are estimated to last a few Myrs, migration will clearly

play an important role in the early evolution of planets orbits.

1.5.2 Resonant Torques

Whilst the impulse approximation gives a useful order of magnitude calculation describing the interaction between the planet and the disc, recent analysis of this process treats the planet as a linear perturbation to a fluid disc. This allows us to express the angular momentum exchange as the sum of individual torques exerted at resonant locations within the disc.

In general a resonance occurs when the characteristic frequency of the planet matches a frequency within the disc. The simplest case is that where the orbital frequency of the planet Ω_p matches the orbital frequency of the gas in the disc, $\Omega(r)$

$$\Omega(r) = \Omega_p \tag{1.91}$$

Such a resonance is known as a co-rotation resonance. If we ignore the radial pressure gradient in the disc, which can cause the gas in the disc to orbit at sub-Keplarian velocities the co-rotation resonance is located on the same orbit as the planet.

The other type of resonance we must consider is a Lindblad resonance. Here the gas in the disc is excited at its natural frequency,

$$m[\Omega(r) - \Omega_p] = \pm\Omega(r) \tag{1.92}$$

for integer values of m. This gives resonances located at

$$r_L = \left(1 \pm \frac{1}{m}\right)^{\frac{2}{3}} a \tag{1.93}$$

1.5.3 Types of Migration

If the resonance locations are known the total torque on the planet can be calculated by summing up the individual torque from each resonance. The strength of the torque at each location is determined by two factors, the intrinsic strength of the resonance and the amount of gas present at the location.

The intrinsic strength of each resonance can be obtained from theory. The amount of gas present at the location of each resonance will vary as the disc evolves. From this we obtain two limiting cases.

Type I Migration

Type I Migration occurs for low mass planets where the interaction between the planet and the disc is relatively weak. In this case the planets presence does not significantly alter the structure of the disc. The planet remains embedded within the disc and material is present throughout the disc. In this regime we can then evaluate, for a given disc structure, the total torque on the planet. The perturbations are proportional to the planet mass M_p, resulting in torque varying as M_p^2 as obtained by the impulse approximation in section 2. Figure 1.13 shows a simulation of a disc interacting with a low mass planet in the type I regime. The planets presence in the disc causes a wake of enhanced surface density trailing out into the disc and leading into the centre. The gravitational back reaction of this wake on the planet exerts a torque on the planet.

Tanaka et al (2002) computed that for a disc with a surface density profile of

$$\Sigma(r) \propto r^{-q} \tag{1.94}$$

the total torque on the planet is given by

$$\frac{\mathrm{d}J}{\mathrm{d}t} = -(1.36 + 0.54q)\left(\frac{M_p}{M_*}\right)^2\left(\frac{h}{r}\right)^{-2}\Sigma a^4\Omega_p^2 \tag{1.95}$$

for a planet of mass M_p orbiting a star of mass M_* at a radius a with angular frequency Ω_p. This expression for the torque is often employed to estimate the

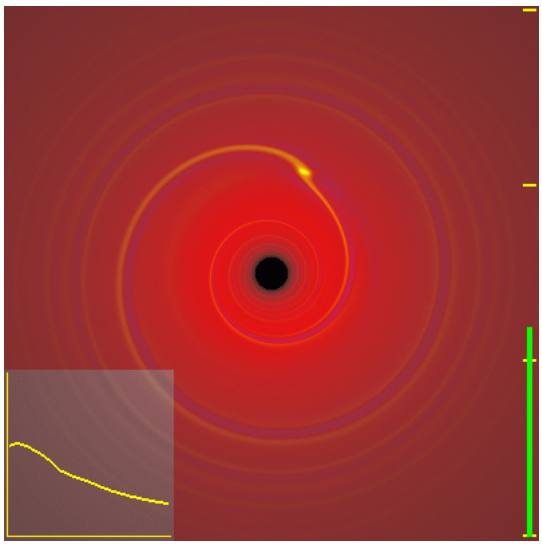

Figure 1.13 *A low mass planet interacting with the gaseous disc. We see a faint spiral structure in the disc due to the presence of the planet, however the planet does not cause any major change to the structure in the disc. The plot in the lower left hand corner shows the surface density profile within the disc. Figure taken from Armitage (2010)*

effect of type I migration however it should be noted that it assumes an isothermal disc and neglects non-linear effects. Regimes where these effects are important can render this expression invalid.

Type II Migration

As we have seen from both the impulse approximation and the expression for the type I torque above, the torque exerted by the planet on the disc in the type I regime scales as M_p^2. As the planet grows this torque grows large enough that the planets presence can no longer be simply treated as a perturbation to the disc, and starts to modify the structure of the disc in the vicinity of the planets orbit. As the main effect of the torque is to transfer angular momentum radially outward within the the disc this causes gas interior to the planet to lose angular momentum and fall inward, whilst gas exterior to the planet gains angular momentum and moves outward. This results in a gap opening around the planets orbit. This can be seen in figure 1.14. Here we see the planets influence has significantly altered

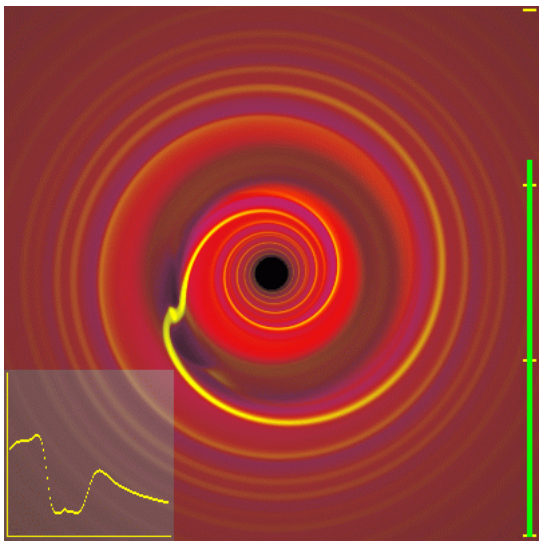

Figure 1.14 *A high mass planet of mass $M \sim M_J$ interacting with the disc. Here the spiral structure emanating from the planet is much more pronounced than in the low mass case. In addition to this the structure of the disc has been drastically altered by the planets presence, with a gap starting to open up around planets orbit. Figure taken from Armitage (2010)*

the structure of the disc around the orbit of the planet, causing a gap to open.

In order to estimate the mass at which a planet must grow to before it begins to open a gap we must consider the two processes which are responsible for opening and closing gaps in the disc . The torque that the planet exerts on the disc always tends to open a gap, but this is opposed by the viscosity in the disc, which acts to diffusively smooth out sharp radial gradients in the disc.

The disc opening timescale can be estimated by considering the amount of angular momentum required to eject all the material from an annulus in the disc between a and $(a + h)$,

$$\Delta J = 2\pi a \Sigma \frac{\mathrm{d}l}{\mathrm{d}r}\bigg|_a h^2 \tag{1.96}$$

where l is the angular momentum per unit mass of gas in a Keplarian orbit. From this we can approximate the gap opening timescale,

$$t_{open} = \frac{\Delta J}{|\mathrm{d}J/\mathrm{d}t|}. \tag{1.97}$$

where we can estimate $\mathrm{d}J/\mathrm{d}t$ from the expression obtained via the impulse approximation.

In order to estimate the timescale on which the gap will close, we must consider the evolution of Σ due to internal angular momentum transport within the disc. By considering the rate of change of the mass within an annulus in the disc, it can be shown that the continuity equation is,

$$r\frac{\partial \Sigma}{\partial t} + \frac{\partial}{\partial r}(r\Sigma v_r) = 0. \tag{1.98}$$

Similarly, conservation of angular momentum gives,

$$r\frac{\partial}{\partial t}(r^2\Omega\Sigma) + \frac{\partial}{\partial r}(r^2\Omega \cdot r\Sigma v_r) = \frac{1}{2\pi}\frac{\partial \Gamma}{\partial r}. \tag{1.99}$$

where the torque Γ for a viscous fluid, with kinematic viscosity ν, is given by,

$$\Gamma = 2\pi r \cdot \nu\Sigma r\frac{\mathrm{d}\Omega}{\mathrm{d}r} \cdot r \tag{1.100}$$

Combining equations 1.98 and 1.99, it can be shown, for a Keplarian potential ($\Omega \propto r^{-3/2}$) that the evolution equation for the surface density of a disc due to internal angular momentum transport is,

$$\frac{\partial \Sigma}{\partial t} = \frac{3}{r}\frac{\partial}{\partial r}\left[r^{1/2}\frac{\partial}{\partial r}(\nu\Sigma r^{1/2})\right]. \tag{1.101}$$

The corresponding timescale for a material to cross a distance Δr due to viscous diffusion is then simply,

$$\tau_v = \frac{\Delta r^2}{\nu}. \tag{1.102}$$

For our gap of width h the closing timescale is then,

$$t_{close} = \frac{h^2}{\nu}. \tag{1.103}$$

By equating the gap opening and closing timescales we can estimate the minimum mass of planet required to open a gap in the disc. By defining the ratio of the planets mass to the stars mass, $q \equiv M_p/M_*$ we obtain an expression for the critical mass ratio,

$$q_{crit} = \left(\frac{27\pi}{8}\right)^{\frac{1}{2}} \left(\frac{h}{r}\right)^{\frac{5}{2}} \alpha^{\frac{1}{2}}. \tag{1.104}$$

For a typical disc, this gives $q_{crit} = 2 \times 10^{-4}$, which is equivalent to a Saturn mass planet around a solar mass star.

Once a gap has been opened, the only torques which need to be considered are due to a small number of low m Lindblad resonances. The edges of the gap are then defined by the locations of the lowest m resonance capable of holding back the viscous inflow of gas. As gas flows from the outer boundary inward it runs up against the barrier created by planetary torque at the outer edge of the gap. In order to prevent the gas from flowing into the gap the planet must impart angular momentum to the gas, which must come from the inner disc. This loss of angular momentum causes the gas in the inner disc to recede further. In order for the edges of the gap to remain at the resonant locations, the planet itself must move inward with the gas in the disc. The result is that a planet migrating in the type II regime will move inward at the same rate as the local gas disc,

$$v_r \propto -\frac{\nu}{r} \tag{1.105}$$

In the type II regime, the migration rate is independent of the mass of the planet.

1.5.4 Consequences of Migration

To summarise, we see that both types of migration can have a significant effect on both the planet in the disc, and the structure of the disc itself. Here we detail the major effects of each type,

- **Type I Migration** - Type I migration tends to be very rapid, acting on timescales of $\sim 10^5$ years. In fact type I migration is so rapid that it actually makes it difficult to form giant planet cores of around 10 Earth

masses without the planet drifting all the way into the central star. It is therefore often assumed that there is some process damping the full effect of type I migration, however the physical origin of this is unclear. Despite this, small amounts of inward drift can actually be highly beneficial to the planet formation process, by constantly providing the planet with fresh material to accrete, preventing the stagnation of its growth. Investigating how planetesimals can be shielded from this strong inward drift is one of the key problems this thesis attempts to address.

- **Type II Migration** - Type II migration tends to be much slower than type I, typically acting on timescales of $\sim$ 1Myr. Type II migration is often employed to describe the hot Jupiter's often seen around stars as no current theory of planet formation can form such massive planets in-situ. Despite being slower than type I migration, the type II process can still cause planets to be lost to the central object if they form very early in the disc.

1.6 Summary

This Chapter has outlined the fundamental properties of accretion discs that arise during the star formation process and described the physical processes which are thought to play a major role in the evolution of the disc and the formation of planets within the disc. The aim of the work contained in this thesis draws is to gain an improved understanding of grain growth and planetesimal formation at early evolutionary stages when the disc is still self-gravitating. As mentioned in Section 1.4, planetesimal formation must be rapid in order to match observations for two reasons, to avoid the rapid radial infall of solid objects, especially in the meter-size range, and to provide a sufficiently large reservoir of solid material for terrestrial planets and gas giants to form before the gas in the disc is dispersed. Specifically, motivated by the work of Clarke & Lodato (2009), the dynamical behaviour of particles embedded in a self-gravitating disc is studied using a local shearing-sheet approximation. Clarke & Lodato (2009) concluded, based on analytical estimations, that in realistic self-gravitating discs,

particle agglomeration will be restricted to the outer regions of the disc (at radii of several tens of AU). At such large separations, the cooling time-scale is relatively short and hence density enhancements in spiral features are strong enough to concentrate particles on a local dynamical (orbital) time scale – the lifetime of such features. This work builds on these estimates and studies in greater detail, via numerical simulations, the ability of spiral waves which arise from gravitational instabilities to support the planet formation process.

The remainder of this thesis is arranged as follows, Chapter 2 gives an overview of the tools used to study protoplanetary disc evolution, including an overview of hydrodynamics, the local shearing sheet approximation and its effects on the hydrodynamical equations and outlines the pencil code, which is used to conduct the numerical simulations in the subsequent chapters. Chapter 3 studies the basic particle trapping properties of spiral density waves which form as a result of gravitational instabilities in massive discs. Chapter 4 expands on the work contained in Chapter 3, exploring how planetesimals can form within spiral density waves due to their particle trapping properties. Chapter 5 explores how the vortices which can form in self gravitating discs may also be able to assist planetesimal formation due to their particle trapping properties. Chapter 6 outlines recent work which explores the possibility of expanding these findings from 2D shearing sheets into 3D shearing boxes. In Chapter 7 these findings are summarised and their relation to the wider field of planet formation is discussed.

Chapter 2

Model

This Chapter outlines the numerical methods used for the work outlined in this thesis. As noted at the end of Chapter 1, the work detailed in subsequent chapters explores how gravitational instabilities that are present in massive discs present in the early stages of the star formation process can seed the disc with a large number of planetesimal sized objects, and possibly even larger bodies, which could go on to form terrestrial planets or become the cores of giant planets as detailed by the core accretion model of planet formation. This Chapter covers three key aspects of the model used in this work, the basic hydrodynamical equations, which are used to model the gaseous component of the accretion disc, the shearing-sheet approximation, which modifies these equations to describe gas dynamics for a small 'local' region of an accretion disc. Finally the PENCIL code, which is used to solve these equations numerically is introduced, and some of the basic numerical methods used in the PENCIL code are outlined.

2.1 Hydrodynamics and the Shearing Sheet Approximation

The work outlined in subsequent chapters treats the gaseous component of accretion discs as a compressible fluid, therefore the evolution of the physical

properties of the disc are described by the hydrodynamical equations. These equations are partial differential equations which express conservation laws which govern the gas. By considering a flow through an arbitrary volume, conservation of mass requires that the variation of mass within this volume must be due to inflow or outflow of mass, this yields the continuity equation,

$$\frac{\partial \rho}{\partial t} + \nabla \cdot (\rho \, \mathbf{u}) = 0, \tag{2.1}$$

where ρ is the volume density of the gas, which has a velocity $\mathbf{u}$. By considering conservation of momentum within the volume we obtain the equation for the evolution of the gas velocity,

$$\frac{\partial \mathbf{u}}{\partial t} + (\mathbf{u} \cdot \nabla)\mathbf{u} = -\frac{1}{\rho}\nabla P. \tag{2.2}$$

where P is the pressure of the gas, with an equation of state, $P = (\gamma - 1)U$, for a gas with ratio of specific heats γ. Finally conservation of energy gives the energy evolution equation,

$$\frac{\partial U}{\partial t} + \mathbf{u} \cdot \nabla U = -\frac{P}{\rho}\nabla \cdot \mathbf{u} \tag{2.3}$$

where U is the internal energy of the gas.

When applied to an accretion disc, these equations have to be modified to account the background dynamics of the disc. The processes which the work presented in this thesis studies operate on length scales much smaller than the physical extent of the disc. In order to study such small-scale or 'local' processes, the 'shearing sheet' formalism is adopted. This formalism was first employed by Goldreich & Lynden-Bell (1965). From a simulation perspective, this local formalism allows much greater resolution than a global simulation would. The essence of the shearing sheet approximation is illustrated in Figure 2.1. Here we see the 'shearing sheet', a local region of the disc, expressed in cartesian co-ordinates (x, y) imposed on the disc, which is defined in cylindrical co-ordinates (r, ϕ), where x points radially outward and y points along the azimuthal direction. The transformations between these two co-ordinates systems are then $x = r - r_0$ and $y = r_0(\phi - \phi_0)$, where (r_0, ϕ_0) is the centre of the shearing sheet. By assuming the disc is cool, and therefore thin $(h/r \simeq c_s/(\Omega r) \ll 0.1)$ the Keplerian rotation appears as

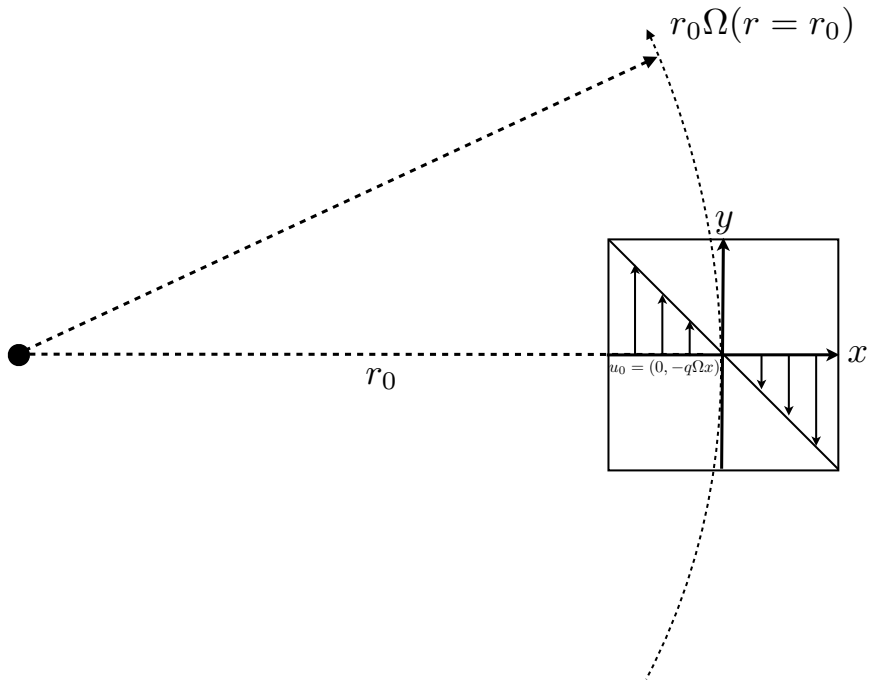

Figure 2.1 *Illustration of the local coordinate frame (x,y) used in the shearing sheet approximation, which co-rotates with the disc matter at the distance r_0 with velocity $r_0\Omega$. In this local frame, the discs Keplerian differential rotation appears as a parallel azimuthal shear flow $u_0 = (0, -q\Omega x)$.*

a parallel azimuthal shear flow across sheet and the hydrodynamical equations become,

$$\frac{\partial \rho}{\partial t} + \nabla \cdot (\rho\, \mathbf{u}) - q\Omega x \frac{\partial \rho}{\partial y} = 0, \tag{2.4}$$

$$\frac{\partial \mathbf{u}}{\partial t} + (\mathbf{u} \cdot \nabla)\mathbf{u} - q\Omega x \frac{\partial \rho}{\partial y} = -\frac{1}{\rho}\nabla P - 2\Omega(\hat{\mathbf{z}} \times \mathbf{u}) + q\Omega u_x \hat{\mathbf{y}} - \nabla\psi, \tag{2.5}$$

$$\frac{\partial U}{\partial t} + \mathbf{u} \cdot \nabla U - q\Omega x \frac{\partial U}{\partial y} = -\frac{P}{\rho}\nabla \cdot \mathbf{u}. \tag{2.6}$$

As a result of the co-ordinate transform the left hand side of each equation now

contains a shear term,

$$-q\Omega x\frac{\partial}{\partial y},$$

where the shear parameter $q = 1.5$ for Keplerian rotation profiles. In addition to this the velocity evolution equation has two additional terms on the right hand side which describe the Coriolis effect, and a term describing the gravitational potential of the disc. In the case of low mass discs, this term describing the gravitational potential of the disc is negligible. For the massive discs studied here, where gravitational instabilities set in, the gravitational potential of the disc must be calculated via Poisson's equation,

$$\nabla^2\psi = 4\pi G\rho. \tag{2.7}$$

where G is the gravitational constant.

These equations form the basis for the study of planetesimal formation in accretion discs described below, the next section outlines the numerical methods used to solve these equations, along with any further modifications made to these equations to study particular properties of the disc.

2.2 The Pencil Code

The work outlined in subsequent chapters uses numerical simulations to study planetesimal formation in self-gravitating discs. To numerically solve the hydrodynamical equations in the shearing sheet approximation the PENCIL Code is employed. This section contains a brief overview of the PENCIL Code, how it solves the hydrodynamical equations, and describe some of the other physics routines employed that have not been previously mentioned.

The PENCIL code is a grid based hydrodynamics code, which is primarily design to model weakly compressible, turbulent flows. The PENCIL code is used to solve the 2D versions of the above hydrodynamical equations on a fixed grid, along with the poisson equation for the self-gravity of the disc. In the simulations performed below, the shearing sheet spans the region $L_x \times L_y$, where $L_x = L_y = L$. The

domain is periodic in x and y, adopting the standard shearing sheet boundary conditions of Hawley et al. (1995), where grid variables $f = \Sigma, U, u_x, \delta u_y = u_y + q\Omega x$ obey,

$$f(x, y, t) = f(x, y + L, t), \tag{2.8}$$

$$f(x, y, t) = f(x + L, y - q\Omega L t, t). \tag{2.9}$$

The sheet is therefore fully periodic in x, and periodic in y, with some offset to take into account the velocity gradient present along the shearing sheet.

2.2.1 Spatial Derivatives

As previously noted, the PENCIL code uses high order derivatives. In order to achieve the high level of numerical accuracy required for modelling turbulence, sixth order spatial derivatives are used, under this scheme first and second order differentials of a variable f at a grid cell i with cell width Δx are,

$$f'_i = (-f_{i-3} + 9f_{i-2} - 45_{i-1} + 45f_{i+1} - 9f_{i+2} + f_{i+3})/(60\Delta x), \tag{2.10}$$

$$f''_i = (2f_{i-3} - 27f_{i-2} + 270_{i-1} - 490f_i + 270f_{i+1} - 27f_{i+2} + 2f_{i+3})/(180\Delta x). \tag{2.11}$$

these high order derivative schemes provide a good compromise between numerical accuracy and code efficiency.

2.2.2 Viscosity and Diffusion

The implementation of the differential equations in the code are dissipation free, have phase errors, but no amplitude errors. In order to suppress unstable modes at the grid scale that can arise due to turbulence, numerical dissipation must be introduced in order to maintain numerical stability in the code. In the simulations performed in this work, the velocity equation contains a Navier-Stokes viscosity

term,

$$\mathbf{f}_\nu = \nu(\nabla^2\mathbf{u} + \frac{1}{3}\nabla\nabla\cdot\mathbf{u} + 2\mathbf{S}\cdot\nabla\ln\,\Sigma) \tag{2.12}$$

where ν is the kinematic viscosity and $\mathbf{S}$ is the traceless rate-of-strain tensor

$$S_{ij} = \frac{1}{2}\left(\frac{\partial u_i}{\partial x_j} + \frac{\partial u_j}{\partial x_i} - \frac{2}{3}\delta_{ij}\nabla.\mathbf{u}\right). \tag{2.13}$$

Similar mass diffusion and thermal conductivity terms exist for the continuity and energy equations, however are not used in the work described below.

A related viscous heating term is also included in the energy equation,

$$H_\nu = 2\nu\Sigma\mathbf{S}^2. \tag{2.14}$$

The code works with a constant diffusion coefficient viscosity ν. If the viscosity coefficient is too small for a given resolution, the code develops wiggles and will eventually crash. A useful criterion for minimum amounts of viscosity to include in the code is given by the mesh Reynolds number based on the maximum velocity,

$$\mathrm{Re}_{\mathrm{mesh}} = \frac{\max(|\mathbf{u}|)\cdot\max(\Delta x, \Delta y)}{\nu}, \tag{2.15}$$

which should not exceed a certain value dependent on the problem being solved. Typically the largest possible value of $\mathrm{Re}_{\mathrm{mesh}}$ is around 5.

If the rms velocity becomes comparable with the speed of sound, shocks may form in the code. In such a case the mesh Reynolds number should be smaller. In order to avoid excessive viscosity in the unshocked regions, shock viscosity is also employed to concentrate the effects of a low mesh Reynolds number to only those areas where it is necessary (see below).

2.2.3 Shocks

If shocks form in the simulation, the simple Navier-Stocks viscosity described above may be insufficient to maintain stability within the code due to the presence of discontinuities across the shock fronts. To counteract this, additional shock

terms are included in the hydrodynamical equations to smooth shock fronts to avoid steep gradients creating instabilities that propagate through the code. These shock terms take the following form,

$$f_D = \zeta_D(\nabla^2\Sigma + \nabla \ln \zeta_D \cdot \nabla\Sigma). \tag{2.16}$$

Here the quantity ζ_D is defined as,

$$\zeta_D = D_{sh}\langle \max_3[(-\nabla.\mathbf{u})_+]\rangle \Delta x^2 \tag{2.17}$$

where D_{sh} is a constant defining the strength of the shock terms in the hydrodynamical equations. The term $\langle \max_3[(-\nabla.\mathbf{u})_+]\rangle$ locates the shocks within the simulation domain by identifying regions of large negative divergence in the velocity field which corresponds to the shocks. This term then revises the sign and takes the positive values (represented by the $_+$ subscript). Finally the maximum value over three grid cells is taken. The simulations performed below include a shock term in the continuity, velocity and energy equations providing mass diffusion, viscosity and heat conduction across the shock fronts.

2.2.4 Particles

The solid component of the disc is modelled as a large number of numerical superparticles, with positions $\mathbf{x} = (x_p, y_p)$ on the grid and velocities $\mathbf{v} = (\mathrm{v}_x, \mathrm{v}_y)$ relative to the unperturbed Keplerian rotation velocity $\mathbf{u_0} = (0, -q\Omega x_p)$ in the local frame. These are evolved as

$$\frac{\mathrm{d}\mathbf{x}}{\mathrm{d}t} = \mathbf{v} - q\Omega x_p \hat{\mathbf{y}} \tag{2.18}$$

$$\frac{\mathrm{d}\mathbf{v}}{\mathrm{d}t} = -2\Omega\hat{\mathbf{z}} \times \mathbf{v} + q\Omega \mathrm{v}_x \hat{\mathbf{y}} + \nabla\psi + \frac{1}{\tau_f}(\mathbf{u} - \mathbf{v}), \tag{2.19}$$

where τ_f is the friction time of the particle as outlined in Chapter 1. The first two terms in equation 2.19 represent the Coriolis Force and the non-inertial force due to shear. The third term represents the gravitational potential of the system.

The final term describes the drag force exerted by the gas on the particles which arises from the velocity difference between the two.

The drag force on the particles from the gas is calculated by interpolating the gas velocity field to the position of the particle, in a three step process. first the gas velocities are calculated at the positions of the particles, the drag force on the particles as a result of the gas is then calculated, and the back reaction of the particles on the gas is calculated if appropriate.

To interpolate the gas velocities $\mathbf{u}^{(j)}$, where the index j labels the cell on the grid which are at a position $\mathbf{x}^{(j)}$, at the positions of the particles, $\mathbf{x}^{(i)}$, a weight function, W_I, is used giving the velocity of the gas at the positions of the particles as,

$$\overline{\mathbf{u}(\mathbf{x}^{(i)})} = \sum_j W_I(\mathbf{x}^{(i)} - \mathbf{x}^{(j)})\mathbf{u}^{(j)}. \tag{2.20}$$

The weight function is normalised as $\sum_j W_I(\mathbf{x}^{(i)} - \mathbf{x}^{(j)}) = 1$, and has non-zero contributions only from cells adjacent to $\mathbf{x}^{(j)}$ Once the gas velocity at the location of the particle has been determined, it becomes trivial to calculate the drag term on the particle, i,

$$\mathbf{f}_p^{(i)} = -\frac{1}{\tau_f}\left(\mathbf{v}^{(i)} - \overline{\mathbf{u}(\mathbf{x}^{(i)})}\right), \tag{2.21}$$

where $\mathbf{v}^{(i)}$ and τ_f are the velocity and friction time of the particle.

The final step, calculating the back reaction drag force on the gas due to the particles, is done by considering Newtons third law. This gives

$$\mathbf{f}_g^{(j)} = -\frac{m_p}{\Sigma^{(j)}\Delta x \Delta y}\sum_i W_I(\mathbf{x}^{(i)} - \mathbf{x}^{(j)})\mathbf{f}_p^{(i)} \tag{2.22}$$

where m_p is the mass of a superparticle, $\Sigma^{(j)}$ is the surface density of gas in cell j and $\Delta x, \Delta y$ are the length of the cell in the x and y directions respectively.

There are several different implementations of W_I in the PENCIL code, the simplest are the nearest grid point (NGP) scheme, which assumes that particles are points like, the entirety of the particles mass is contained within the cell the particle is located in, and the cloud in cell (CIC) method, where the mass of a particle is evenly distributed to surrounding grid cells. The work in this thesis adopts the

triangular shaped cloud scheme, whereby a particles mass is assigned to a 3x3 region (in 2D) of nearby grid points as follows,

$$W_I = \begin{cases} 1 - \dfrac{\delta x_i^2}{\Delta x^2}, & |\delta x_i| < \Delta x/2, \\ \dfrac{1}{2}\left(1 - \dfrac{|\delta x_i|}{\Delta x}\right)\left(2 - \dfrac{|\delta x_i|}{\Delta x}\right), & \Delta x/2 < |\delta x_i| < 3\Delta x/2, \\ 0, & |\delta x_i| > 3\Delta x/2, \end{cases} \tag{2.23}$$

where $\delta x_i \equiv x - x_i$ is the distance from the particles location to the centre of a grid cell of width Δx. This assignment scheme, although more expensive computationally than the other two schemes, conserves momentum, which the other methods do not.

2.2.5 Time Step

The PENCIL Code uses a third order Runga-Kutta time step, which is specified in the code via the coefficients $c_{dt}, c_{dt,v}, c_{dt,s}$. The resulting Courant time step is then given by,

$$\Delta t = \min\left(c_{dt}\frac{\Delta x_{\min}}{U_{\max}}, c_{dt,v}\frac{\Delta x_{\min}^2}{D_{\max}}, c_{dt,s}\frac{1}{H_{\max}}\right). \tag{2.24}$$

Here $\Delta x_{min} = \min(\Delta x, \Delta y)$. $U_{max}, D_{max}, H_{max}$ are defined as follows,

$$U_{max} \equiv \max\left(|\mathbf{u}| + \sqrt{c_s^2 + v_A^2}\right) \tag{2.25}$$

where c_s and v_A represent the sound speed and Alfvén speed,

$$D_{max} = \max(\nu, \gamma\chi, \eta, D), \tag{2.26}$$

where ν, χ, η, D represent the strength of kinematic viscosity, thermal conductivity, magnetic diffusivity and mass diffusion. Finally H_{max} is dependent on the

numerical terms present on the right hand side of the energy equation (see below). By using a variable minimum time step in this way, numerical errors that can arise from an excessively large time step are avoided.

In addition to this, the particles also have a maximum time step which they can be evolved on. The time-step constraint set by the drag force is,

$$\Delta t_{drag} = \min\left(c_{dt,p}\frac{\tau_f}{(1+\epsilon)}\right), \tag{2.27}$$

where ϵ is the local dust-to-gas ratio. As the dust-to-gas ratio increases, the allowed time-step decreases.

The coefficients $c_{dt}, c_{dt,v}, c_{dt,s}, c_{dt,p}$ are user defined constants whose value is equal to or less than unity, these coefficients allow for an extra layer of robustness in the time step calculation, as the time step the code is evolved on will be less than the minimum required to avoid numerical errors. This work takes $c_{dt} = c_{dt,v} = c_{dt,s} = c_{dt,p} = 0.5$.

2.2.6 Poisson Equation

The gravitational potential terms in the gas velocity equation and the particle velocity equation are calculated by inverting the Poisson equation, which in 2D for a razor thin disc is,

$$\nabla^2\psi = 4\pi G\Sigma'\delta(z). \tag{2.28}$$

In Equation 6.9 the surface density Σ' represents either the perturbed gas surface density $\Sigma - \Sigma_0$ or the particle surface density Σ_p. This is then solved via a Fourier method. Here, the surface density is Fourier transformed from the (x, y) plane to the (k_x, k_y) plane, the solution for a single Fourier density mode of wavenumber $\mathbf{k} = (k_x, k_y)$and Fourier amplitude Σ_k is then,

$$\psi_k = -\frac{4\pi G\Sigma_k}{k^2}, \tag{2.29}$$

for $k = |\mathbf{k}| > 0$, the full potential is then given by,

$$\psi = \sum_k \psi_k \mathrm{e}^{i\mathbf{k}\cdot\mathbf{x}}. \tag{2.30}$$

Due to the velocity gradient present in the shearing sheet, the sheet is not completely periodic in x and y, with the radial (x) direction being shear periodic. Connected points along the inner and outer boundaries are separated by a distance,

$$\Delta y(t) = q\Omega L t, \tag{2.31}$$

to take this into account, the Poisson solver implemented in the PENCIL code initially applies a Fast Fourier Transform (FFT) in the periodic y-direction. This is then shifted by an amount $\delta y(x) = \Delta y(t)x/L$ to make the x-direction periodic before a FFT is applied to the x-direction. This process is then reversed after the potential is calculated by performing these steps in the opposite order. The PENCIL code also follows the argument of Gammie (2001) where wave numbers above a limit k_{max} must be excluded from the solution to the Poisson equation in the shearing box in order to keep the gravitational acceleration approximately isotropic at small scales in the presence of shear. This limit is at $k_{max} = \sqrt{2}k_{Ny}$, where k_{Ny} is the Nyquist wavenumber.

Chapter 3

Particle Trapping in Self-Gravitating Discs

This Chapter was published as Gibbons et al. (2012), Monthly Notices of the Royal Astronomical Society, Volume 426, Issue 2, pp. 1444-1454

3.1 Introduction

There are currently two models for the formation of gas giant planets in circumstellar discs. The most widely accepted is the core accretion model (Pollack et al., 1996). Here, a core of solid material grows via a series of collisions until it becomes massive enough to accrete a gaseous envelope from the disc (Pollack et al., 1996). This must occur before the disc is depleted of gas, a process which is observationally estimated to take $\sim 10^7$ years (Haisch et al., 2001).

A major area of uncertainty in the core accretion model lies in the growth of objects from small dust grains to kilometre-sized planetesimals, which form the building blocks of planet cores. Many numerical models of the core accretion process assume that a large population of planetesimals has already formed.

The dynamics of the smaller particles that ultimately grow to form these

kilometre-sized planetesimals is, however, governed by the drag force that arises from the velocity difference between the solid particles and the surrounding gas.

Within a few scale heights of the disc mid-plane, the pressure gradient within the disc tends to be negative. This causes the gas to orbit with sub-Keplerian velocities. The dust is not affected by the gas pressure gradient and orbits at Keplerian velocities. The drag force on the dust particles that arises from this velocity difference results in the solids losing angular momentum to the disc and drifting inward at a rate that depends on the particles' size (Weidenschilling, 1977; Nakagawa et al., 1986). For very small grain sizes, the dust is tightly coupled to the gas in the disc and the radial drift velocities are small. For very large objects, the solids are decoupled from the gas, move in approximately Keplerian orbits and again have very small drift velocities. Particles in the intermediate size range can, however, have large drift velocities. Although the exact size range depends on the local properties of the disc, drift velocities can exceed 10^3cm/s for objects with sizes between 1cm and 1m (Weidenschilling, 1977). In order to prevent dust particles from spiralling inward into the central star before it decouples from the gas, solid material must rapidly grow from small centimetre-sized grains to large decametre sized objects. Laibe et al. (2012) do however suggest that there may be surface density and temperature profiles for which particles may survive this inward migration.

The alternative disc instability model requires that planets be able to form via direct gravitational collapse of the gaseous part of the disc, and does not require the presence of a solid core (Boss, 1998). Gravitational instabilities set in, for a razor–thin disc, when the sound speed c_s, Keplerian rotation frequency, Ω and the surface density of the disc satisfy (Toomre, 1964)

$$Q \equiv \frac{c_s \Omega}{\pi G \Sigma} < 1. \tag{3.1}$$

This requires that the disc be relatively massive compared to its parent star. In the event that a disc is susceptible to such instabilities, one of two outcomes may occur. If the cooling time is long, the disc will settle into a quasi-steady state, where the cooling balances the heating generated by gravitoturbulence (Gammie, 2001). For short cooling times the disc may fragment, forming gas giant

planets. The critical cooling time below which fragmentation occurs is commonly taken to be $t_{c,crit} = 3\Omega^{-1}$ (Gammie, 2001; Rice et al., 2003) however recent studies suggest that this threshold may not be fully converged, with recent high resolution simulations suugesting that the critical cooling time, $t_{c,crit}$ may exceed $10\Omega^{-1}$ (Meru & Bate, 2011). It has, however, been suggested that this result is numerical (Paardekooper et al., 2011; Lodato & Clarke, 2011; Rice et al., 2012). Paardekooper (2012) do, however, suggest that there may be an intermediate range of cooling times for which fragmentation may be stochastic, observing fragmentation in some simulations with cooling times as high as $t_c = 20\Omega^{-1}$.

Although very few Class II protostars are observed to have sufficiently massive discs to be susceptible to gravitational instabilities (Beckwith & Sargent, 1991), observations indicate that during the Class 0 and Class I phases, massive discs may be much more common around protostars (Rodriguez et al., 2005; Eisner et al., 205; Greaves & Rice, 2010). However, even though a massive circumstellar disc is thought to be present at early times in the star formation process (Machida & Matsumoto, 2011), it is not clear that such discs can cool quickly enough to directly form giant planets via fragmentation.

Even if the cooling times present within discs are too long to allow giant planets to form via fragmentation, it is expected that circumstellar discs are self-gravitating in their early stages (Lin & Pringle, 1987, 1990). If this is the case, these instabilities take the form of non-axisymmetric spiral structures, which have been shown to be highly efficient at transporting angular momentum outward (Lodato & Rice, 2004; Forgan et al., 2011).

It has been proposed that these spiral waves may be highly effective at trapping the solids in the disc. The gas pressure gradient changes from positive to negative across these spiral wave structures, which results in sub-Keplerian velocities on one side of the wave, and super-Keplerian on the other. The drag force then causes dust grains to drift toward the density/pressure maxima at the centre of the waves. This can eliminate two problems currently challenging theories of planet formation. Firstly, by trapping large amounts of solid material within a spiral arm the local density of solids is much higher than the average within the disc, leading to the faster creation of planetesimals. Trapping particles in these

local pressure maxima can also shield growing objects from the rapid inward drift described previously that can potentially stop large objects forming before they drift into the central object. Rice et al. (2004) showed, using global simulations, that the surface density of certain particle sizes can be enhanced by a factor of over 100 in the spiral wave structure. Rice et al. (2006) estimate that such an augmentation in the surface density of solids will lead to the creation of km-scale planetesimals through the self-gravity of the solids. Clarke (2009) however noted that the simulations carried out in Rice et al. (2004) and Rice et al. (2006) assumed a constant cooling time throughout the disc, and that the conditions required to achieve such high solid concentrations may be restricted to very large orbital radii in discs that incorporate a more realistic cooling.

Similar concentrations of particles are also seen in the presence of other density enhancements in the gas, such as those caused by magneto-rotational turbulence (Johansen et al., 2006), as well as vortices (Godon & Livio, 2000; Klahr & Bodenheimer, 2003). Increased particle concentrations are thought to aid planetesimal formation in two ways, the enhanced collision rate displayed by Rice et al. (2004) will aid planetesimal formation (provided collisions are constructive). Secondly, the presence of high dust densities may actually lead to the formation of large planetesimals through direct gravitational collapse of the solids (Rice et al., 2006; Johansen et al., 2007, 2011).

The goal of the work presented in this Chapter is an improved understanding of grain growth and planetesimal formation at early evolutionary stages when the disc is still self-gravitating. Specifically, motivated by the work of Clarke & Lodato (2009), we study dynamical behaviour of particles embedded in a self-gravitating disc using a local shearing-sheet approximation. As mentioned above, Clarke & Lodato (2009) concluded, based on analytical estimations, that in realistic self-gravitating discs, particle agglomeration will be restricted to the outer regions of the disc (at radii of several tens of AU). At such large separations, the cooling time-scale is relatively short and hence density enhancements in spiral features are strong enough to concentrate particles on a local dynamical (orbital) time scale – the lifetime of such features. Here, we go beyond these estimates and study in greater detail, via numerical simulations, the trapping capability of spiral waves for a wide range of disc cooling times and particle stopping times.

This allows us to see how the solids will respond to the presence of spiral density waves at various radii within the disc and also understand what minimum values of gas density enhancements are required for appreciable particle concentration to occur is spiral features.

This Chapter is arranged as follows. In Section 2 we outline the model we use in our simulations. In Section 3 we discuss the evolution of the gas and dust particles. Finally, we draw our conclusions in Section 4.

3.2 Model

To investigate the dynamics of solid particles embedded in self-gravitating protoplanetary discs, we solve the 2D local shearing sheet equations for gas on a fixed grid, including disc self-gravity as in Gammie (2001), together with the equations of motion of solids coupled to the gas solely through aerodynamic drag force. As a main numerical tool, we employ the PENCIL CODE[1]. The PENCIL CODE is a sixth order spatial and third order temporal finite difference code (see Brandenburg (2003) for full details). The PENCIL CODE treats solids as numerical super-particles (Johansen et al., 2006).

To use the local shearing sheet model, we must make two simplifying assumptions, first that the disc is cool, and therefore thin ($H/r \simeq c_s/(\Omega r) \ll 0.1$), and that the disc is razor-thin, as in Gammie (2001). In the shearing sheet approximation, disc dynamics is modelled in the local Cartesian coordinate frame centred at some arbitrary radius, r_0, from the central object and rotating with the disc's angular frequency, Ω, at this radius. In this local frame, the x-axis points radially away from the central object, the y-axis points in the azimuthal direction of the disc's differential rotation, which in turn manifests itself as an azimuthal parallel flow characterised by a linear shear, q, of background velocity, $\mathbf{u}_0 = (0, -q\Omega x)$. Our simulation domain spans the region $-L_x/2 \leq x \leq L_x/2$, $-L_y/2 \leq y \leq L_y/2$. We adopt the standard shearing-sheet boundary conditions (Hawley et al., 1995),

[1]See http://code.google.com/p/pencil-code/

namely for any variable f we have

$$f(x, y, t) = f(x, y + L, t) \tag{3.2}$$

$$f(x, y, t) = f(x + L, y - q\Omega Lt, t). \tag{3.3}$$

These boundary conditions apply to all grid variables except the azimuthal component of the velocity, u_y, which must be adjusted to account for the relative shear between neighbouring boxes. The azimuthal velocity on the radial boundary is,

$$v_y(x, y, t) = v_y(x + L, y - q\Omega Lt, t) + q\Omega L. \tag{3.4}$$

The shear parameter $q = 1.5$ for Keplerian rotation.

3.2.1 Gas Density

In this local model, the continuity equation for the gas surface density Σ is

$$\frac{\partial \Sigma}{\partial t} + \nabla.(\Sigma \mathbf{u}) - q\Omega x \frac{\partial \Sigma}{\partial y} - f_D(\Sigma) = 0 \tag{3.5}$$

where $\mathbf{u}(u_x, u_y)$ is the gas velocity relative to the background Keplerian flow, which in our domain manifests itself as an azimuthal flow with linear shear of velocity $\mathbf{u}_0 = (0, -q\Omega\mathbf{x})$. Due to the high-order numerical scheme of the PENCIL CODE we also include a diffusion term, f_D, to ensure numerical stability and capture the effects of shocks,

$$f_D = \zeta_D(\nabla^2\Sigma + \nabla \ln \zeta_D \cdot \nabla\Sigma). \tag{3.6}$$

Here the quantity ζ_D is defined as,

$$\zeta_D = D_{sh}\langle \max_3[(-\nabla.\mathbf{u})_+]\rangle \Delta x^2 \tag{3.7}$$

where D_{sh} is a constant defining the strength of shock diffusion as outlined in Appendix B of Lyra et al. (2008).

3.2.2 Gas Velocity

The equation of motion for the gas velocity $\mathbf{u}$ relative to the background Keplerian flow $\mathbf{u}_0$ takes the form

$$\frac{\partial \mathbf{u}}{\partial t} + (\mathbf{u}\cdot\nabla)\mathbf{u} - q\Omega x\frac{\partial \mathbf{u}}{\partial y} = -\frac{\nabla P}{\Sigma} - 2\Omega\hat{\mathbf{z}}\times\mathbf{u} + q\Omega u_x\hat{\mathbf{y}} + 2\Omega\Delta v\hat{\mathbf{x}} - \nabla\psi + \mathbf{f}_\nu(\mathbf{u}), \quad (3.8)$$

where P is the two-dimensional pressure and ψ is the gravitational potential of the sheet due to the gas surface density perturbation $\Sigma - \Sigma_0$. The left hand side of equation 3.8 includes terms from the velocity field $\mathbf{u}$ and the Keplerian flow. The first term on the right hand side of the equation is the force due to the pressure gradient. The second and third terms represent the Coriolis effect/shear induced by the choice of coordinate system. The fourth term mimics a global radial pressure gradient, which reduces the orbital speed of the gas by Δv and is responsible for the inward migration/drift of solids in an unperturbed disc. The main purpose for the inclusion of this term here is to see how the radial drift affects the concentration of particles by spiral density waves. The fifth term represents the effect of the gravitational potential of the disc. Finally we include an explicit viscosity term

$$\mathbf{f}_\nu = \nu(\nabla^2\mathbf{u} + \frac{1}{3}\nabla\nabla\cdot\mathbf{u} + 2\mathbf{S}\cdot\nabla\ln\,\Sigma) + \zeta_\nu[\nabla(\nabla.\mathbf{u}) + (\nabla\ln\,\Sigma + \nabla\ln\,\zeta_\nu)\nabla.\mathbf{u}], \quad (3.9)$$

which contains both Navier-Stokes viscosity and a bulk viscosity for resolving shocks. Here $\mathbf{S}$ is the traceless rate-of-strain tensor

$$S_{ij} = \frac{1}{2}\left(\frac{\partial u_i}{\partial x_j} + \frac{\partial u_j}{\partial x_i} - \frac{2}{3}\delta_{ij}\nabla.\mathbf{u}\right) \quad (3.10)$$

and ζ_ν is the shock viscosity coefficient analogous to the shock diffusion coefficient defined in equation 3.7 with $\nu_{sh} = D_{sh}$

3.2.3 Self-gravity

The gravitational potential of the gas is found by inverting the Poisson equation for a 2D (razor thin) disc

$$\nabla^2\psi = 4\pi G(\Sigma - \Sigma_0)\delta(z) \tag{3.11}$$

using the Fast Fourier Transform method outlined in Chapter 2. Note that since the gravitational potential is associated with density fluctuations, only the perturbed surface density $\Sigma - \Sigma_0$ enters equation 3.11.

3.2.4 Entropy

The PENCIL CODE uses entropy, s, as its main thermodynamic variable, rather than internal energy, U, as used by Gammie (2001). The equation for entropy evolution is

$$\frac{\partial s}{\partial t} - q\Omega x\frac{\partial s}{\partial y} + (\mathbf{u}.\nabla)s = \frac{1}{\Sigma T}\left(2\Sigma\nu\mathbf{S}^2 - \frac{\Sigma c_s^2}{\gamma(\gamma-1)t_c} + f_\chi(s)\right) \tag{3.12}$$

where the first term on the right hand side is the viscous heating term and the second term is an explicit cooling term. Here we assume the cooling time t_c to be constant throughout the sheet and take its value to be sufficiently large that the disc does not fragment and achieves a quasi-steady state. The final term on the right hand side is a shock dissipation term analogous to that outlined for density.

3.2.5 Dust Particles

The dust particles are treated as a number of massless numerical test-particles, using the implementation for dust particles of Johansen et al. (2007). In this implementation dust particles have positions $\mathbf{x} = (x_p, y_p)$ on the grid and velocities $\mathbf{v} = (\mathrm{v}_x, \mathrm{v}_y)$ relative to the unperturbed Keplerian rotation velocity

$\mathbf{u_0} = (0, -q\Omega x_p)$ in the local frame. These are evolved as

$$\frac{\mathrm{d}\mathbf{x}}{\mathrm{d}t} = \mathbf{v} - q\Omega x_p \hat{\mathbf{y}} \tag{3.13}$$

$$\frac{\mathrm{d}\mathbf{v}}{\mathrm{d}t} = -2\Omega\hat{\mathbf{z}} \times \mathbf{v} + q\Omega \mathrm{v}_x \hat{\mathbf{y}} + \frac{1}{\tau_f}(\mathbf{u} - \mathbf{v}), \tag{3.14}$$

where τ_f is the friction time of the particle (Johansen et al., 2006). The first two terms in equation 3.14 represent the Coriolis Force and the non-inertial force due to shear. The final term describes the drag force exerted by the gas on the particles which arises from the velocity difference between the two. Unlike the gas the particles do not feel the pressure force. The goal of this Chapter is to investigate where, in a typical self-gravitating disc, the solid particles are most strongly influenced by the self-gravitating structures in the gas disc. Additionally, we wish to investigate what range of particle sizes are most strongly affected, without making any assumption as to how particle sizes and masses are distributed. Consequently, we use massless 'test' particles. Therefore, there is no term modelling the back-reaction of the drag force in equation 3.8, nor is the self-gravity of the system considered in equation 3.14. We do acknowledge, however, that if the local solid density became comparable to that of the gas, these terms would become important.

The drag force on the particles from the gas is calculated by interpolating the gas velocity field to the position of the particle, using the second order spline interpolation outlined in Appendix A of Youdin & Johansen (2007).

3.2.6 Units and Initial Conditions

We normalise our parameters by setting $c_{s,0} = \Omega = \Sigma_0 = 1$. The time and velocity units are $[t] = \Omega^{-1}$ and $[v] = c_{s,0}$, resulting in the orbital period, $T = 2\pi$. The unit of length is the scale height, $[l] = H = c_{s,0}/\Omega$. We initialise the Toomre-Q parameter to be 1 throughout the sheet. This sets the gravitational constant $G = \pi^{-1}$. The surface density of gas is initially set to be unity everywhere in the sheet. The box is of length $L = 80G\Sigma/\Omega^2$ and is divided into a grid of 1024^2

cells. This choice of units sets the sheet length $L = 80H/\pi \sim 25H$. This is a much larger value for L than that typically taken for simulations investigating MRI driven turbulence (e.g. Johansen et al. (2006, 2011)), however is typical for those investigating instabilities due to self-gravity. (Gammie, 2001) estimates that structure in self-gravitating discs typically arises on length scales of $\sim 64G\Sigma/\Omega^2$. Typical proto-planetary discs are estimated to have aspect ratios $H/r = 0.05-0.1$ (Gammie, 2001; Armitage, 2011). This is supported by observations by Andrews et al. (2010), who find that typical discs have scale heights ranging from 2-20AU at radii of 100AU, giving aspect ratios ranging from 0.02 to 0.2. A shearing sheet centred at $r_0 = 20$AU with a scale height of ~ 1AU will therefore span the radial range $\sim 10 - 30$AU. It is worth noting that the cooling time, t_c, which we have assumed to be constant throughout the sheet, in reality is $t_c = t_c(\Sigma, U, \Omega)$ as described by Gammie (2001). However the use of constant cooling time over a sheet of this size allows us to infer the general behaviour of the dust particles at a given location within the disc.

The gas velocity field is initially perturbed by some small random fluctuations with the rms amplitude $\sqrt{<\delta\mathbf{v}^2>} = 10^{-3}$. We take the viscosity and diffusion coefficients to be $\nu = 10^{-2}$ and $\nu_{sh} = D_{sh} = 5.0$. We use 5×10^5 particles, split evenly between five friction times, $\tau_f = [0.01, 0.1, 1, 10, 100]\Omega^{-1}$. Bai & Stone (2010) and Laibe et al. (2012) have shown there is a spatial resolution criteria which applies to coupled dust and gas simulations such as those outlined above. For the dust particles to be properly resolved, the grid spacing must satisfy $\Delta x < c_s\tau_f$. For the chosen set of parameters we have $\Delta x/c_s \sim 0.07$, they satisfying this condition for all but the $\tau_f = 0.01\Omega^{-1}$ particles. The required increase in resolution to satisfy this for the $\tau_f = 0.01\Omega^{-1}$ particles is beyond our computational limits. The effects of these particles potentially being under-resolved are discussed in Section 3. Each particle species with a fixed radius is initially given zero velocity relative to the Keplerian flow and is distributed spatially uniformly throughout the sheet.

3.3 Results

3.3.1 Gas Evolution

The evolution of the gaseous component of the disc is in good agreement with that observed in analogous studies based on the shearing sheet formalism (Gammie, 2001; Johnson & Gammie, 2003; Mamatsashvili & Rice, 2009). The small initial velocity fluctuations grow and develop into nonlinear fluctuations in velocity, surface density and potential. Shocks then develop which proceed to heat the gas, while the cooling works to reduce the entropy of the gas. Density structures develop which are sheared out by differential rotation. These density structures tend to take on a trailing nature, which leads to a finite shear stress parameter α (Gammie, 2001). After a few orbits, the heating due to shocks is balanced by the cooling term and the thermal energy of the sheet settles into a quasi-steady self-regulated state, where the thermal, kinetic and gravitational energies of the disc are approximately constant with time. In this state, on the surface density field we clearly see elongated trailing surface density features, or density waves (Figure 3.1), whose particle trapping capability is our main subject of study.

The magnitude of these nonlinear density enhancements is determined by the cooling time - the smaller the cooling time, the larger the amplitude of density waves (Cossins et al., 2009; Rice et al., 2011). To analyse the efficiency of particle trapping by density wave structures at a range of radii within the disc, we consider several values of $t_c = 10, 20, 40, 80$ and $160\Omega^{-1}$, bearing in mind that in discs realistic (radiative) effective cooling timescales tend to decrease with increasing radius (Clarke, 2009; Rice & Armitage, 2009).

3.3.2 Particle Concentration

Once the gas has settled into a quasi-steady state, we release the dust particles. For the $t_c = 10\Omega^{-1}$ and $20\Omega^{-1}$ runs, the particles are introduced at a time $t_{par} = 10T$, while for the $t_c = 40\Omega^{-1}$, $80\Omega^{-1}$ and $160\Omega^{-1}$ runs at $t_{par} = 20T$, $t_{par} = 30T$, and $t_{par} = 50T$ respectively. In each case we evolve the system for a further 30

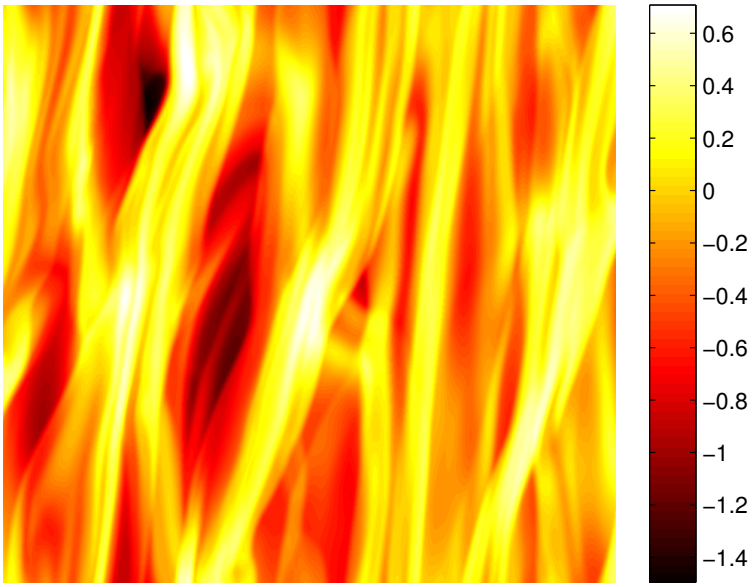

Figure 3.1 *Logarithmic surface density of the gas after 40 orbits in the* $t_c = 10\Omega^{-1}$ *run. At this stage the disc is already in a quasi-steady state.*

orbits, until the particles have also reached a quasi-steady state and come in sort of dynamical equilibrium with the gas - the majority of particles are trapped in density wave features, but particles aggregated within each density enhancement disperse as the the latter gets sheared out by the disc's differential rotation. These particles are then captured in a new density structure.

Upon release, the particles are drawn to local pressure maxima associated with the density waves in the gas. Figure 3.2 shows the logarithmic surface densities of the dust grains with different friction times in a quasi-steady state at $t = 40T$ in the $t_c = 10\Omega^{-1}$ run. The corresponding gas surface density at the same time is plotted in Figure 3.1. Comparing Figures 3.1 and 3.2, we see a clear correlation between the density enhancements in the gas and over-densities in the particles.

The degree to which the presence of spiral density waves affect the particle dynamics and the magnitude of their concentration depends on the friction time of the particles, as evident from Figures 3.2 and 3.3. The first three panels in Figure 3.2 show the surface densities of the smaller particles with correspondingly smaller friction times ($\tau_f = [0.01, 0.1, 1.0]\Omega^{-1}$ respectively). In this case, there is a high

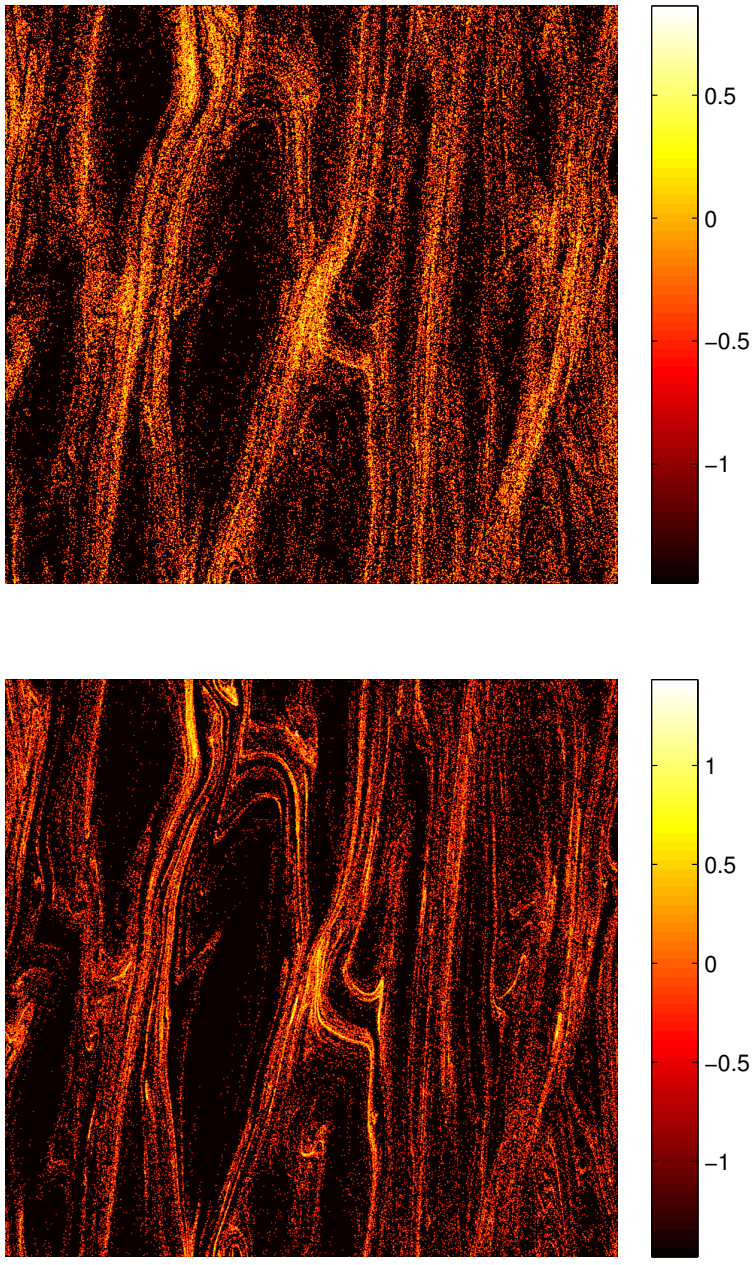

Figure 3.2 *Logarithmic surface density of the $\tau_f = 0.01\Omega^{-1}$ and $\tau_f = 0.1\Omega^{-1}$ particles for the $t_c = 10\Omega^{-1}$ run at $t = 40T$, when the disc is already in a quasi-steady state.*

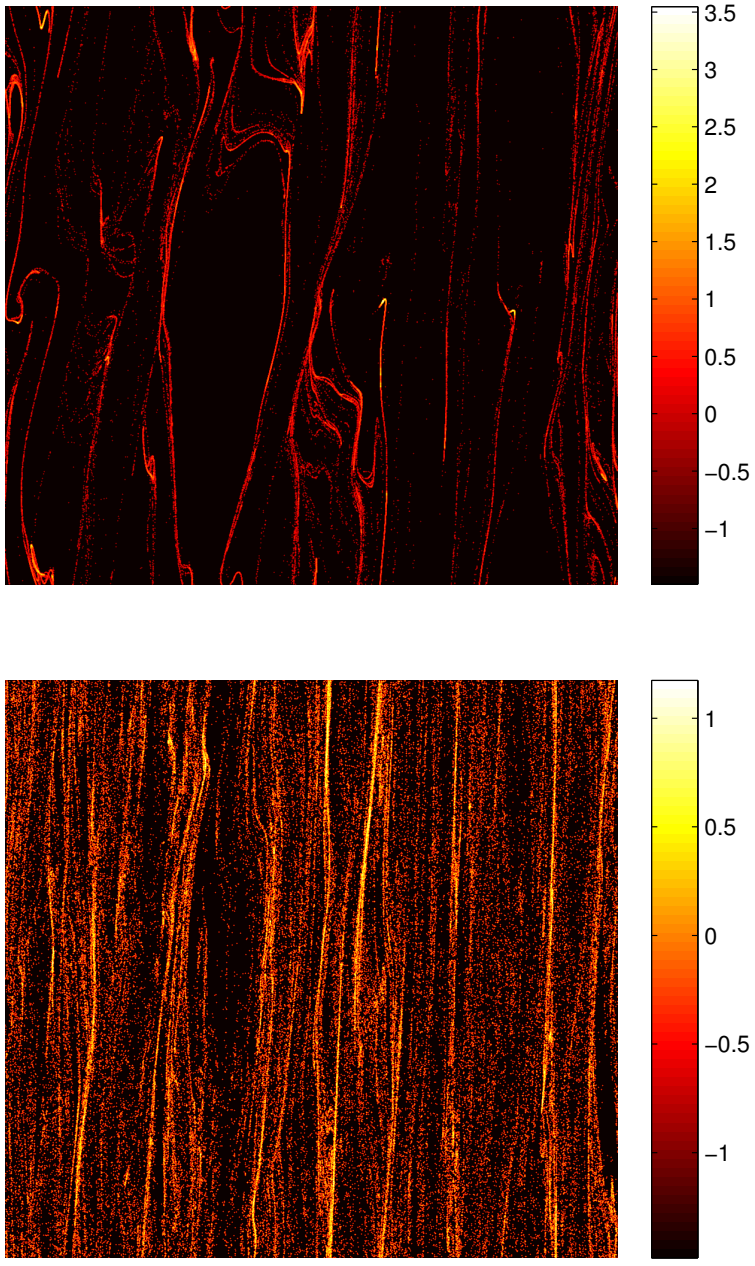

Figure 3.2 **(Continued)** *Logarithmic surface density of the* $\tau_f = 1.0\Omega^{-1}$ *and* $\tau_f = 10.0\Omega^{-1}$ *particles for the* $t_c = 10\Omega^{-1}$ *run at* $t = 40T$*, when the disc is already in a quasi-steady state.*

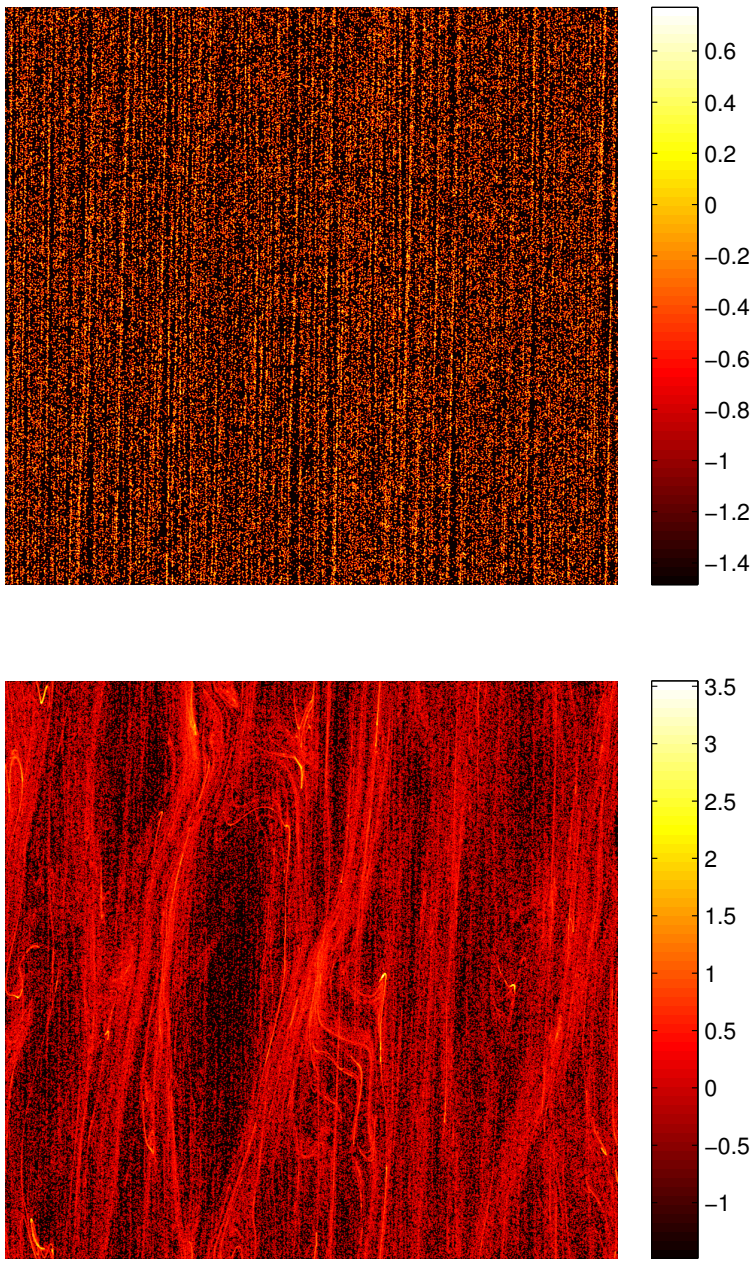

Figure 3.2 **(Continued)** *Logarithmic surface density of the* $\tau_f = 100.0\Omega^{-1}$ *particles and the combined particle surface density for the* $t_c = 10\Omega^{-1}$ *run at* $t = 40T$*, when the disc is already in a quasi-steady state, or 30 after the drag force between the gas and particles has been turned on. The surface density of gas at this time is shown in Figure 1. From these panels we see that intermediate-sized particles with* $\tau_f \sim 1.0\Omega^{-1}$ *are captured most effectively in density structures.*

degree of correlation between the structures in the gas surface density and the arrangement of the particles, with the smallest particles (with $\tau_f \leq 0.1\Omega^{-1}$, first two panels) tightly mapping the overall gas structure but the local enhancements of particle density are not exceptionally large, with typical density enhancements of no more than 10 times the mean particle density. The intermediate-sized particles (with $\tau_f = 1.0\Omega^{-1}$, third panel) are primarily concentrated at the crests of spiral waves, tracing out the locations of the pressure maxima and reaching there the largest values of density, up to a factor of $\sim 10^3$ times the mean particle density. By contrast, there is much less correlation between the surface densities of the gas and the larger particles (with $\tau_f \geqslant 1.0\Omega^{-1}$, 4th & 5th panels) and therefore the particle over-densities are also lower. In the latter case, the mean Keplerian motion of the particles tends to dominate over the action of the drag force, reducing the effect of the latter to a small perturbation of the background motion. The specific behaviour of particles with various friction times (sizes) in the density field of spiral waves found here agrees well with that in global disc simulations of particle dynamics by Rice et al. (2004). In this connection, we would like to mention that a similar high degree of concentration of intermediate-sized ($\sim$ 1m and $\tau_f \sim 1.0\Omega^{-1}$) dust particles also occurs in gas over-densities produced by MRI-driven turbulence in discs (Johansen et al., 2006, 2007).

Thus accumulation of the particles within spiral waves leads to an enhancement in the local surface density of the solids within the disc. Figure 3.3 shows how the maximum value of particle density, relative to the mean particle density, inside the domain varies with time for a range of particle sizes (friction times) in the $t_c = 10\Omega^{-1}$ simulation. Particles with very short ($\tau_f \leqslant 0.1\Omega^{-1}$) and very long ($\tau_f \geqslant 10\Omega^{-1}$) friction times exhibit small density enhancements, with the maximum density of particles typically no more than a few times the mean (initial) density. However, particles that occupy an intermediate size range with $\tau_f = 0.1 - 10\Omega^{-1}$ exhibit orders of magnitude larger growth in gas over-densities. For example, particles with $\tau_f = 0.1\Omega^{-1}$ and $\tau_f = 10\Omega^{-1}$ experience an increase in concentration approximately 10 times larger than that of particles in the above mentioned first two size ranges and around 20-30 times that of the initial particle density throughout the sheet. As mentioned above, particles characterised by $\tau_f = 1.0\Omega^{-1}$ are remarkable as they exhibit the highest degree of concentration in density wave crests/maxima, with the local density of the particles typically

reaching levels a factor of $\sim 10^2$ times that of the mean value, or initial particle density. This range of particle density enhancements is in good agreement with analytic theory, which predicts that the effects of the aerodynamic drag force are most significant for $\tau_f = 1.0\Omega^{-1}$ particles. This consistency with analytic theory is reassuring when considering the potential non-convergence issue with the smallest ($\tau_f = 0.01\Omega^{-1}$) particles, as combined with the lack of obvious numerical problems in Figure 3.2, suggest that our results are correct to a good degree of accuracy, even for the insufficiently resolved particles.

In this work we have used massless 'test' particles so as to focus mainly on where the self-gravitating structures in the gas disc can have the most significant affect on the solid particles. In a typical star forming cloud, the solid particles make up ~ 1 % of the mass. This can, however, be distributed over a wide range of particle sizes and so it is not clear how much mass will be in particles that are strongly influenced by the gas overdensities (i.e., in particles with friction times $0.1\Omega^{-1} < \tau_f < 10\Omega^{-1}$). Given that the density of these particles can be enhanced by a factor of $100 - 1000$, if ~ 10 % of the solid particle mass is in this size range, there will be regions in the disc where the gas and solid densities are comparable and we would then need to include the back reaction of the solid particles on the gas and also the self-gravity of the solid particles to determine their subsequent evolution.

The enhancement in the local density of solids is also dependent on the gas cooling time, t_c. As outlined in Section 3.3.1, the amplitude of spiral wave structure is determined by the value of cooling time, with smaller cooling times resulting in larger pressure gradients and higher surface densities in the spiral waves. The higher pressure gradients due to short cooling times tend to be more efficient at trapping the particles. Figure 3.4 shows the maximum of net surface density of all particles over time for a range of cooling times. Although in this plot we show the net particle density, at any given value of cooling time the maximum value of density is still due to the particles with $\tau_f = 1.0\Omega^{-1}$, similar to the above situation with $t_c = 10\Omega^{-1}$. Here the amount of particle accumulation that occurs appears to have a dependance on t_c, with the longest values studied ($t_c = 80\Omega^{-1}$ and $t_c = 160\Omega^{-1}$) showing less concentration than that for the shorter cooling times. This decrease is due to the shallower gradients in both

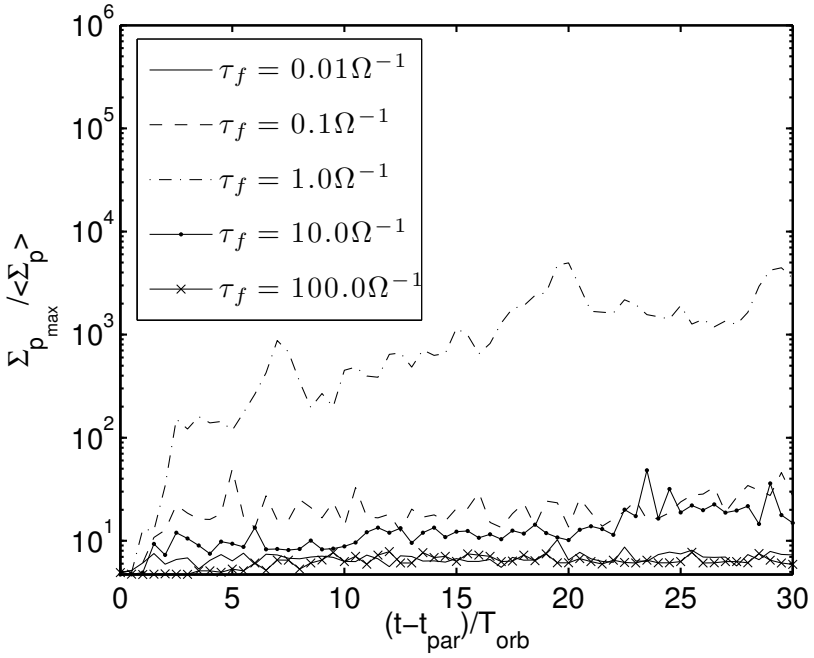

Figure 3.3 *Maximum particle density, relative to the mean, as a function of time for a range of friction times in the $t_c = 10\Omega^{-1}$ simulation. Particles with $\tau_f = 1.0\Omega^{-1}$ exhibit the highest degree of concentration in gas over-densities.*

pressure and potential associated with the longer cooling times. Although longer cooling times are not considered here, we expect this trend to continue, with longer cooling times exhibiting less concentration. The particles also reach a quasi-steady state much quicker in the simulations with a shorter cooling time. As the cooling time gets longer, the particles tend to form long filaments of approximately uniform density along the spiral waves in the gas, rather than tightly crowding in density wave crests.

It is instructive at this point to relate the parameters used in our simulations to realistic models of self-gravitating proto-planetary discs. By taking the analytically derived profile for the total stresses α from the appendix of Clarke (2009) and finding with it an effective cooling time using the expression given in Gammie (2001), we can estimate the range of radii in the disc corresponding to the effective cooling times considered here. Figure 3.5 shows how such obtained t_c varies with radius within the disc, for given stellar accretion rates $\dot{M}$. From Figure 3.5 we see that the range of cooling times considered here spans a radial

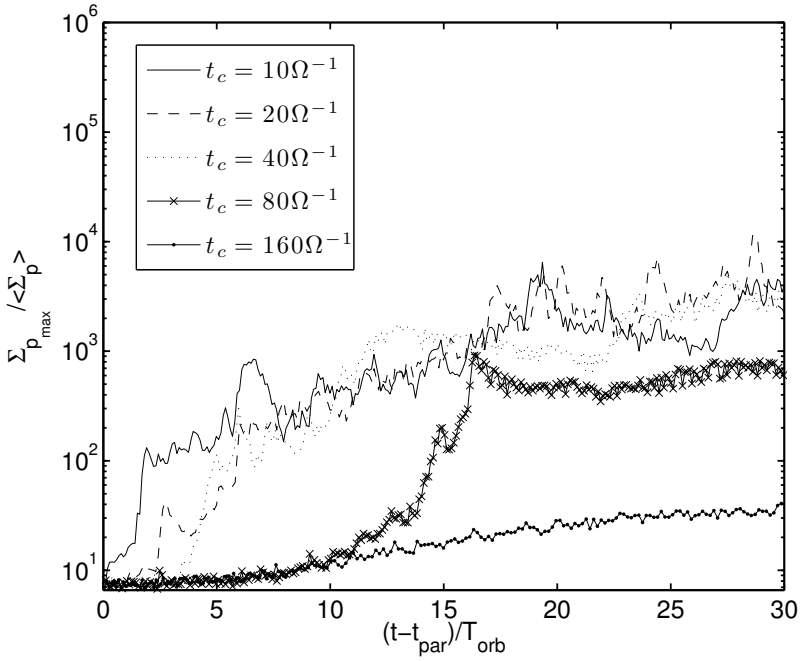

Figure 3.4 *Maximum particle density, relative to the mean, as a function of time for a range of cooling times. Particles are somewhat more effectively concentrated in spiral density waves at short cooling times, with the* $t_c = 80\Omega^{-1}$ *and the* $t_c = 160\Omega^{-1}$ *simulations showing a decrease in particle concentration than the shorter times considered.*

interval $20 - 60$AU in the disc. This is actually the range of radii at which disc self-gravity is appreciable ($Q \sim 1$) and maintains the disc in a quasi-steady state. At larger distances ($\geq$ 70AU) cooling is too fast, causing the disc to fragment, whereas at smaller distances ($\leq$ 10AU) cooling is very inefficient and so the self-gravitating density perturbations will be negligible and this region is likely to be dominated by the magneto-rotational instability (Balbus & Hawley, 1991; Zhu et al., 2009). Once a radius within the disc is specified, we can also determine the actual values of physical variables (gas density, sound speed, etc.) in our simulations and relate the dimensionless friction times of particles used here to their real physical sizes.

The force acting on a dust particle of radius a traveling at a velocity $\mathbf{u}$ relative to the surrounding gas of density ρ is given by (Whipple, 1972; Weidenschilling,

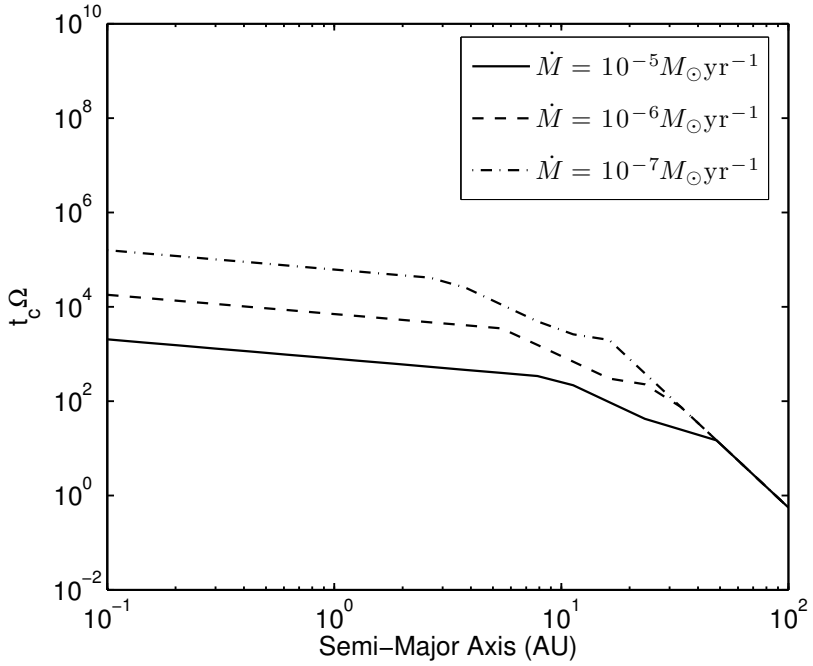

Figure 3.5 *Analytically derived profile for t_c as a function of radius for different mass accretion rates. The effective cooling times we consider here correspond to the radial range $\sim 20 - 60$AU.*

1977),

$$\mathbf{F_D} = -\frac{1}{2} C_D \pi a^2 \rho u^2 \hat{\mathbf{u}}, \tag{3.15}$$

where $u = |\mathbf{u}|, \hat{\mathbf{u}} = \mathbf{u}/u$ and the drag coefficient C_D is defined as,

$$C_D = \begin{cases} \frac{8}{3}\frac{c_s}{u} & a < \frac{9\lambda}{4} \\ 24 R_e^{-1} & R_e < 1 \\ 24 R_e^{-0.6} & 1 < R_e < 800 \\ 0.44 & R_e > 800. \end{cases} \tag{3.16}$$

The drag regime with $a < 9\lambda/4$ is generally called the Epstein regime, whereas the other three regimes define the Stokes drag. In expressions 3.16, R_e is the Reynolds number characterizing gas flow in the vicinity of a dust particle, which will be defined below, and λ is the mean free path of gas molecules. Assuming the gas to be made mainly of molecular hydrogen, for the mean free path we get

$$\lambda = \frac{m_{H_2}}{\rho A} = \frac{4 \times 10^{-9}}{\rho} \text{cm}. \tag{3.17}$$

The Reynolds number is given by,

$$R_e = \frac{2\rho a u}{\eta} \tag{3.18}$$

where $\eta = \rho\nu$ is the gas viscosity. For collisional viscosity, we have

$$\eta = \frac{\rho c_s \lambda}{2}. \tag{3.19}$$

The Reynolds number can therefore be expressed as

$$R_e = 4 \left(\frac{a}{\lambda}\right) \left(\frac{u}{c_s}\right). \tag{3.20}$$

Once the drag force on the particles is known, the corresponding friction time of

the particles (as used in equation 4.8) can be calculated,

$$\tau_f = \frac{m_p u}{|\mathbf{F_D}|}, \tag{3.21}$$

where $m_p = \frac{4}{3}\pi a^3 \rho_p$ is the mass of a particle of internal density ρ_p.

By following this prescription, we estimate that for a disc with the surface density profiles derived in Clarke (2009), at the innermost radius considered ($\sim$ 20AU), the range of particle sizes considered spans 1mm-10m, with the $\tau_f = 1$ particles corresponding to objects with a physical size of 10cm. At an outer radii of $\sim$ 60AU, the size range considered is halved, spanning 0.3mm-3m, with $\tau_f = 1$ particles corresponding to 3cm size objects. We note here that the inner radii tend to be more effective at collecting 'larger' particles, this allows for the possibility of small objects forming at large radii and growing as they drift inward due to aerodynamic drag.

3.3.3 Particle Velocities

Although large concentrations of dust and ice is vital for the growth of planetesimals, the velocities of the particles must also be considered in order to determine the evolution of the solid component of the disc. If the relative velocities of the particles are too large, collisions become too energetic, and tend to result in large objects being broken apart, rather than growing. Figure 3.6 shows the distribution of velocities for each particle size at the end of the $t_c = 10\Omega^{-1}$ simulation. The peak of the distribution lies at higher velocities for smaller grain sizes, whilst the width of the distribution tends to also increase. In the case of the $\tau_f = 1.0\Omega^{-1}$ particles, the width of the distribution is unusually narrow. This appears to be a result of the particles being tightly concentrated at the centre of density waves, causing their velocities to become highly ordered, resulting in the majority of particles having similar velocities. This keeps the relative velocities between particles low, improving the likelihood of collisional growth occurring.

By contrast, particles with small $\tau_f \leqslant 1.0\Omega^{-1}$ are strongly coupled to the gas and practically repeat the overall turbulent motion of gas outside spiral arms,

hence the larger dispersion in the particle velocity. On the other hand, particles with large $\tau_f \geqslant 10.0\Omega^{-1}$ are very loosely coupled to the gas and therefore most of them have small velocity dispersion, i.e., they are not effectively accelerated by gas. In Figure 3.6, this corresponds to the large peak in particle number near zero velocity for large friction times.

As we move radially inward within the disc, we see the velocity dispersion for each particle size narrows as the cooling time increases. Figure 3.7 shows the velocity dispersion of the $\tau_f = 1.0\Omega^{-1}$ particles for a range of cooling times. The peak velocity decreases with increasing cooling time, and the width of the distribution narrows. We therefore see that despite the reduction in the concentration of solids that arises from the increasing cooling time, the likelihood of constructive collisions increases due to the decreasing velocity dispersion.

As shown in Figures 3.6 and 3.7, the velocities of particles within our simulation domain are typically of order the local sound speed in the disc. For typical disc parameters, this ranges from $100 - 1000\text{ms}^{-1}$. Such high velocities are typically associated with destructive collisions between particles (grain destruction is typically estimated to occur for collisions above $\sim 10\text{ms}^{-1}$). This is likely offset due to the presence of the spiral density waves. As the velocities of particles located within the spiral density waves is determined by the aerodynamic drag force between the dust particles in the gas, the particle velocities tend become aligned along spiral waves, and the relative velocities between particles are likely to be much smaller, as demonstrated by the small spread of velocities in Figures 3.6 and 3.7, especially in the simulations with longer values of t_c. In order to obtain more precise values for the relative (collisional) velocities, a more complete description of the particles evolution, including the back-reaction and self-gravity is required.

This opens up the possibility of a preferred region for planetesimal formation at radii between 30-40AU, where the cooling time is low enough to allow large concentrations of solids to accumulate, without the collisional velocities of particles becoming high enough to inhibit growth.

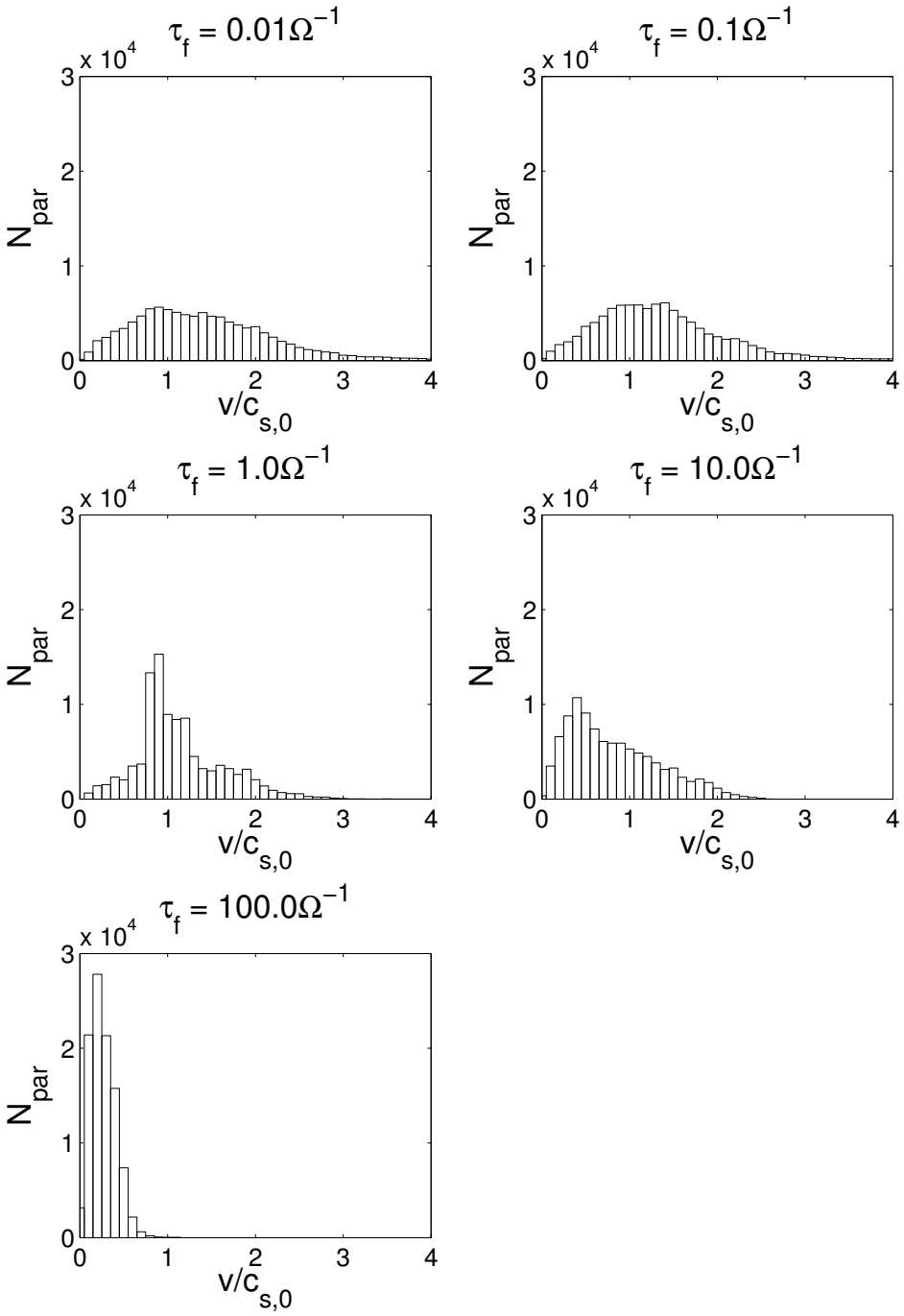

Figure 3.6 *Histograms showing the spread of particle velocities, relative to the initial sound speed, for each friction time at the end of the* $t_c = 10$ *simulation. As the friction time lengthens, the distribution of velocities narrows due to the diminishing effect of the drag force. The peak of the distribution also tends to occur at lower velocities.*

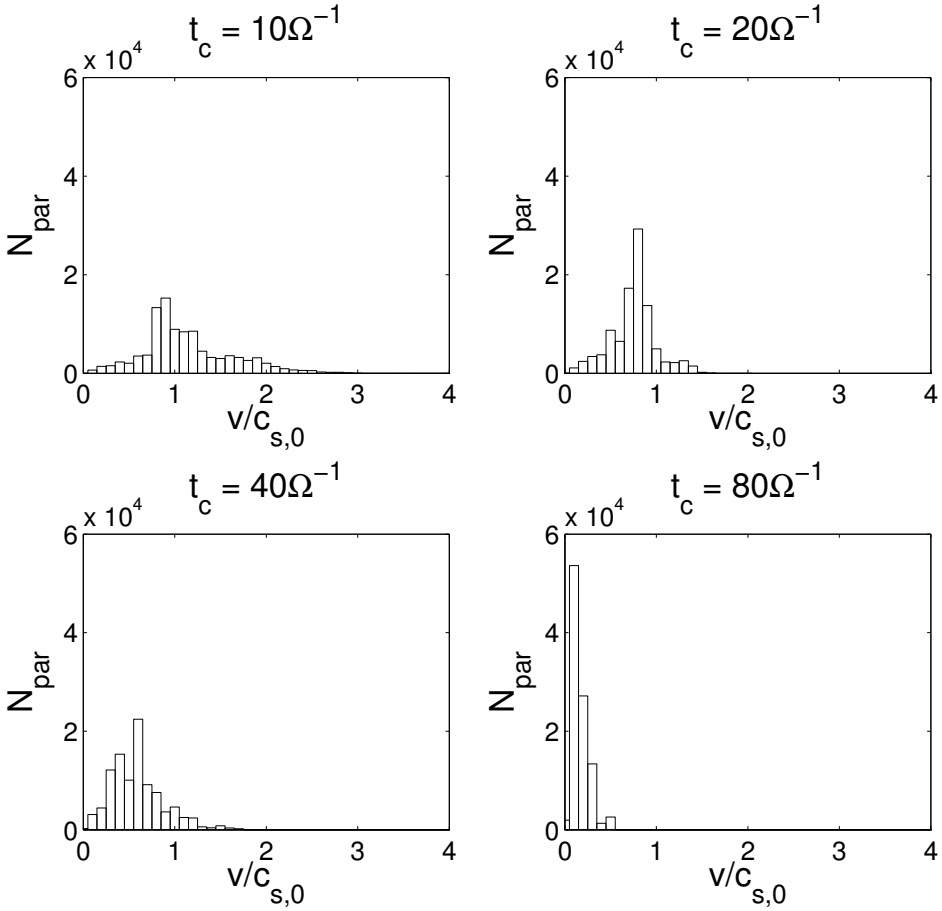

Figure 3.7 *Histograms showing the spread of the $\tau_f = 1$ particles velocities, relative to the initial sound speed, at the end of our simulations for the four shortest cooling times considered. As the cooling time lengthens, the distribution of particle velocities narrows, with the peak of the distribution occurring at smaller velocities.*

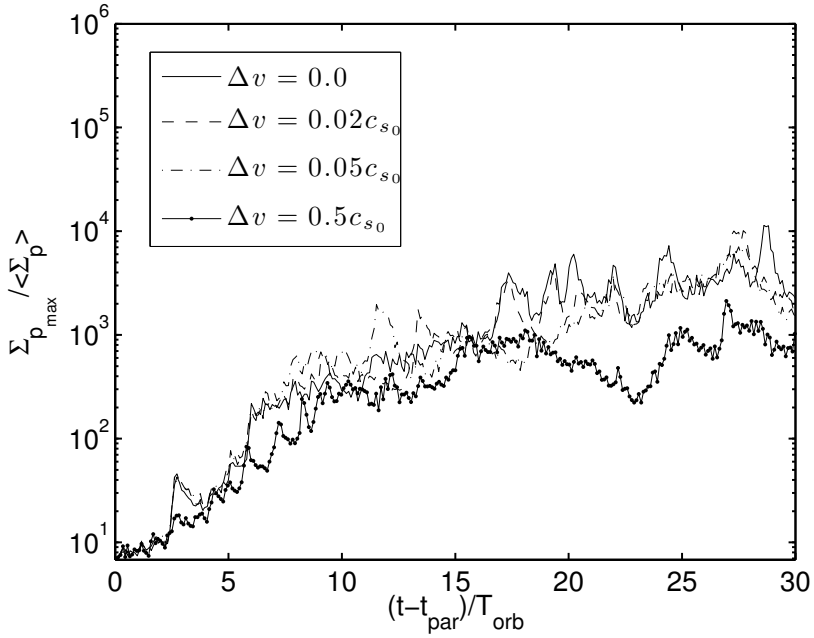

Figure 3.8 *Maximum particle density, relative to the mean, against time for a range of drift values, $\Delta v = 0.0, 0.02, 0.05$ and 0.5 for cooling time $t_c = 20\Omega^{-1}$. Even in the presence large amounts of radial drift, there are still significant over-densities in the particle density field due to the gravitational instabilities.*

3.3.4 Effects of Radial Drift

The above simulations were all conducted assuming that there is no radial pressure gradient supporting the disc ($\Delta v = 0$ in Equation 3.8). In reality the gas in the disc is partially supported by pressure, causing it to orbit at slightly sub-Keplerian velocities. The dust particles however travel with approximately Keplerian velocities. The resulting velocity difference results in the particles transferring angular momentum to the disc and spiralling inwards towards the star. This radial pressure gradient could potentially negate the effect of the spiral density waves, causing particles to drift through the associated pressure maxima, reducing the degree to which particles are concentrated. In order to quantify the effect of this radial drift we performed several simulations at a fixed cooling time t_c, varying only the value of the drift parameter Δv. Figure 3.8 shows how the maximum surface density of particles evolves with time for each value of Δv considered. In each case, we see that for typical values of Δv (of order

a few percent of the sound speed), there is very little deviation from the case with no radial drift. Even for very high drift values associated with turbulent discs, the overall concentration of particles is reduced only slightly, suggesting that the radial pressure gradient does little to change the efficiency of particle concentration within spiral waves.

3.4 Discussion and Conclusions

In this Chapter we present a series of simulations modelling dust dynamics in self-gravitating discs using the shearing sheet approximation. The dust particles evolve within a quasi-steady gaseous spiral structure produced by a combined effect of disc self-gravity and cooling. Particles are coupled to the gas via a drag force with a constant friction time. As in previous related studies (Rice et al., 2004, 2006), we find that spiral density waves in self-gravitating discs can result in significant over-densities in the solid component of the disc. A novel contribution of this work is, however, that we characterised a particle trapping capability of density waves for a wide range of disc cooling times and particle friction times. Particles with friction times $\tau_f \sim 1.0\Omega^{-1}$ tend to be affected by spiral density waves most effectively and exhibit the largest and the tightest concentrations in wave crests. At smaller friction times, the particles closely trace the overall gaseous spiral structure, however exhibit lesser concentration in wave crests. At larger friction times, particles are almost unaffected and decouple from the gas, so that they mimic the spiral structure very weakly again with smaller concentration in spiral waves. We also found that particle concentration depends on cooling time (see Figure 3.4). The shorter cooling times ($t_c \leq 40\Omega^{-1}$) considered show similar amounts of particle concentration, as the spiral density waves are large enough to continually trap the majority of the particles. For longer cooling times this is no longer the case, as seen in the $t_c = 80\Omega^{-1}$ and the $t_c = 160\Omega^{-1}$ run, where the maximum particle density is lower. We expect this trend to continue to longer cooling times and given the rapid increase in t_c with decreasing radius (Figure 3.5), do not expect disc self-gravity to play a significant role in particle dynamics at inner radii ($r < 20$AU).

This implies that particle trapping by density waves is not necessarily restricted to the very outer regions of the disc, a concern raised by Clarke & Lodato (2009). Generally, as mentioned above, grains with effective friction time $\tau_f \sim 1.0\Omega^{-1}$ exhibit the largest concentration in density waves. When this is translated in terms of particle size we find that grain sizes which experience the largest density enhancements depend on the radius in the disc, with larger particles more efficiently trapped at inner radii and smaller at outer radii. We also analysed the dependence of particle velocity dispersion on friction and cooling times. Given a fixed cooling time, the smaller the friction time, the larger the average velocity of particles. Conversely, at a fixed friction time, the larger the cooling time, the smaller the particle velocities are.

Based on the trends observed in this Chapter, we propose the following potential route of grain growth and evolution in discs: As smaller grains can be trapped primarily at larger radii, this can lead to continual growth as grains secularly migrate inward as a result of drag forces from the gas (due to difference between Keplerian velocity of particles and sub-Keplerian velocity of gas). Small grains initially at large radii ($\geqslant$ 60AU) can become trapped in gas over-densities and grow through collisions with other particles. This process can continue until the grains reach sizes larger than the optimally trapped size range ($\tau_f \sim 1.0\Omega^{-1}$). Then a gas over-density can no longer prevent particles from radial drift and they start to slowly move inward in the next optimally trapped size range at smaller radii, where they will undergo further rapid growth and so on until they reach planetesimal sizes. However, this process may be partially offset at large radii, where the effective cooling time is lower, as the relative velocities between particles may be still large enough to lead to the collisional destruction of large objects. At inner radii ($\simeq 20 - 30$AU) the velocity dispersion is much lower, especially for the $\tau_f = 1.0\Omega^{-1}$ particles which are clumped in spiral waves most effectively. This may lead to a ring of material, analogous to the Kuiper belt in our own Solar System, building up at intermediate radii within the disc, where the enhancement of the solids surface density is significantly augmented due to the self-gravitating structure, but the velocity dispersion is sufficiently small to avoid collisional destruction of growing objects.

Another interesting question that still needs to be addressed is the effect that large

accumulations of particles have on the gas dynamics due to the back reaction of the particles on gas and the effect of particle self-gravity. As we found here, particle densities in the crests of spiral waves can reach 100-1000 times the mean particle density. For typical proto-planetary discs, the dust to gas mass ratio is 0.01. If there is sufficient mass in the size range that is strongly influenced by structures in the gas discs, there will be regions where the particle density can reach values comparable to, or sometimes even larger than, the local gas density. Under these conditions, it is no longer appropriate to treat the particles as massless tracer particles. To obtain a more comprehensive understanding of the particles' evolution the back reaction of particles on gas and the self-gravity of dust particles must be included. For example, in the case of planetesimal formation as a result of streaming instability, ultimate concentration of particles in the nonlinear saturated state is determined by particle feedback on gas that limits explosive growth of particle density due to linear streaming instability once the local dust-to-gas ration becomes of order unity in gas over-densities (Johansen & Youdin, 2007). As regards the role of particle self-gravity, we saw that once the parent gas over-density has sheared out, particles aggregated within it also dissolve, whereas particle self-gravity can in principle keep dust clumps together and prevent them from dissolving, facilitating further bonding of grains. For example, in analogous simulations of particle accumulation but in gas over-densities in MRI-driven turbulence, ultimate sticking, retainment and growth of particle aggregates occurs in fact thanks to their self-gravity (Johansen et al., 2007). Finally, only the 2D 'shearing sheet' case has been considered in our analysis. Therefore we are unable to observe any behaviour in the z direction, such as dust settling. Further work must be done to expand the study to the 3D 'shearing box' case to study these effects.

Chapter 4

Planetesimal Formation in Spiral Density Waves

4.1 Introduction

The field of planet formation currently provides two methods through which large gas giant planets can form in discs around young stars. The favoured model of planet formation is known as the core accretion model. This model proposes that planets grow via a 'bottom-up' process, where a core of solid material grows from initially small, kilometre sized objects via a series of collisions. If this core becomes massive enough, it will begin to accrete a gaseous envelope from the disc (Pollack et al., 1996). For a Jupiter-like gas giant planet to form, the solid core must reach a mass of $\sim$ 10 Earth masses before the disc is depleted of gas, a process which is observationally estimated to take $\sim 10^7$ years (Haisch et al., 2001). A key uncertainty in the core accretion model is the mechanism through which the disc is populated with kilometre-sized solid objects, similar to those found in the asteroid belt. It is likely that these objects are assembled via collisional growth from initially small dust grain present in the ISM during the star formation process which creates the proto-planetary disc. However current theory has difficulties describing the growth of dust grains past the metre-scale. At this size, collisions between bodies are no longer expected to be constructive,

due to the velocities of the objects involved, and the self-gravity of the resulting rubble pile is thought to be insufficient to allow the debris to collapse into a gravitationally bound structure.

The dynamics of these smaller particles that ultimately grow to form these kilometre-sized planetesimals is largely governed by the aerodynamic drag force that arises from the velocity differential between the particles and the surrounding gas. Within a few scale heights of the disc mid-plane, the pressure gradient within the disc tends to be negative. This causes the gas to orbit with sub-Keplerian velocities. The dust is not affected by the gas pressure and orbits at Keplerian velocities. The drag force on the dust particles that arises from this velocity difference results in the solids losing angular momentum to the disc and drifting inward at a rate that depends on the particles' size (Weidenschilling, 1977; Nakagawa et al., 1986). For very small grain sizes, the dust is tightly coupled to the gas in the disc and the radial drift velocities are small. For very large objects, the solids are decoupled from the gas, move in approximately Keplerian orbits and again have very small drift velocities. Particles in the intermediate size range can, however, have large drift velocities. Although the exact size range depends on the local properties of the disc, drift velocities can exceed 10^3cm/s for objects with sizes between 1cm and 1m (Weidenschilling, 1977). Therefore the process through which planetesimals form must be rapid, unless this inward drift can be offset. Laibe et al. (2012) have shown that there may be surface density and temperature profiles for which particles may survive this inward migration, and Gibbons et al. (2012) have shown that local pressure maxima associated with density waves which arise due to gravitational instabilities in the disc can shield the particles from the inward drift. Nevertheless, in the standard core accretion scenario, the period of growth from micron to decametre sized objects is expected to be rapid, else objects in this size range will rapidly spiral inward and be accreted onto the central proto-star.

Gravitational instabilities such as those mentioned above arise, in a razor–thin disc, when the sound speed c_s, Keplerian rotation frequency, Ω and the surface density of the disc satisfy (Toomre, 1964),

$$Q \equiv \frac{c_s \Omega}{\pi G \Sigma} < 1. \tag{4.1}$$

This requires that the disc be relatively massive compared to its parent star, and this criteria is often re-expressed as a ratio of disc mass to stellar mass,

$$\frac{M_{disc}}{M_*} > \frac{h}{r}, \tag{4.2}$$

where h/r is known as the aspect ratio of the disc, and is typically around 0.05 - 0.1 for most protoplanetary discs (Gammie, 2001; Armitage, 2011). If a disc is susceptible to such instabilities, one of two outcomes may occur, depending on the thermal properties of the disc. If the cooling time is greater than some threshold the disc will settle into a quasi-steady state, where the cooling balances the heating generated by gravitoturbulence (Gammie, 2001). For cooling times shorter than $t_{c,crit}$, the disc may fragment, forming brown dwarf and/or gas giant planet type objects (Boss, 1998). The critical cooling time below which fragmentation occurs is commonly taken to be $t_{c,crit} = 3\Omega^{-1}$ (Gammie, 2001; Rice et al., 2003) however recent studies suggest that this threshold may not be fully converged, with some simulations suggesting critical cooling times as high as $t_c = 20\Omega^{-1}$. Although very few Class II objects are observed to have sufficiently massive discs for gravitational instabilities to set in (Beckwith & Sargent, 1991), observations indicate that during the Class 0 and Class I phases, massive discs may be much more common around protostars (Rodriguez et al., 2005; Eisner et al., 205; Greaves & Rice, 2010), suggesting that most, if not all stars possess a self-gravitating disc for some period of time during the early star formation process. If this is the case, these instabilities likely take the form of non-axisymmetric spiral structures.

It has been shown that these spiral waves are highly effective at trapping the solids in the disc. Rice et al. (2004) showed, using global simulations, that the surface density of certain particle sizes can be enhanced by a factor of over 100 in the spiral wave structure. Gibbons et al. (2012) used local shearing-sheet simulations to expand on these findings, mimicking the conditions at a range of disc radii to study the particle trapping capabilities of spiral density waves through the disc. These results showed that gravitational instabilities are responsible for creating large over-densities in the solid component of the disc at intermediate to large orbital radii within the disc (> 20AU). Rice et al. (2006) estimated from global simulations that the observed increase in the surface density of solids will lead

to the creation of km-scale planetesimals due to the gravitational collapse of the solids in the over-dense regions. Here we aim to directly study the gravitational collapse of the solids via local shearing-sheet simulations.

The goal of the work presented here is to demonstrate how the over-densities that can form in the solid component of the disc can undergo gravitational collapse as a result of the solids self-gravity, promoting further grain growth, which can lead to the formation of planetesimals at very early evolutionary stages when the disc is still self-gravitating. This directly expands on the work done by Gibbons et al. (2012), which studied the effect that changing the effective cooling time of the gas has on the particle-trapping properties of spiral density waves for a range of particles sizes (stopping times). In the following work, we study the dynamical behaviour of particles embedded in a self-gravitating disc using a local shearing-sheet approximation. We study, via numerical simulations, the ability of density enhancements to collapse via their self-gravity, and the resulting behaviour of the solid component of the disc.

This Chapter is arranged as follows. In Section 2 we outline the adjustments made to the model used in our simulations. In Section 3 we discuss the evolution of the gas and dust particles. Finally, we draw our conclusions in Section 4.

4.2 Model

To investigate the dynamics of solid particles embedded in self-gravitating proto-planetary discs, we solve the 2D local shearing sheet equations for gas on a fixed grid, including disc self-gravity as in Gammie (2001), together with the equations of motion of solids coupled to the gas solely through aerodynamic drag force. As a main numerical tool, we employ the PENCIL CODE. The PENCIL CODE is a sixth order spatial and third order temporal finite difference code (see Brandenburg (2003) for full details). The PENCIL CODE treats solids as numerical super-particles (Johansen et al., 2006).

To use the local shearing sheet model, we must make two simplifying assumptions,

first that the disc is cool, and therefore thin ($H/r \simeq c_s/(\Omega r) \ll 0.1$), and that the disc is razor-thin, as in Gammie (2001). In the shearing sheet approximation, disc dynamics is modelled in the local Cartesian coordinate frame centred at some arbitrary radius, r_0, from the central object and rotating with the disc's angular frequency, Ω, at this radius. In this local frame, the x-axis points radially away from the central object, the y-axis points in the azimuthal direction of the disc's differential rotation, which in turn manifests itself as an azimuthal parallel flow characterised by a linear shear, q, of background velocity, $\mathbf{u}_0 = (0, -q\Omega x)$. Our simulation domain spans the region $-L_x/2 \leq x \leq L_x/2$, $-L_y/2 \leq y \leq L_y/2$. We adopt the standard shearing-sheet boundary conditions (Hawley et al., 1995), namely for any variable f we have

$$f(x, y, t) = f(x, y + L, t) \tag{4.3}$$

$$f(x, y, t) = f(x + L, y - q\Omega L t, t). \tag{4.4}$$

These boundary conditions apply to all grid variables except the azimuthal component of the velocity, u_y, which must be adjusted to account for the relative shear between neighbouring boxes. The azimuthal velocity on the radial boundary is,

$$v_y(x, y, t) = v_y(x + L, y - q\Omega L t, t) + q\Omega L. \tag{4.5}$$

The shear parameter $q = 1.5$ for Keplerian rotation profile adopted in this paper.

The equations governing the evolution of the gas and particles remain as outlined in Chapter 3, with the following changes to account for the mass of the particles.

4.2.1 Gas Velocity

The equation of motion for the gas velocity $\mathbf{u}$ relative to the background Keplerian flow $\mathbf{u}_0$ takes the form

$$\frac{\partial \mathbf{u}}{\partial t} + (\mathbf{u}\cdot\nabla)\mathbf{u} - q\Omega x\frac{\partial \mathbf{u}}{\partial y} = -\frac{\nabla P}{\Sigma} - 2\Omega\hat{\mathbf{z}}\times\mathbf{u} + q\Omega u_x\hat{\mathbf{y}} + 2\Omega\Delta v\hat{\mathbf{x}} - \frac{\Sigma_p/\Sigma}{\tau_f}(\mathbf{u}-\mathbf{v}) - \nabla\psi + \mathbf{f}_\nu(\mathbf{u}), \tag{4.6}$$

where P is the two-dimensional pressure and ψ is the gravitational potential of the sheet due to the gas surface density perturbation $\Sigma - \Sigma_0$. The left hand side of Equation 4.6 includes terms from the velocity field $\mathbf{u}$ and the Keplerian flow. The first term on the right hand side of the equation is the force due to the pressure gradient. The second and third terms represent the Coriolis effect/shear induced by the choice of coordinate system. The fourth term mimics a global radial pressure gradient, which reduces the orbital speed of the gas by Δv and is responsible for the inward migration/drift of solids in an unperturbed disc. The main purpose for the inclusion of this term here is to see how the radial drift affects the concentration of particles by spiral density waves. The fifth term describes the drag force exerted on the gas by the dust particles. The sixth term represents the effect of the gravitational potential of the disc. Finally we include an explicit viscosity term, $\mathbf{f}_\nu$, which contains both Navier-Stokes viscosity and a bulk viscosity for resolving shocks.

4.2.2 Dust Particles

The dust particles are treated as a large number of numerical superparticles, with positions $\mathbf{x} = (x_p, y_p)$ on the grid and velocities $\mathbf{v} = (\mathrm{v}_x, \mathrm{v}_y)$ relative to the unperturbed Keplerian rotation velocity $\mathbf{u_0} = (0, -q\Omega x_p)$ in the local frame. These are evolved as

$$\frac{\mathrm{d}\mathbf{x}}{\mathrm{d}t} = \mathbf{v} - q\Omega x_p\hat{\mathbf{y}} \tag{4.7}$$

$$\frac{\mathrm{d}\mathbf{v}}{\mathrm{d}t} = -2\Omega\hat{\mathbf{z}}\times\mathbf{v} + q\Omega\mathrm{v}_x\hat{\mathbf{y}} + \nabla\psi_p + \frac{1}{\tau_f}(\mathbf{u}-\mathbf{v}), \tag{4.8}$$

where τ_f is the friction time of the particle (Johansen et al., 2006). The first two terms in equation 4.8 represent the Coriolis Force and the non-inertial force due to shear. The final term describes the drag force exerted by the gas on the

particles which arises from the velocity difference between the two. Unlike the gas the particles do not feel the pressure force, and the self-gravity of the particles is not studied here, therefore we omit the term describing the particles' collective gravitational potential. The drag force on the particles from the gas is calculated by interpolating the gas velocity field to the position of the particle, using the second order spline interpolation outlined in Appendix A of Youdin & Johansen (2007).

4.2.3 Units and Initial Conditions

We normalise our parameters by setting $c_{s,0} = \Omega = \Sigma_0 = 1$. The time and velocity units are $[t] = \Omega^{-1}$ and $[v] = c_{s,0}$, resulting in the orbital period, $T = 2\pi$. The unit of length is the scale height, $[l] = H = c_{s,0}/\Omega$. We initialise the Toomre-Q parameter to be 1 throughout the sheet. This sets the gravitational constant $G = \pi^{-1}$. The surface density of gas is initially set to be unity everywhere in the sheet. The box is of length $L = 80G\Sigma/\Omega^2$ and is divided into a grid of 1024^2 cells. This choice of units sets the sheet length $L = 80H/\pi \sim 25H$. It is worth noting that the cooling time, t_c, which we have assumed to be constant throughout the sheet, in reality is $t_c = t_c(\Sigma, U, \Omega)$ as described by Gammie (2001). However the use of constant cooling time over a sheet of this size allows us to infer the general behaviour of the dust particles at a given location within the disc.

The gas velocity field is initially perturbed by some small random fluctuations with the rms amplitude $\sqrt{< \delta \mathbf{v}^2 >} = 10^{-3}$. We take the viscosity and diffusion coefficients to be $\nu = 10^{-2}$ and $\nu_{sh} = D_{sh} = 5.0$. We use 5×10^5 particles, split evenly between five friction times, $\tau_f = [0.01, 0.1, 1, 10, 100]\Omega^{-1}$. As noted in Gibbons et al. (2012), Bai & Stone (2010) and Laibe et al. (2012) have shown there is a spatial resolution criteria which applies to coupled dust and gas simulations such as those outlined above. For the dust particles to be properly resolved, the grid spacing must satisfy $\Delta x < c_s \tau_f$. For the chosen set of parameters we have $\Delta x/c_s \sim 0.07$, they satisfying this condition for all but the $\tau_f = 0.01\Omega^{-1}$ particles. As noted in Gibbons et al. (2012), this under-resolution of particles does not appear to create any numerical inconsistencies in the evolution of the smallest particles.

Each particle species with a fixed radius is distributed spatially uniformly with the average surface density of $\Sigma_{0p} = 10^{-2}\Sigma_0$, except in the low mass case studied, where we take $\Sigma_{0p} = 10^{-3}\Sigma_0$ prescribed according to the standard value of dust-to-gas ratio. The particles are initially given random positions within the sheet and zero velocities, relative to the background Keplerian flow, $\mathbf{v}(t = 0) = (0, 0)$.

4.3 Results

4.3.1 Gas Evolution

The evolution of the gaseous component of the disc is in good agreement with that observed in analogous studies based on the shearing sheet formalism (Gammie, 2001; Johnson & Gammie, 2003; Mamatsashvili & Rice, 2009; Gibbons et al., 2012). The small initial velocity fluctuations grow and develop into nonlinear fluctuations in velocity, surface density and potential. Shocks then develop which proceed to heat the gas, while the cooling works to reduce the entropy of the gas. Density structures develop which are sheared out by differential rotation. These density structures tend to take on a trailing nature, which leads to a finite shear stress parameter α (Gammie, 2001). After a few orbits, the heating due to shocks is balanced by the cooling term and the thermal energy of the sheet settles into a quasi-steady self-regulated state, where the thermal, kinetic and gravitational energies of the disc are approximately constant with time. In this state, on the surface density field we clearly see elongated trailing surface density features, or density waves (Figure 5.1). The amplitude of these density waves, and consequently their ability to trap dust particles, is dependent on the cooling time of the gas (Cossins et al., 2009; Gibbons et al., 2012).

In this study we also included the back-reaction of the particles' drag force on the evolution of the gas, a process that was omitted by Gibbons et al. (2012), due to the massless particles adopted by that study. Here we include the back reaction for two values of dust-to-gas mass ratios. Figures 4.1 - 4.5 shows the surface density of the gas and particles at the end of each simulation performed. Generally, the evolution of the gas appears to be identical to the results in

the previous Chapter, where the particles do not affect the gas, however close examination of the $\Sigma_{0p} = 10^{-2}\Sigma_0$ runs shows that when the particle density reaches extremely high concentrations, the wakes of large clouds of particles are evident in the gas. These wakes appear to become more pronounced as the cooling time increases, likely due to the density waves having less robust structure in the simulations with longer cooling times, however in none of the runs do these features appear to have a significant effect on the overall evolution of the gas.

4.3.2 Particle Concentration

The particles, which initially have zero velocities (relative to the Keplerian flow) and random locations within the sheet, are not evolved until the gas has undergone its initial burst phase and settled into a quasi-steady state. Once the gas has reached this phase, we release the dust particles. For the $t_c = 10\Omega^{-1}$ and $20\Omega^{-1}$ runs, the particles are introduced at a time $t_{par} = 10T$, while for the $t_c = 40\Omega^{-1}$ and $80\Omega^{-1}$ runs they are introduced at $t_{par} = 20T$ and $t_{par} = 30T$ respectively. At this point we switch on the drag force between the gas and the dust particles, evolving the system for a further 5 orbits in each case until the dust particles have begun to trace the structure of the gas. Finally we introduce the self-gravity of the particles, evolving the system with both the drag force and particle self-gravity for another 25 orbits.

Once the particles are introduced, they are drawn to local pressure maxima associated with the density waves in the gas. Figure 4.1 shows the logarithmic surface densities of both the gas and dust grains once the system has reached a quasi-steady state at $t = 40T$ in the $t_c = 10\Omega^{-1}$, $\Sigma_{0p} = 10^{-3}\Sigma_0$ run. Comparing the gaseous and dust components of the simulation, we see the same correlation between the density enhancements in the gas and over-densities in the particles observed by Gibbons et al. (2012), the degree to which the presence of spiral density waves affect the particle concentration depends strongly on the friction time of the particles. As observed in Gibbons et al. (2012), the smaller particles, with friction times $\tau_f = [0.01, 0.1, 1.0]\Omega^{-1}$ tightly map the structure which forms due to gravitational instabilities in the gas, whilst the larger particles are not as affected by the drag force and their evolution is not significantly altered by the

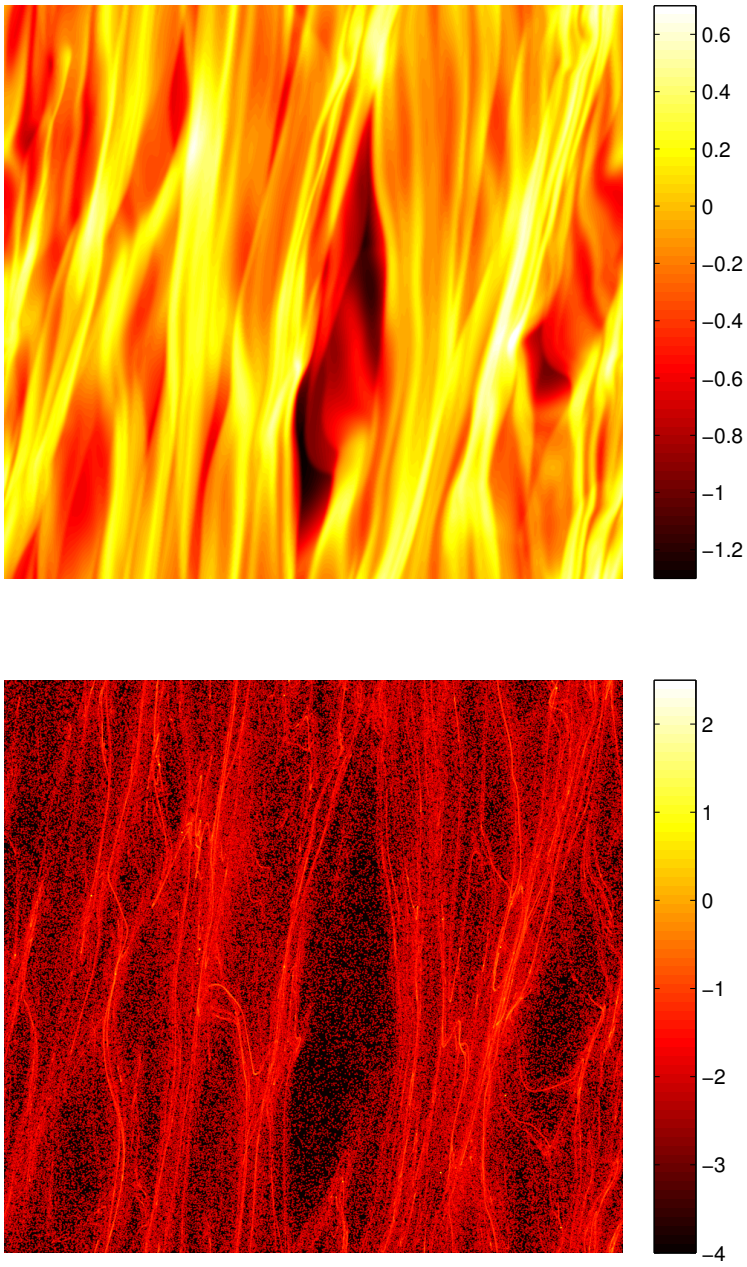

Figure 4.1 *Surface density of the gas (top) and particles (bottom) in the low mass ($\Sigma_p = 10^{-3}\Sigma_0$), $t_c = 10\Omega^{-1}$ simulation. The dust particles are collected in the density waves that form due to gravitational instabilities in the gas.*

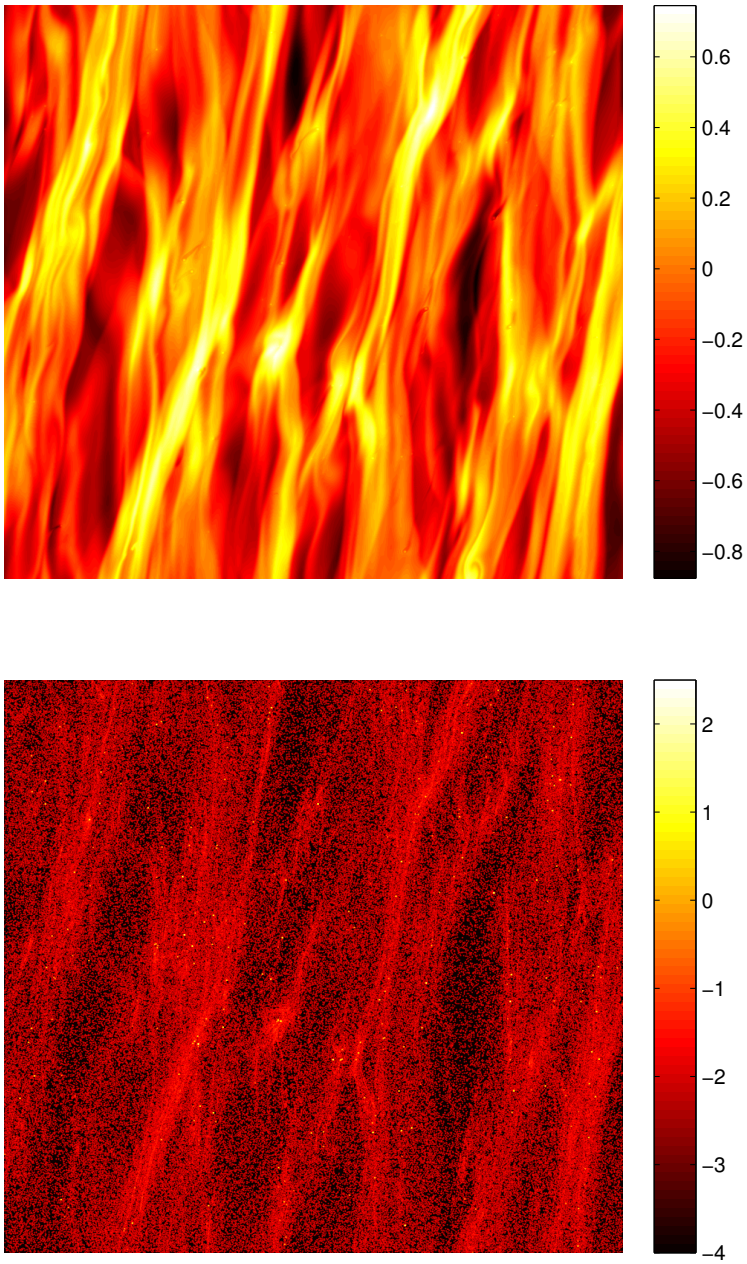

Figure 4.2 *Surface density of the gas (top) and particles (bottom) in the standard $t_c = 10\Omega^{-1}$ simulation. As a result of the particles' gravitational interaction with each other bound clumps of particles form within the spiral density waves. If these clumps reach high enough densities the back reaction on the gas results in the wake of the clumps motion becoming visible in the gas.*

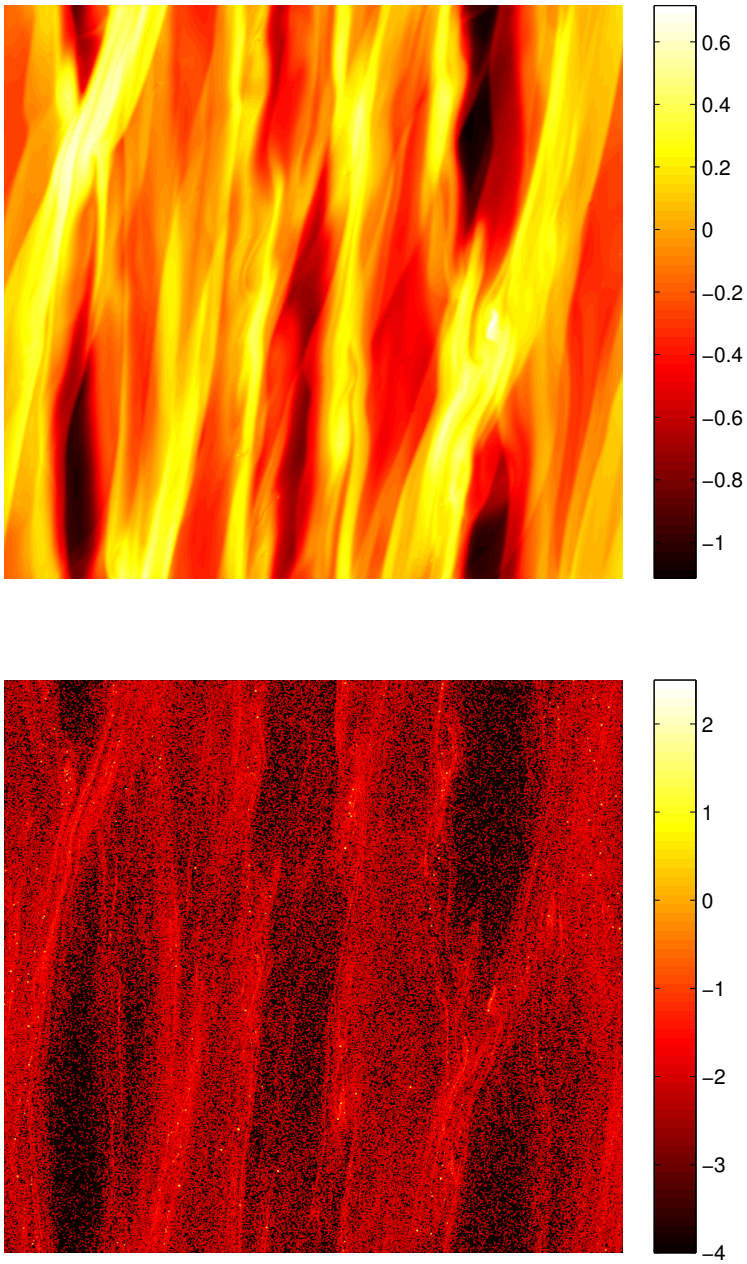

Figure 4.3 *Surface density of the gas (top) and particles (bottom) in the $t_c = 20\Omega^{-1}$ simulation. As a result of the particles' gravitational interaction with each other bound clumps of particles form within the spiral density waves. If these clumps reach high enough densities the back reaction on the gas results in the wake of the clumps motion becoming visible in the gas.*

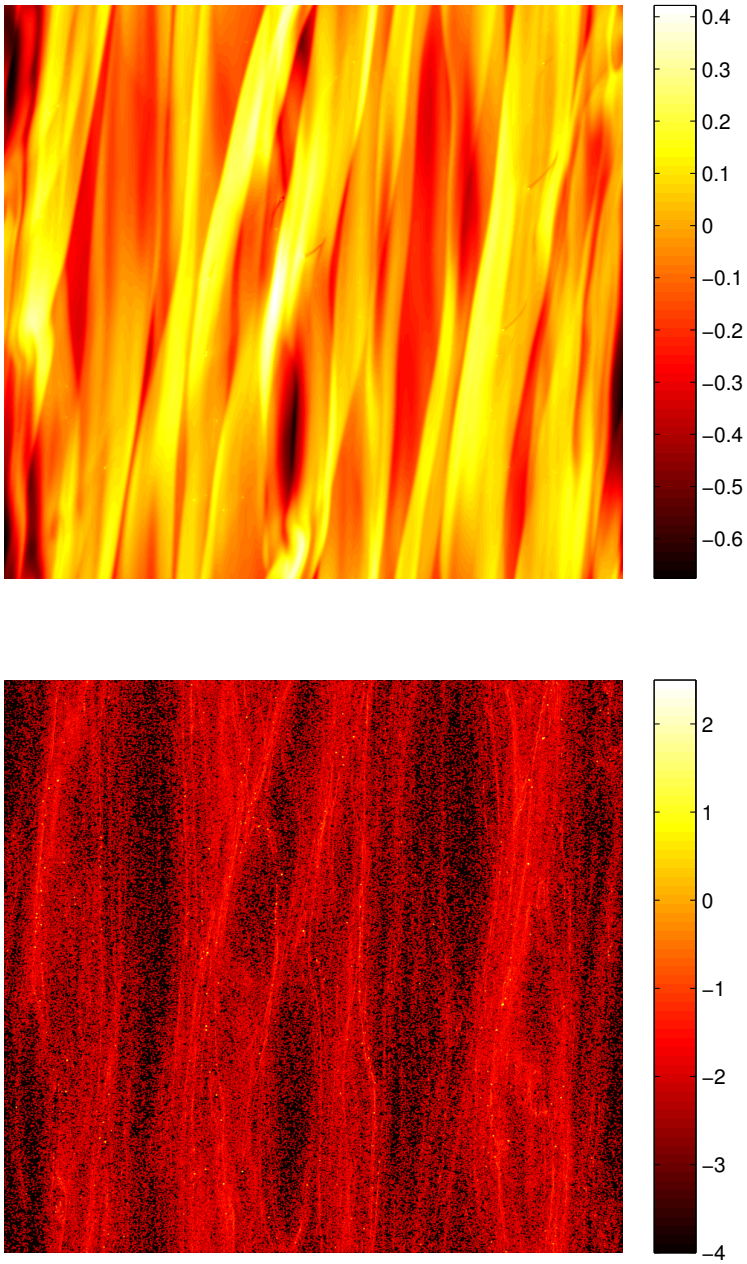

Figure 4.4 *Surface density of the gas (top) and particles (bottom) in the* $t_c = 40\Omega^{-1}$ *simulation. As a result of the particles' gravitational interaction with each other bound clumps of particles form within the spiral density waves. If these clumps reach high enough densities the back reaction on the gas results in the wake of the clumps motion becoming visible in the gas.*

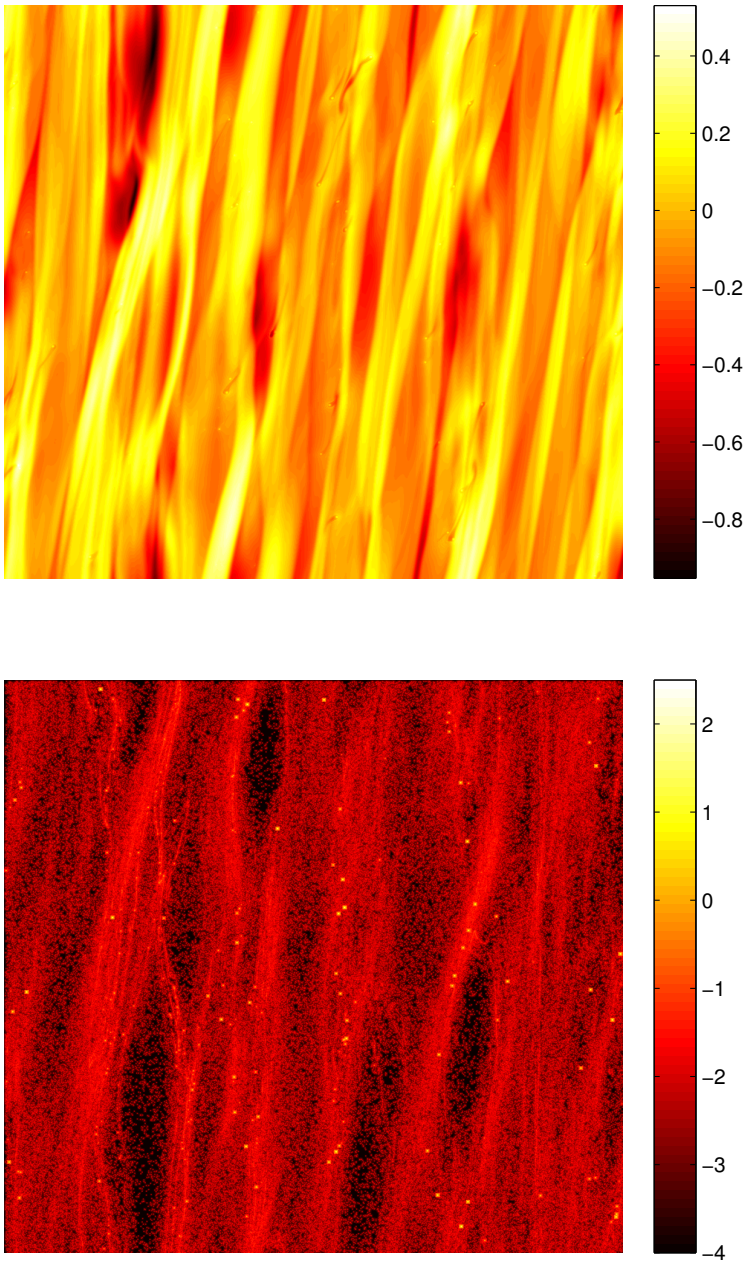

Figure 4.5 *Surface density of the gas (top) and particles (bottom) in the $t_c = 80\Omega^{-1}$ simulation. As a result of the particles' gravitational interaction with each other bound clumps of particles form within the spiral density waves. If these clumps reach high enough densities the back reaction on the gas results in the wake of the clumps motion becoming visible in the gas.*

structure of the gas. Comparing this low mass case with both the higher mass case (Figure 4.2) and the previous massless particle case discussed in the previous Chapter we see that that the inclusion of the particles self-gravity does not have a significant effect on the evolution of the dust particles. The particles evolution in this case is qualitatively the same as the massless case.

Figures 4.2 - 4.5 show the surface density of particles in the simulations with $\Sigma_{0p} = 10^{-2}\Sigma_0$. These figures show that in all cooling times studied, the accumulation of particles within spiral density waves leads to the formation of very high density clouds of particles in the centre of the spiral density waves. These particle clouds form due to the inclusion of the particle self gravity term. Once the particle surface density reaches a certain value, typically equal to the gas, gravitational instabilities set into the solid component of the disc, causing the filaments that form within spiral density waves to contract into several high density objects. Figure 4.6 shows the surface density of the particles at the end of the $\Sigma_{0p} = 10^{-2}\Sigma_0$, $t_c = 10\Omega^{-1}$ simulation decomposed into separate friction times. Here we see that the clouds are primarily composed of intermediate sized particles with friction times $\tau_f = [0.1, 1.0]\Omega^{-1}$. Particles with these friction times are highly concentrated into the density waves and make up the bulk of the mass that is contained in the clumps that form due to the particles self-gravity, with over 90% of the mass in the most massive particle cloud in the simulation with $t_c = 10\Omega^{-1}$ is made up of particles with these cooling times.

The inclusion of self-gravity in the evolution of the dust particles causes the surface density of the particle to reach values ~ 10 times higher than the non self-gravitating case. Figure 4.7 plots the maximum surface density of the particles over time for each cooling time. Although the longer cooling times take longer to reach a steady maximum value, this maximum surface density appears to be largely independent of cooling time, instead being determined by the strength of particle self-gravity (i.e. the total mass of particles in the shearing sheet). By relating the cooling time of the gas used in each simulation to a radial location within the disc, the surface density can be re-expressed as a mass. Figure 4.8 shows the mass of the largest gravitationally bound region of particles within the sheet over time, given typical disc parameters. Here we see that the mass of clumps that form does not really correlate with cooling time (and by extension

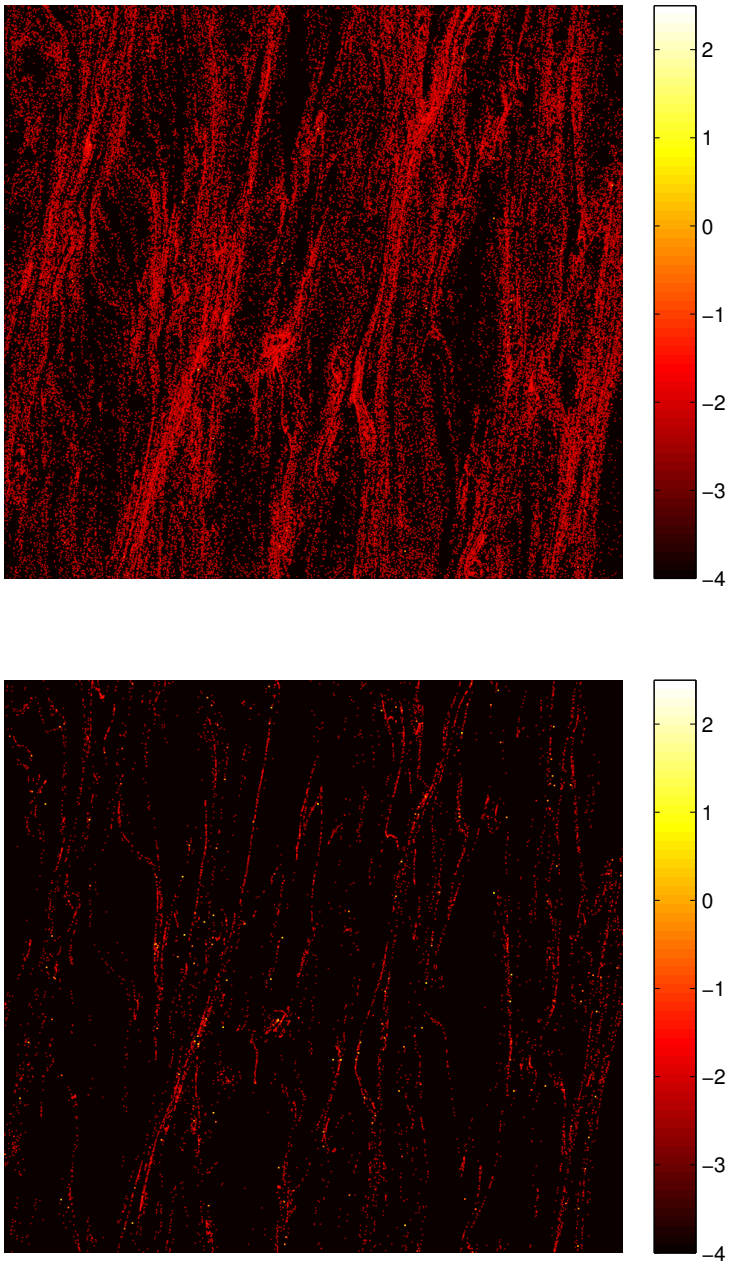

Figure 4.6 *Logarithmic surface density of the $\tau_f = 0.01\Omega^{-1}$ and $\tau_f = 0.1\Omega^{-1}$ particles in the top right corner of the $t_c = 10\Omega^{-1}$ run at $t = 40T$, when the disc is already in a quasi-steady state, or 30 orbits after the drag force between the gas and particles has been turned on.*

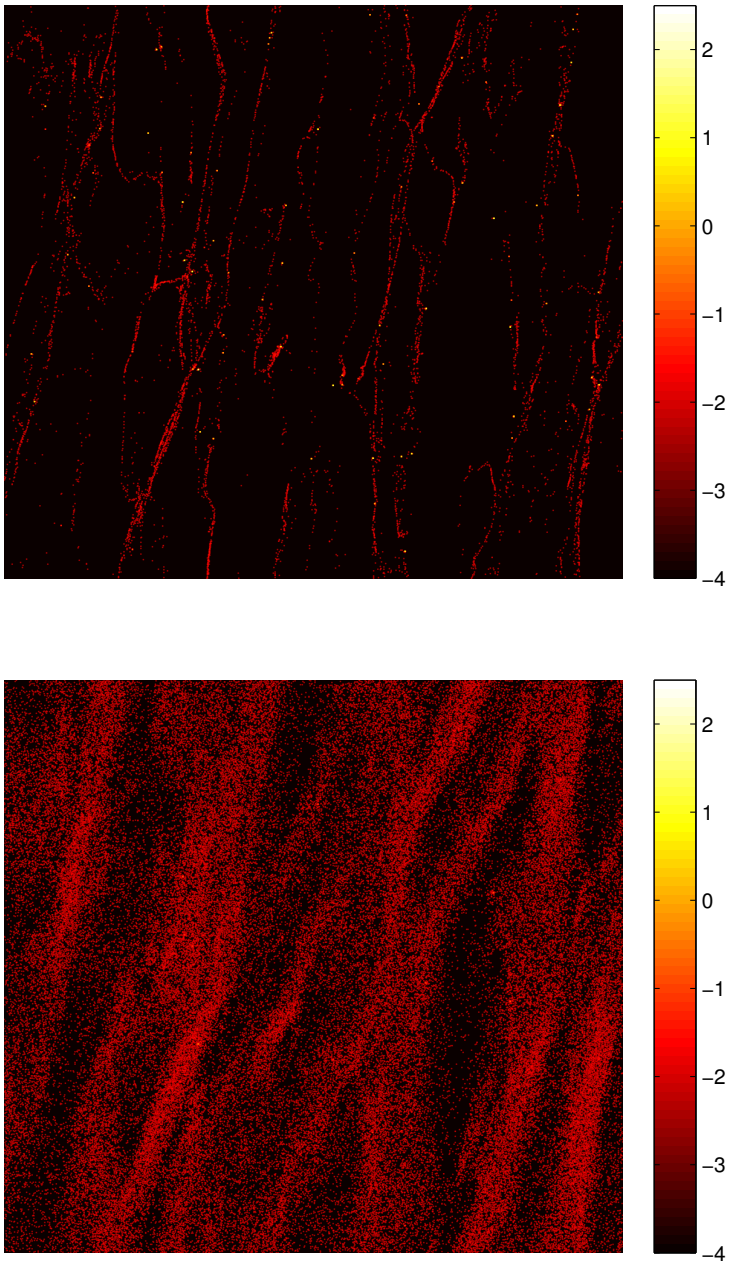

Figure 4.6 **(Continued)** *Logarithmic surface density of the $\tau_f = 1.0\Omega^{-1}$ and $\tau_f = 10.0\Omega^{-1}$ particles in the top right corner of the $t_c = 10\Omega^{-1}$ run at $t = 40T$, when the disc is already in a quasi-steady state, or 30 orbits after the drag force between the gas and particles has been turned on.*

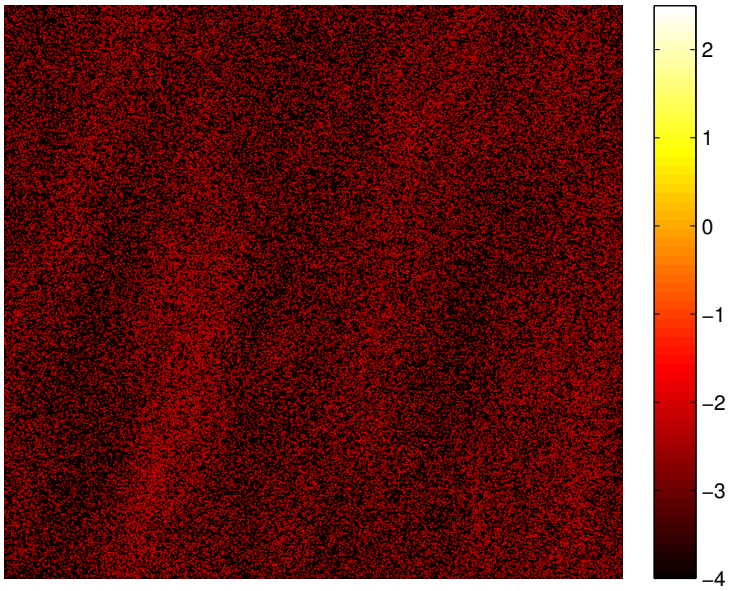

Figure 4.6 **(Continued)** *Logarithmic surface density of the* $\tau_f = 100.0\Omega^{-1}$ *particles and total particle surface density in the top right corner of the* $t_c = 10\Omega^{-1}$ *run at* $t = 40T$*, when the disc is already in a quasi-steady state, or 30 orbits after the drag force between the gas and particles has been turned on. We clearly see a number of highly dense structures which are gravitationally bound. these structure are primarily made up of* $\tau_f = 0.1\Omega^{-1}$ *and* $\tau_f = 1.0\Omega^{-1}$ *particles.*

radius within the disc). Any increase in concentration which occurs in the simulations with lower cooling time tends to be offset by the larger surface density of particles associated with inner radii where the longer cooling times are present.

In practise, it is likely that the particles will also undergo collisional growth as a result of being so densely packed, forming a single object that is likely to be very weakly coupled to the disc via the drag force studied here. As a result of this the simulations detailed here cannot probe the subsequent evolution of planetesimals beyond this point and do not model the shearing sheet for longer time periods, as other effects not modelled here start to affect the evolution of any growing body. Through a more detailed prescription, which takes into account the effects of collisions between particles, a clearer picture of the evolution of these 'rubble piles' can be built up. By replacing the accumulations of particles presented here with a single massive particle and introducing terms describing the migration processes described in Chapter 1, as well as the accretion of gas from the disc onto the growing planet, the late stages of planet formation can be studied.

Figures 4.9 and 4.10 also shows the number of particle clumps which are gravitationally bound, along with the total mass of particles contained in a gravitationally bound structure within a simulation over time. The shorter cooling times tend to form clumps over shorter time periods, the runs with a shorter cooling time producing more gravitationally bound structures over the time period modelled. The total mass contained in bound structures is largely independent of cooling time, for similar reasons mentioned for Figure 4.8. Although the simulations adopting shorter cooling times tend to produce more clumps, and concentrate a higher fraction of the total particle mass available in the simulation into bound clumps, the higher surface densities associated with the inner radii result in the total mass contained in bound structures being higher.

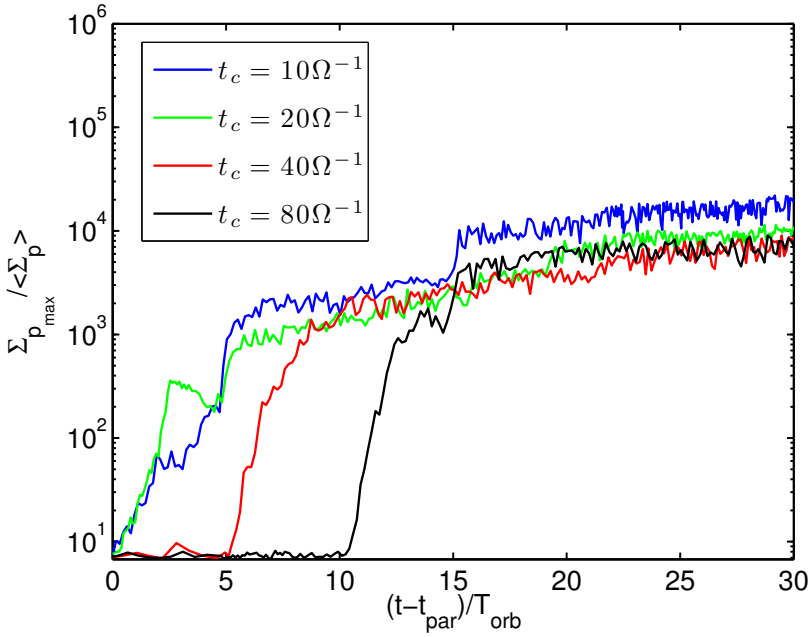

Figure 4.7 *Maximum surface density of the dust particles within the sheet, as a function of time, for each cooling time. There is little correlation between cooling time and the maximum surface density reached, suggesting the particles self-gravity can enable significant density enhancements, even for longer cooling times*

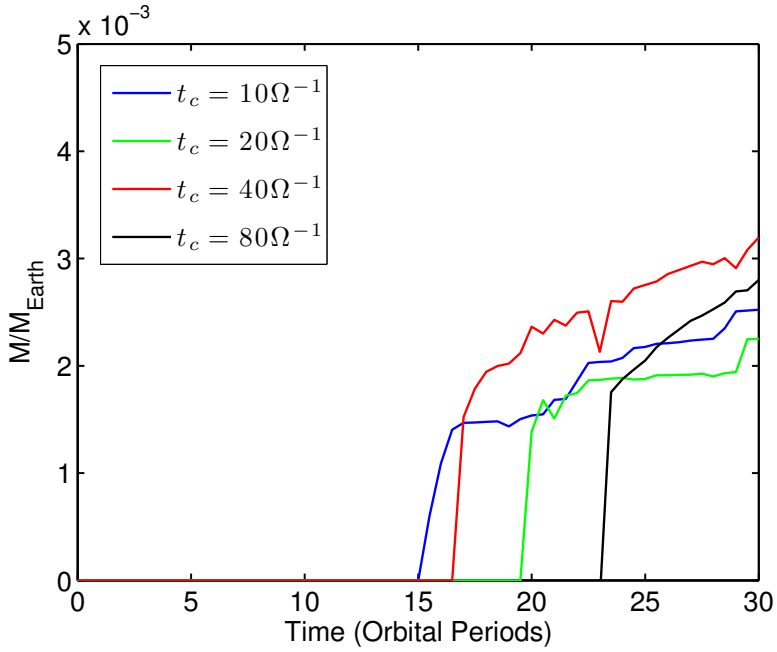

Figure 4.8 *Mass of the largest gravitationally bound collection of particles within the sheet, as a function of time, for each cooling time. The shorter cooling times tend to produce more massive particle clumps, with the shortest cooling time considered*

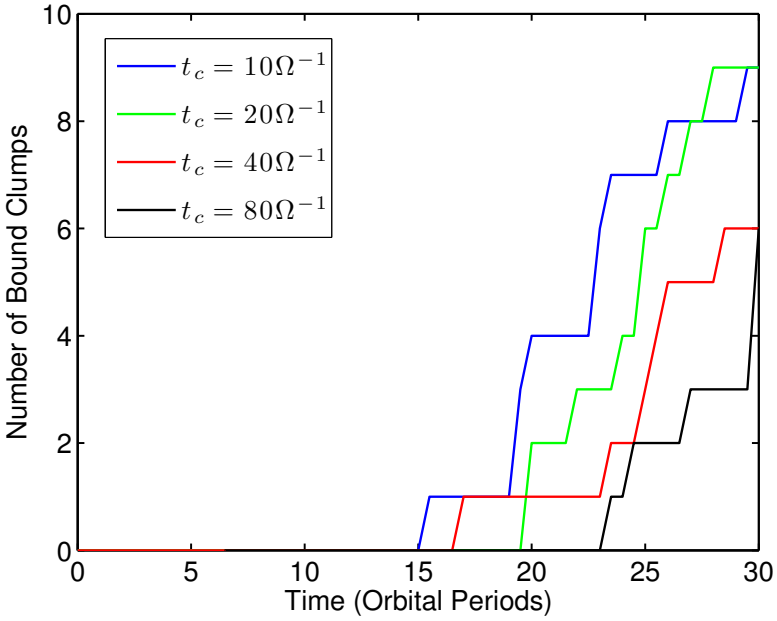

Figure 4.9 *Number of gravitationally bound concentrations of particles in the sheet over time for each cooling time*

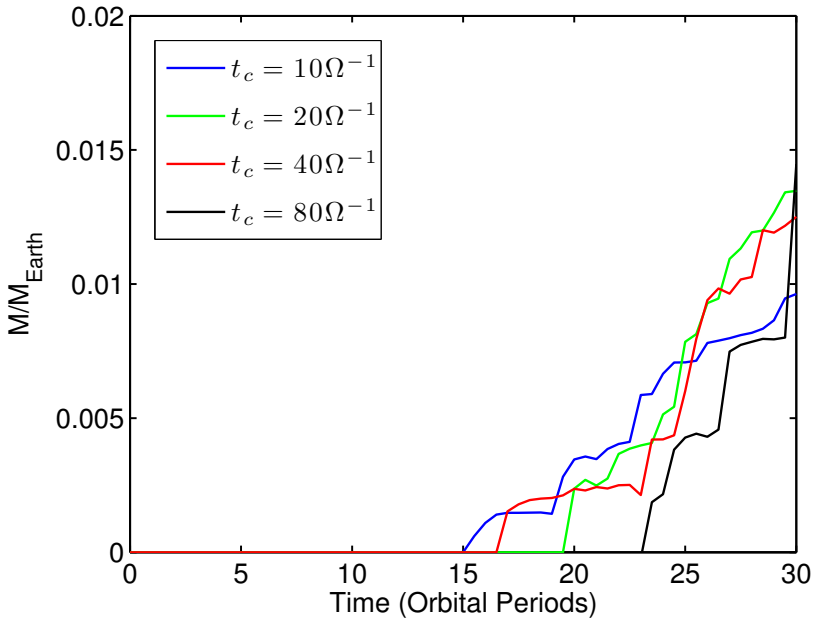

Figure 4.10 *Total mass of gravitationally bound concentrations of particles in the sheet over time for each cooling time*

4.4 Discussion and Conclusions

The work presented in this Chapter expands on the findings of the previous Chapter, presenting a series of simulations modelling the evolution of dust particles in the presence of spiral density waves which occur as a result of gravitational instabilities. In particular this Chapter focusses on the effect that the gravitational interaction between massive dust particles has on their evolution, expanding on the massless 'tracer' particles adopted previously. The general picture of the evolution of the dust particles remains unchanged, the dust particles evolve within a quasi-steady gaseous spiral structure produced by a combined effect of disc self-gravity and cooling. Particles accumulate in spiral density waves, producing significant over-densities in the solid component of the disc, with the magnitude of the enhancement dependent on both the cooling time of the gas and the friction time of the particles.

The introduction of the term modelling particle self-gravity can have several significant effects on the evolution of the disc. The magnitude of the effects

depend on the strength of self-gravity within the simulation. If the mass of the particles is low (i.e. the dust-to-gas mass ratio $\ll 0.01$) the inclusion of the particles self-gravity has no significant effects on the evolution of either the gas or solid component of the disc. For more canonical dust-to-gas mass ratios (~ 0.01), the inclusion of the self-gravity term results in the accumulation of particles which form in spiral density waves contracting further along the crests of the density waves. If the particle concentration is high enough, the particles gravitational interaction becomes sufficiently large to cause local collapse of the solid component of the disc, resulting in the formation of one or more gravitationally bound structures within the disc. The scope of the simulations presented here does not allow us to accurately model the behaviour of the dust particles within these structures, with many of these structures occupying a single pixel on the grid, and we cannot precisely determine whether these structures tend to take the form of loosely bound rubble piles, or coalesce into a single large objects via collisional growth. Assuming typical disc parameters however predicts masses for these structures to be comparable to very large planetesimals, with the most massive structures identified comparable to dwarf planet masses, providing seed objects for the growth of terrestrial planets and giant planet cores. These structures are robust enough to survive in the disc, even after the spiral density wave they formed in has been sheared out and the remainder of the solid particles have diffused back into the disc. Interestingly, the physical mass of these structures is only loosely related to the cooling time of the disc. Although short cooling times are more efficient at trapping particles within density waves, resulting in structures forming faster and usually accounting for a larger fraction of the particles, for a given disc, the lower surface density of material present at the larger radii associated with these shorter cooling times tends to offset this, suggesting that density waves arising from gravitational instabilities in the gas are able to produce large scale planetesimals, even if the effects of self-gravity are relatively weak. The full extent of the region where this mechanism can operate is beyond the scope of the simulations performed here, as to probe regions interior to $\sim$ 10AU, very long cooling times are required, which are not feasible for the simulations posed here, as for such one cooling times, numerical viscosity will begin to dominate the shear stresses, requiring us to perform higher resolution studies.

In conclusion the finding of the work presented in this Chapter tend to support and expand upon those outlined in Chapter 3. The picture of planet formation proposed at the end of Chapter 3 is still an attractive method for the rapid creation of a reservoir of planetesimals, along with several very massive objects of $\sim 0.01 M_{Earth}$, which are likely to continue to grow via the accretion of smaller bodies, potentially reaching terrestrial planet masses. One of the key advancements of this study is the possibility of this mechanism allowing the formation of planetesimals at a larger range of radii than previously thought. The results of the work presented in the previous Chapter indicated that the enhancements in the surface density of the disc are unlikely to be significant at radii less than $\sim$ 20AU. The results presented here suggest that the particles self-gravity may allow for planetesimal formation due to density waves at much smaller radii within the disc, however higher resolution simulations are required to probe the exact range of this mechanism.

Chapter 5

Particle Trapping by Vortices in Self-gravitating Discs

5.1 Introduction

Research in the field of proto-planetary disc dynamics is generally focused on studying one of two types of perturbations that commonly occur. In the early stages of disc evolution large scale spiral density waves are thought to commonly arise in massive discs as a result of gravitational instabilities within the disc. It has been known for some time that this gravitational instability can act to transport angular momentum outwards, allowing mass to accrete onto the protostar (Lin & Pringle, 1987) and could well be the primary transport mechanism during the earliest stages of star formation (Lin & Pringle, 1987).

The other common perturbation type in discs that has received much attention, partly in connection with planetesimal formation, are vortices. They can arise in both self-gravitating and non-self-gravitating discs provided there is some localized radial structure in the disc triggering Rossby wave instability that in turn results in vortex formation (Lovelace et al., 1999; Li et al., 2000, 2001). Alternatively, vortices can also be generated as a result of other hydrodynamic instabilities, such as baroclinic instability (Klahr & Bodenheimer, 2003) or

Kelvin-Helmholtz instability of vorticity strips (Lithwick, 2007). Although the dynamics and evolution of vortices in non-self-gravitating discs has been under active investigation for a while, since the first idea of their relevance to planet formation by Barge & Sommeria (1995), systematic studies on vortex dynamics in self-gravitating discs appeared only recently (Mamatsashvili & Rice, 2009; Lyra et al., 2009). It was commonly thought before that spiral density waves are the only perturbation type present in self-gravitating discs and the existence of other modes also participating in the overall disc dynamics had been left out of consideration in many studies of self-gravitating discs. Recent developments in the theory of non-self-gravitating discs have shown that vortices can be (linearly) coupled with and excite spiral density waves due to the disc's differential rotation (Bodo et al., 2005; Johnson & Gammie, 2005). This effect was confirmed to be even more efficient in the presence of self-gravity (Mamatsashvili & Chagelishvili, 2007). Moreover, a linear analysis by Mamatsashvili & Chagelishvili (2007) showed that in fact the vortical mode is also subject to the influence of self-gravity and can exhibit gravitational instability with amplification factors comparable to that of density waves. This clearly implies that vortices are an important part in the formation of a complete dynamical picture of self-gravitating discs.

Trapping of dust particles by spiral density waves and the possibility of planetesimal formation via this process were studied in both global (Rice et al., 2004, 2006) and local shearing sheet simulations (Gibbons et al., 2012) of self-gravitating discs. It was demonstrated that density waves are efficient at trapping solids, especially those with stopping times comparable to the local orbital period. The gas pressure gradient changes from positive to negative across the density wave structure, creating sub-Keplerian velocities on one side of the wave, and super-Keplerian on the other. As a result, the drag force causes dust grains to drift toward the density/pressure maxima at the crest of density waves. This can eliminate two problems currently challenging theories of planet formation. Firstly, concentration of solid material trapped within a spiral arm can become locally much larger than the average within the disc, so that particle agglomerations there will collapse due to their own self-gravity, possibly leading to the faster creation of planetesimals. Secondly, particle trapping in local pressure maxima can also prevent growing objects from rapidly drifting inwards and being lost from the disc.

Dust trapping by pressure maxima associated with (anticyclonic) vortices is based on a similar physical mechanism and, as mentioned above, has been extensively covered, though only in non-self-gravitating discs. So, the role of vortices in trapping dust in self-gravitating discs is less understood and needs further investigation. Particle concentration by vortices in the presence of disc self-gravity has been first addressed by Lyra et al. (2009) in global disc simulations. However, in their set-up vortices were generated by a Rossby wave instability in an otherwise laminar disc and had a long-lived regular nature, as in the non-self-gravitating case, though smaller azimuthal size due to the effect of self-gravity. Here, we consider a different situation – a self-gravitating disc in a quasi-steady gravitoturbulent state, without baroclinic or Rossby wave driving, and analyse the behaviour of dust particles embedded within it using the shearing sheet approximation. As shown by Mamatsashvili & Rice (2009), this state consists of transient short-lived small-scale vortices producing overdense regions overlaid on shocks of density wave structures. In other-words, we extend this study by adding dust particles with a goal of understanding the role these structures play in dust evolution. Dust dynamics in the presence of only density waves in the shearing sheet has been explored in Chapters 3 and 4, where larger box sizes were used. Here, we take smaller box sizes and higher resolution, so that vortical structures are also resolved and study the efficiency of dust trapping by transient vortices against the backdrop of density variations due to the shocks. This will help us to establish the role of vortices in planet formation process in self-gravitating discs.

This Chapter is organized as follows. In Section 2, we outline the parameters adopted in these simulations. In Section 3, we discuss the evolution of the dust particles in the presence of the vortex structure. Finally, we draw our conclusions in Section 4.

5.2 Model

The model adopted in this study remains identical to that outlined in Chapter 4. Here we outline the parameters adopted in this study.

5.2.1 Units and Initial Conditions

We normalise our parameters by setting $c_{s,0} = \Omega = \Sigma_0 = 1$. The time and velocity units are $[t] = \Omega^{-1}$ and $[v] = c_{s,0}$, resulting in the orbital period, $T = 2\pi$. The unit of length is the scale height, $[l] = H = c_{s,0}/\Omega$. We initialise the Toomre-Q parameter to be 1 throughout the sheet. This sets the gravitational constant $G = \pi^{-1}$. The surface density of gas is initially set to be unity everywhere in the sheet. We take the cooling time, $t_c = 20\Omega^{-1}$. This ensures that the disc does not fragment, and the gas settles into a quasi steady state. The box is of length $L = 20G\Sigma/\Omega^2$ and is divided into a grid of 1024^2 cells. This choice of units sets the sheet length $L = 20H/\pi \sim 6.5H$.

The gas velocity field is initially perturbed by some small random fluctuations with the rms amplitude $\sqrt{< \delta \mathbf{v}^2 >} = 10^{-3}$. We take the viscosity and diffusion coefficients to be $\nu = 10^{-4}$ and $\nu_{sh} = D_{sh} = 1.0$. We use 5×10^5 particles, split evenly between five friction times, $\tau_f = [0.01, 0.1, 1, 10, 100]\Omega^{-1}$.

We run two simulations, mimicking the regimes probed by the previous two Chapters. The first simulation adopts massless, tracer particles as used in Chapter 3 to study the particle trapping properties of the vortices. The second case adopts massive particles and includes the self-gravity of the particles, adopting the canonical dust to gas density ratio of $\epsilon = 0.01$.

5.3 Results

5.3.1 Gas Evolution

The evolution of the gaseous component of the disc is in good agreement with that observed in previous studies of vortices in self-gravitating discs; e.g. Mamatsashvili & Rice (2009). The small initial velocity fluctuations grow and develop into nonlinear fluctuations in velocity, surface density and potential. Shocks then develop which proceed to heat the gas, while the cooling works to reduce the entropy of the gas. Density structures develop which are sheared

out by differential rotation. These density structures tend to take on a trailing nature, which leads to a finite shear stress parameter α, which is dependant on the cooling time of the simulation (Gammie, 2001). After a few orbits, the heating due to shocks is balanced by the cooling term and the system settles into a quasi-steady self-regulated state, where the thermal, kinetic and gravitational energies of the disc are approximately constant with time. The surface density of the gas at the end of the massless particle run is shown in Figure 5.1.

The vortex structure is defined in the sheet via the potential vorticity (PV),

$$\epsilon \equiv \frac{(\nabla \times \mathbf{u}) \cdot \hat{\mathbf{z}} + (2-q)\Omega}{\Sigma}. \tag{5.1}$$

During the initial shock phase, small scale positive and negative PV regions get strongly sheared into strips, but negative PV (anticyclonic) regions start to wrap up into vortex-like structures due to nonlinear Kelvin-Helmholtz instability (Lithwick, 2007). The positive PV regions remain sheared into strips showing no signs of vortex formation during the entire course of evolution. Therefore only the anticyclonic regions with negative PV are able to survive in shear flows by taking the form of vortices. The PV field associated with Figure 5.1 is shown in Figure 5.2. Figure 5.2 shows several anti-cyclonic vortex structures characterised by negative PV regions have developed in the sheet. The most prominent of these structures is located in the centre-left of the figure. In non-self gravitating discs, these anti-cyclonic vortices have been shown to be efficient at trapping dust particles in the centre of the vortex (Johansen et al., 2004). In Section 5.3.2 we describe the particle trapping properties of these anticyclonic regions in discs where the gas is self-gravitating.

5.3.2 Particle Concentration

The dust particles initially have zero velocities and random positions within the sheet are released after ten orbital periods. At this point the gas has settled in a quasi steady state. At this point in time we introduce the aerodynamic drag force term into the particles evolution. The simulation with massless tracer particles is then evolved for a further 30 orbits, after which the particles have settled into

Figure 5.1 *Surface Density of the gas at the end of the massless particle run. The Potential Vorticity field of the simulation at this time is shown in Figure 5.2, the dust particles are shown in Figure 5.3.*

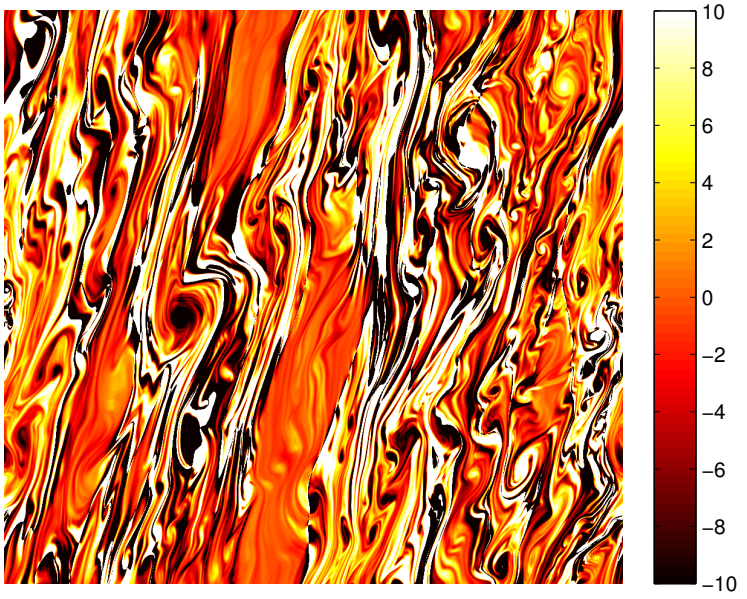

Figure 5.2 *Potential Vorticity field at the end of the simulation with massless particles. The colourmap is restricted to the range* -10 *to* $+10$ *to emphasise the presence of vortex structure.*

a quasi steady state. In the simulation with massive particles the particles are evolved for five orbital periods, without their-self-gravity, until the particles have begun to trace the structure of the gas. At this point we introduce the particles self-gravity and evolve the simulation for a further 10 orbits. At this point the time step of the simulation becomes sufficiently small that it becomes impractical to evolve the particles further, however inspection of the particles evolution up to this point indicates that the particles have been sufficiently evolved to understand their behaviour, especially when compared to the results presented in previous chapters.

The surface density of the particles at the end of the massless particle run is shown in Figure 5.3. As demonstrated in previous Chapters, the intermediate sized particles with friction times $\tau_f = [0.1, 1.0]\Omega^{-1}$ are most efficiently trapped in density structures within the gas, with the $\tau_f = 1.0\Omega^{-1}$ displaying considerably more concentration within density waves than any of the other stopping times. Of particular interest for the work presented in this chapter is the behaviour of the dust particles in the vicinity of vortices. Unlike the simulations presented in Johansen et al. (2004), the particles do not accumulate at the centre of anticyclonic vortices, in fact the opposite appears to occur, the particles that are trapped within a density waves tend to accumulate in a spiral structure around the centre of a vortex, however do not drift into the centre of the structure. This behaviour is most clearly demonstrated in the surface density of the $\tau_f = 0.1\Omega^{-1}$ particles. Here we see several noticeable 'dead zones' corresponding to negative PV regions in Figure 5.2, where there are no dust particles, surrounded by a spiral or ring of dust particles, typically reaching high density augmentations comparable to those present in the large scale shearing boxes investigated in the previous Chapters.

These structures in the particle density fields are transient, their evolution is linked to the evolution of the features in which they form. As the density waves or vortex structure they form within is sheared away as a result of the velocity gradient of the sheet, so is any particle accumulation that has formed alongside the perturbation. This behaviour is visible in the top-left hand corner of the $\tau_f = 1.0\Omega^{-1}$ particle density field. Here we see the remnants of a vortex structure that is in the final stages of being sheared out by the differential flow. The

dust particles are focussed into a single high density filament, reaching particle densities that are likely to condense into bound, planetesimal mass objects.

As mentioned above, the particles do not fall into the centre of the vortex structures, instead circulating on the edge of the vortex structure. This contradicts the behaviour observed when the gas is not self-gravitating. This change in behaviour appears to be due to the vortices in the self-gravitating case evolving into hydrostatic structures. In this regime the pressure forces within the vortex structure are balanced by the self-gravity of the gas, resulting in no pressure gradient across the vortex. This results in particles travelling around the vortices in a spiral structure, forming the ring of particles around the vortices observed in Figure 5.3.

The second simulation performed introduced the self-gravity of the particle component of the disc once the dust particles have begun to trace the structure of the gas. Figure 5.4 shows the surface density of the particles at the end of this run decomposed into individual friction times. In Figure 5.4 the effect of the particles self-gravity clearly dominates the intermediate sized particles evolution, similar to the sheets spanning a larger domain studying density waves in Chapter 4. In this run the particles self-gravity again results in the formation of several high density objects which are gravitationally bound, with structures surviving the decay of the perturbation in which they formed. In this smaller domain, the overwhelming majority of intermediate sized particles are channeled into these structures. In the massive particle run, particles tend to be rapidly swept up by a spiral density wave and tend to trace out vortices which form alongside or within the density wave, similar to the major vortex present in the non self-gravitating case shown in Figures 5.1 - 5.3. This tends to result in a relatively large number of dust particles becoming concentrated around vortices in the gas. This enhancement tends to result in rapid collapse of the solid component of the disc when its self-gravity is introduced. This sequence of events can be seen in Figure 5.5. Here we see the maximum surface density, relative to the mean, in the sheet as a function of time for the two cases. For the first five orbits, the two cases are almost identical. The simulation with massive particles experiences slightly less enhancement in the solid component of the disc due to the effect of the back-reaction of the particles, however both cases still experience local densities $\sim 10^2 - 10^3$ times higher than

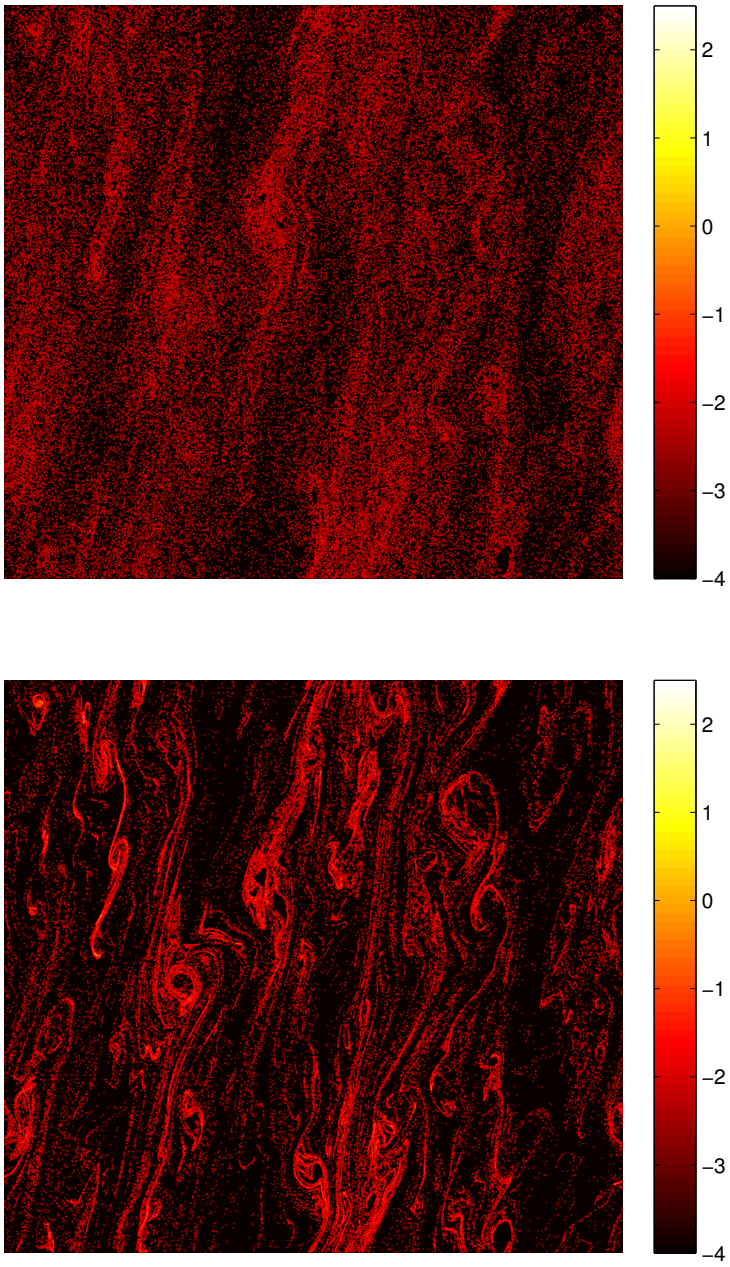

Figure 5.3 *Logarithmic surface density of the* $\tau_f = 0.01\Omega^{-1}$ *and* $\tau_f = 0.1\Omega^{-1}$ *particles at the end of the massless particle run.*

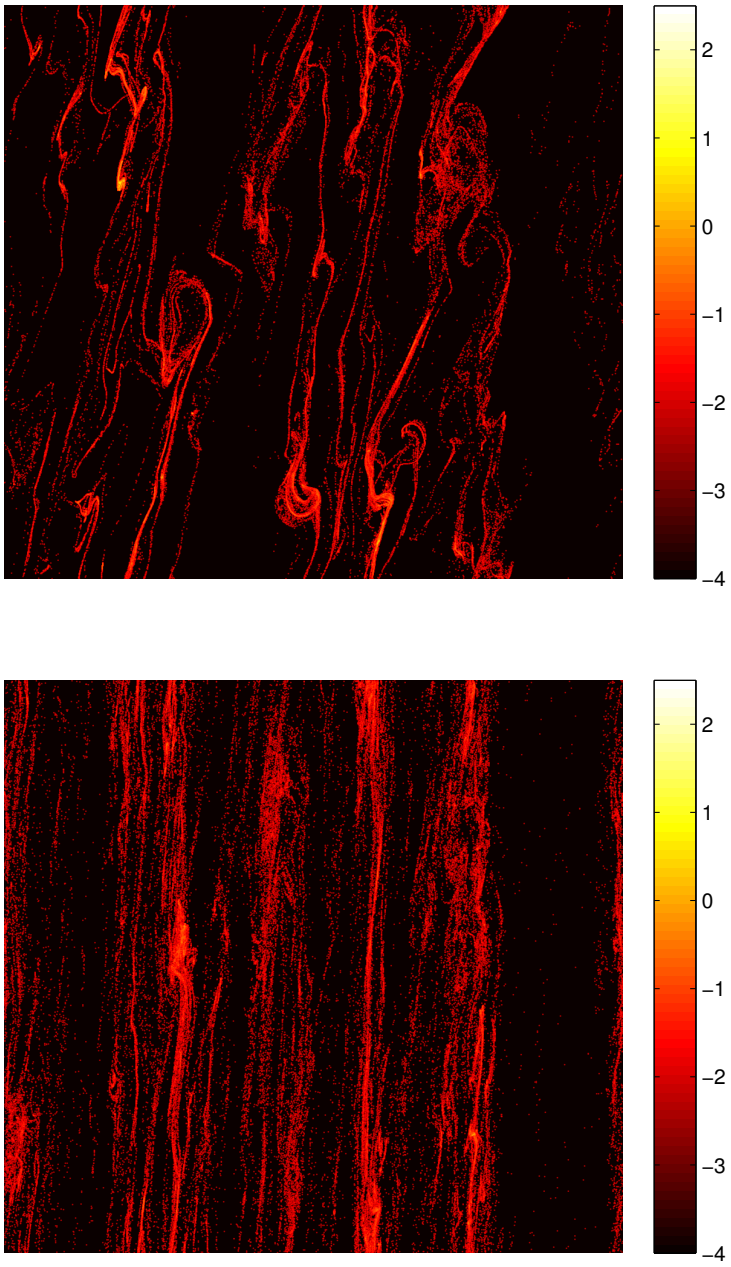

Figure 5.3 **(Continued)** *Logarithmic surface density of the* $\tau_f = 1.0\Omega^{-1}$ *and* $\tau_f = 10.0\Omega^{-1}$ *particles at the end of the massless particle run.*

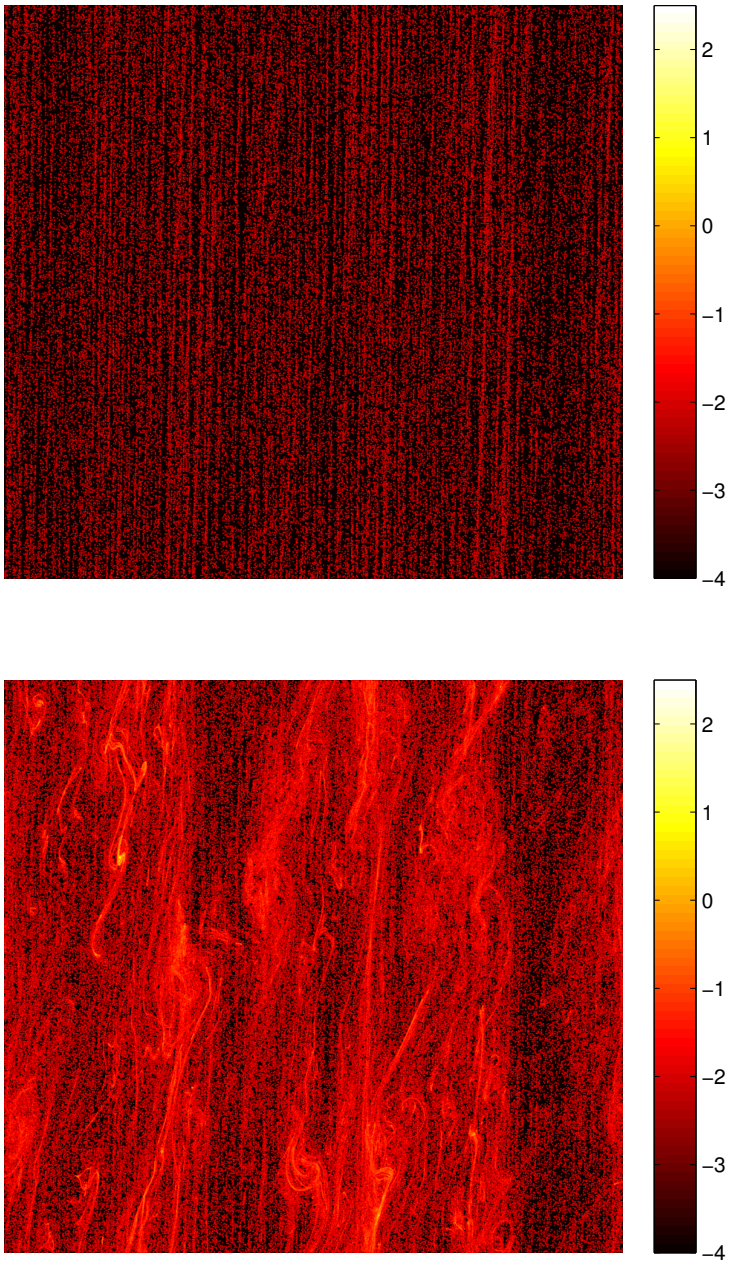

Figure 5.3 **(Continued)** *Logarithmic surface density of the* $\tau_f = 100.0\Omega^{-1}$ *particles and the combined particle surface density for the massless particle run. The surface density of gas at this time is shown in Figure 1 and the vorticity field is shown From these panels we see that intermediate-sized particles are captured effectively in density waves, preferentially surrounding anti-cyclonic vortices.*

the mean density within the sheet. For typical gas to dust ratios, this results in the solids locally reaching densities comparable to the gas. After five orbits the self-gravity of the dust particles is introduced, corresponding to a sharp rise in the particles' surface density, until particle surface densities have reached values as high as 10^4 times the mean. As in the previous chapter, densities this high indicate the presence of gravitationally bound particle clumps. Figure 5.6 shows the surface density of the intermediate size particles two orbits after the particle self-gravity is introduced. Figure 5.6 shows that bound clumps of particles tend to form in the rings of particles that surround anticyclonic vortices fastest, with the high density regions in Figure 5.6 located around the 'dead zones' which correspond to anticyclonic vortices. Additionally these objects tend to form in groups, with several high density structures present around the vortex present in the top-left crier of the sheet.

Over time, the vortex structure begins to shear out, and these objects coalesce due the gravitational interaction between the objects. These mergers correspond to the two smaller jumps in density in Figure 5.5. At the end of this run, the particles have reached density enhancements as high as 5×10^4 times the mean particle density, several times higher than the densities observed in the previous chapters, where particles are exclusively trapped in spiral density waves.

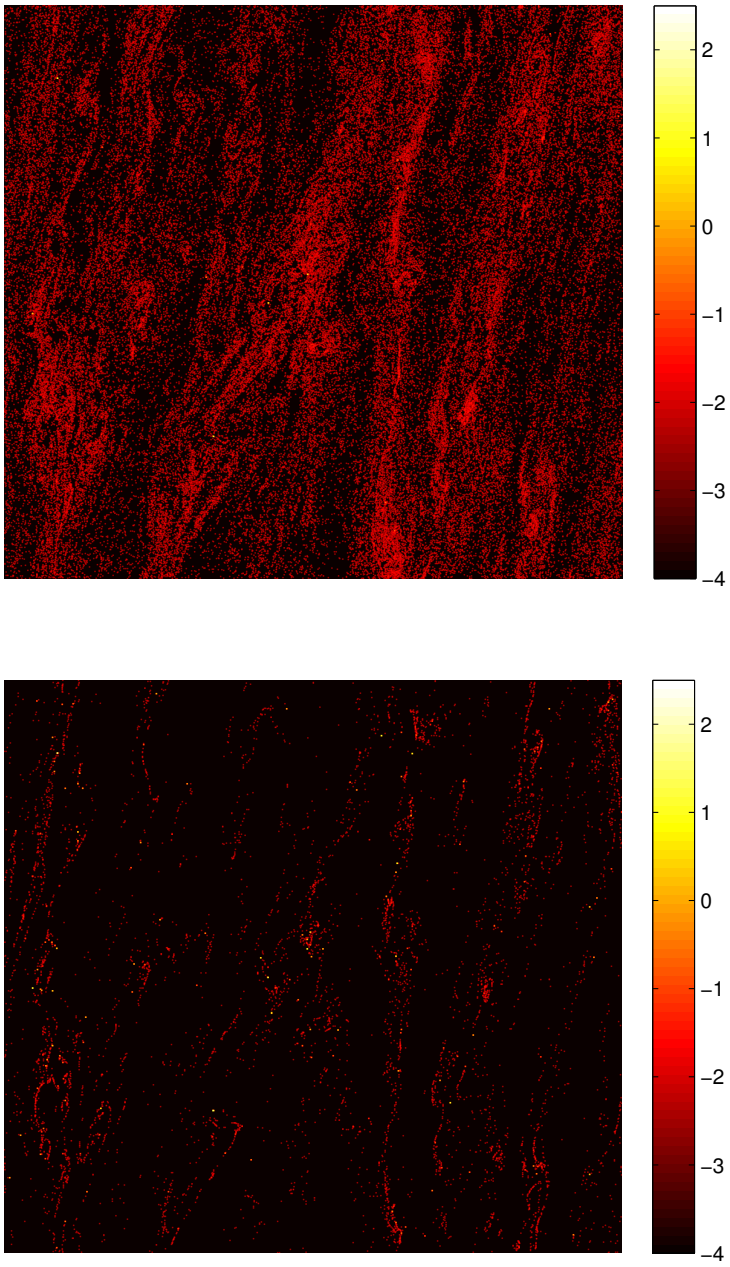

Figure 5.4 *Logarithmic surface density of the* $\tau_f = 0.01\Omega^{-1}$ *and* $\tau_f = 0.1\Omega^{-1}$ *particles at the end of the massive* ($\Sigma_p = 10^{-2}\Sigma_0$) *particle run.*

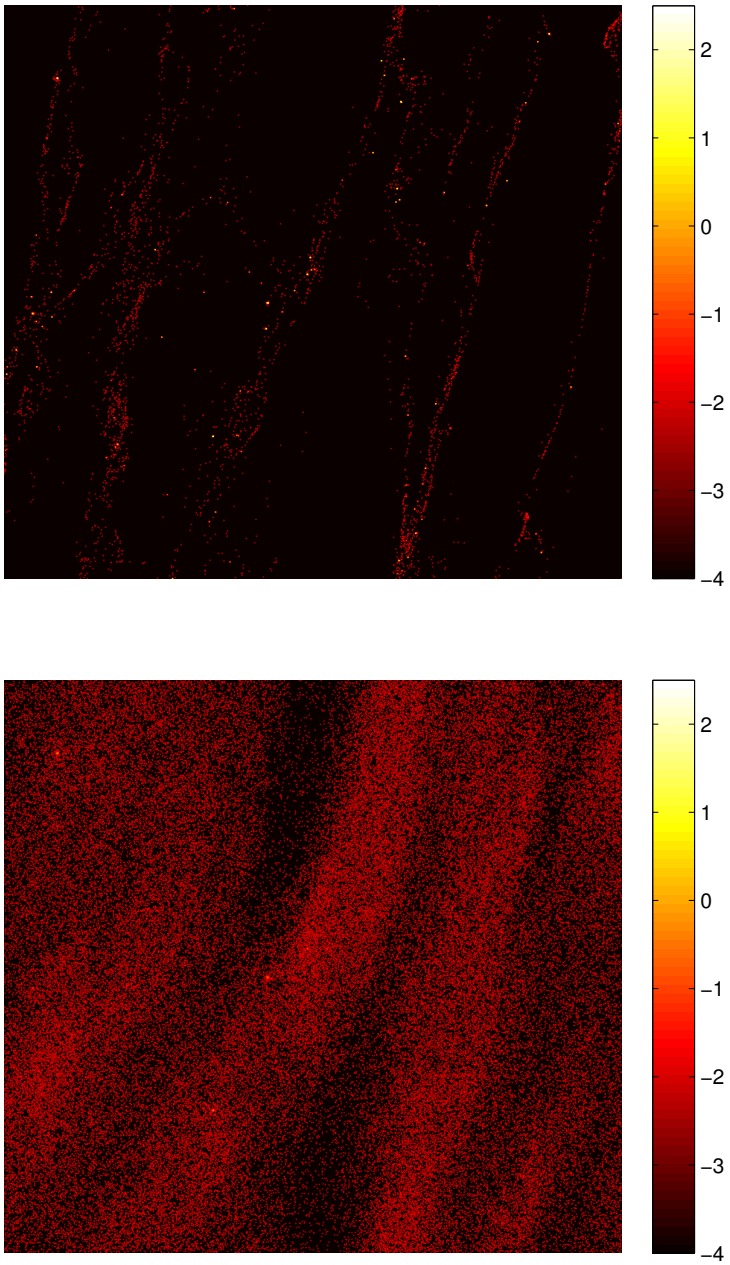

Figure 5.4 **(Continued)** *Logarithmic surface density of the* $\tau_f = 1.0\Omega^{-1}$ *and* $\tau_f = 10.0\Omega^{-1}$ *particles at the end of the massive* ($\Sigma_p = 10^{-2}\Sigma_0$) *particle run.*

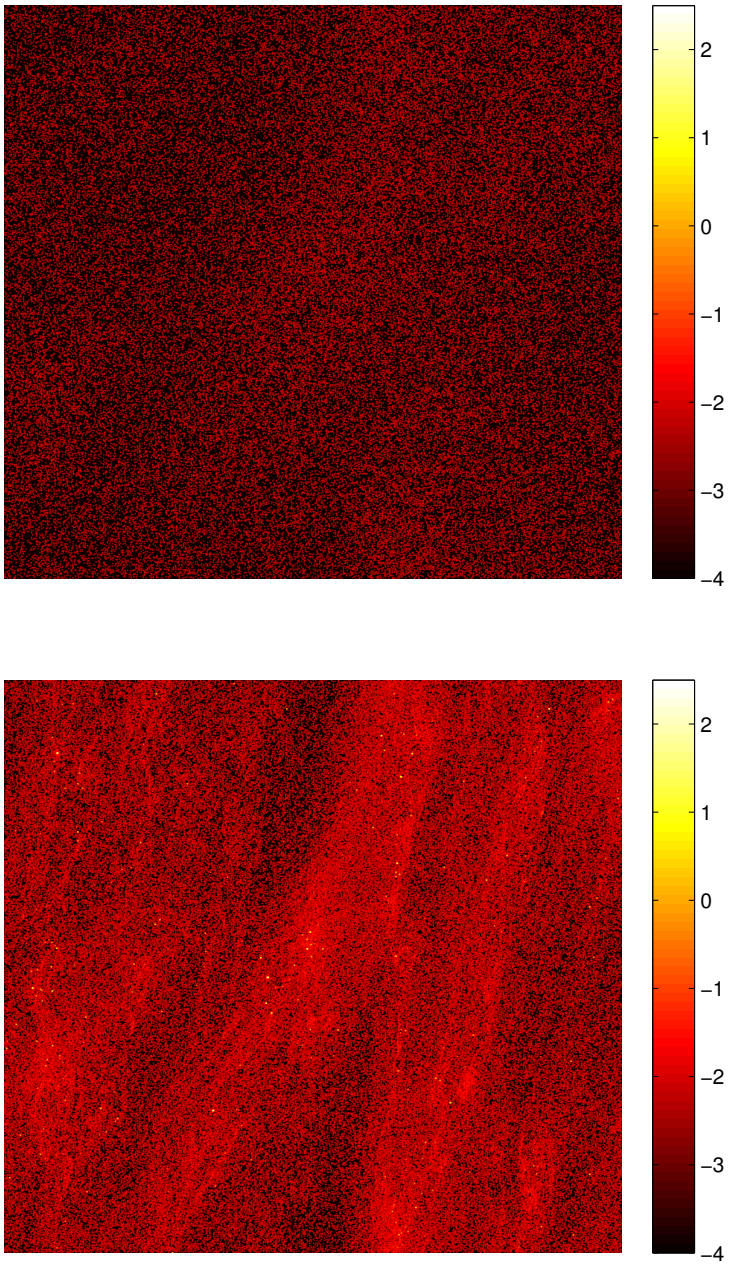

Figure 5.4 **(Continued)** *Logarithmic surface density of the* $\tau_f = 100.0\Omega^{-1}$ *particles and the combined particle surface density for the massive* ($\Sigma_p = 10^{-2}\Sigma_0$) *particle run. As a result of the augmented particle concentration, gravitationally bound clumps of particles form within the structures present on the gaseous component of the disc.*

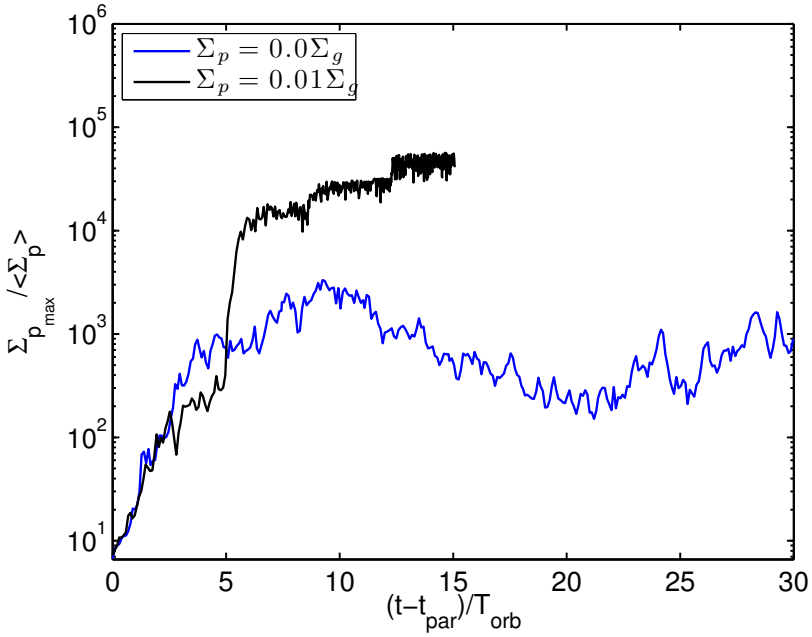

Figure 5.5 *Maximum surface density of the particles within the sheet as a function of time for both simulations performed.*

5.4 Conclusion

The work presented in this Chapter uses a similar simulation setup to that adopted in Chapters 3 and 4 to study the particle trapping properties of vortex perturbations and the impact vortices can have on the planet formation process. Again the general picture of planet formation detailed by the previous two Chapters remains unchanged, the dust particles evolve within a quasi-steady gaseous spiral structure produced by a combined effect of disc self-gravity and cooling. Particles accumulate in spiral density waves, producing significant over-densities in the solid component of the disc, with the magnitude of the enhancement dependent on the friction time of the particles. The work performed here gives us a better picture of how particles trapped in spiral density waves evolve due to the increased resolution of the simulations performed.

The work performed here uses a smaller simulation domain whilst retaining the same number of grid points. The resulting increase in resolution allows small scale perturbations to be studied which results in vortex structure forming in

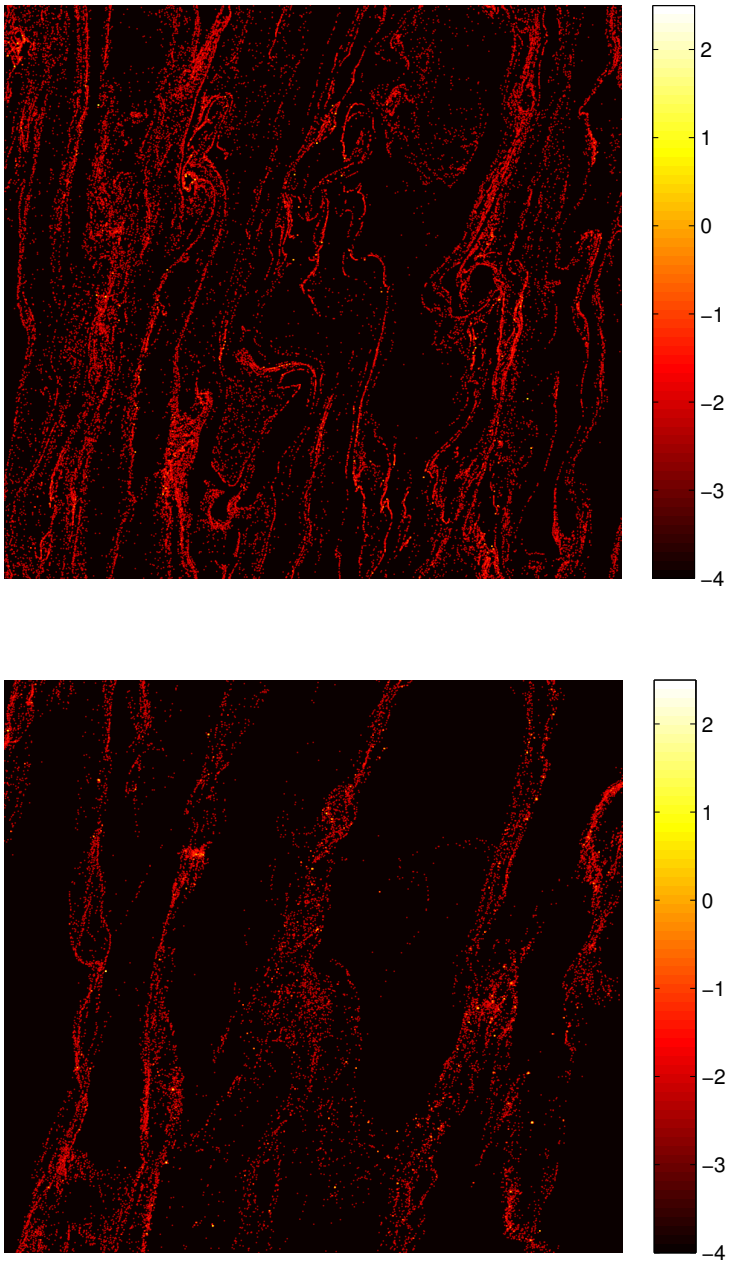

Figure 5.6 *Logarithmic surface density of the* $\tau_f = 0.1\Omega^{-1}$ *and* $\tau_f = 1.0\Omega^{-1}$ *particles seven orbits after the dust particles are released in the massive* ($\Sigma_p = 10^{-2}\Sigma_0$) *particle run. This is two orbits after the particle self-gravity term is introduced. The most dense particle structures appear to preferentially form from the rings which develop around vortices.*

the gaseous component of the disc. These vortices tend to associated with spiral density waves, forming along shock fronts in the disc. The dust particles in the sheet become trapped inside of the spiral density waves through as outlined in Chapter 3. Within the spiral density waves, the strongest particle concentrations tend to form around anticyclonic vortices, forming spiral or ring like structures around the vortex, with very few particles drawn into the core of the vortices. This is an important difference from the vortex properties in non self-gravitating discs, where dust particles are tightly concentrated in the centre of the vortex. When the self-gravity of the solid component of the disc is introduced the over densities that form around vortices are the first to undergo gravitational collapse and rapidly reach densities hundreds of times larger the the local gas density.

The picture of planetesimal formation built up by Chapters 3 and 4 is still an attractive method for the rapid creation of a reservoir of planetesimals, along with several very massive objects of $\sim 1\% M_{Earth}$, which are likely to continue to grow via the accretion of smaller bodies, potentially reaching terrestrial planet masses. Based on the results obtained in this Chapter, planetesimals formation can still rapidly take place within spiral density waves, however it appears that it will preferentially take place around anticyclonic vortex sub-structure present in and around density waves.

Chapter 6

3D Shearing Boxes

The work presented in this Chapter is ongoing. This Chapter describes the current progress made.

6.1 Introduction

The work presented in previous Chapters has modelled accretion discs as two-dimensional shearing sheets. Although current theory suggests that this two-dimensional case is a good approximation of the fully three-dimensional case (Mamatsashvili & Rice, 2010), and is much easier to model due to the significant reduction in computation time, it is impossible to gain a complete picture of planet formation in discs without extending this study to include the vertical component of the disc.

In the previous chapters studying discs in two-dimensions, the stability of the disc against axisymmetric perturbations due to self-gravity is governed by the Toomre Q-parameter,

$$Q_{2D} \equiv \frac{c_s \Omega}{\pi G \Sigma}, \tag{6.1}$$

where Ω is the angular velocity of the disc and Σ is the local surface density of the disc. If Q drops below a certain value $Q_{crit} \sim 1$, then the disc will become

unstable (Toomre, 1964), possibly resulting to the disc fragmenting or density waves forming depending on the thermal properties of the disc (Gammie, 2001; Rice et al., 2003). The three dimensional analogue of this parameter is defined as,

$$Q_{3D} \equiv \frac{\Omega^2}{4\pi G \rho_m}, \tag{6.2}$$

which is obtained (within numerical factors) by taking the density at the mid plane, $\rho_m = \Sigma/h$, where h is the scale height of the disc.

Numerical simulations of self-gravitating discs have generally studied discs in one of two settings, in the local 'shearing sheet' model, such as those presented in previous chapters, the small scale of the simulation domain allows small scale perturbations to be investigated, as previously noted though, these simulations are two-dimensional, with the vertical modes of any perturbations neglected, and physical quantities vertically averaged over the disc. Stability analysis in three dimensions proves to be more complicated than the two dimensional case. Vertical structure in the disc arises from the self-gravity of the disc and the vertical component of the gravitational potential of the central object. Depending on the nature of the vertical stratification, there can be a wide range of modes which exist in three-dimensions which do not exist in two-dimensions. Some of these modes can become unstable on length scales comparable to the disc thickness. In this case the vertical structure of the disc must be taken into account. Global simulations of discs, (e.g. Rice et al., 2003; Lodato & Rice, 2004; Rice et al., 2004, 2006) using smooth particle hydrodynamics (SPH) usually model the disc in three dimensions, however lack the required resolution to fully capture vertical structure within the disc.

The local, three-dimensional, 'shearing box' can allow these small scale vertical motions to be studied, and been utilised to study planet formation in non-self gravitating discs, where the main source of turbulence is the magneto-rotational instability (MRI) (e.g. Johansen et al., 2007, 2011). Here the shearing box is adapted to model gravitational instabilities in discs, and the role these instabilities can play in the planet formation process. Of particular interest, especially in regards to the work presented in this thesis, is the effect of the vertical structure on the fragmentation boundary within the disc, along with the effect the vertical

structure of the gas has on the evolution of the dust within the disc. Both of these can potentially yield a more complete picture of the planet formation process with discs.

This Chapter outlines the differences between the two-dimensional and three-dimensional cases, along with the changes required to the PENCIL code setup to conduct three-dimensional simulations. The current progress of these simulations is also described, along with issues which still need to be addressed.

6.2 Model

In order to model accretion discs in a three-dimensional shearing box, the PENCIL codes used to solve the hydrodynamical equations for the gas on a fixed grid, along with the Poisson equation to describe the discs self-gravity. Dust particles are evolved using the same equations of motion described in previous chapters, however the solids are now free to move in the z direction, as well as the x and y dimensions. In the shearing box, disc dynamics is modelled in the local Cartesian coordinate frame centred at some arbitrary radius, r_0, from the central object and rotating with the disc's angular frequency, Ω, at this radius. In this local frame, the x-axis points radially away from the central object, the y-axis points in the azimuthal direction of the disc's differential rotation, which in turn manifests itself as an azimuthal parallel flow characterised by a linear shear, q, of background velocity, $\mathbf{u}_0 = (0, -q\Omega x, 0)$. The z axis points vertically out of the disc. The simulation domain spans the region $-L_x/2 \leq x \leq L_x/2$, $-L_y/2 \leq y \leq L_y/2$,$-L_z/2 \leq z \leq L_z/2$. The standard shearing-sheet boundary conditions are for any variable f we have

$$f(x, y, z, t) = f(x, y + L, z, t) \tag{6.3}$$

$$f(x, y, z, t) = f(x + L, y - q\Omega Lt, z, t). \tag{6.4}$$

The z boundary is free, allowing material to flow out the top and bottom of the simulation domain. These boundary conditions apply to all grid variables except

the azimuthal component of the velocity, u_y, which must be adjusted to account for the relative shear between neighbouring boxes. The azimuthal velocity on the radial boundary is,

$$v_y(x, y, z, t) = v_y(x + L, y - q\Omega Lt, z, t) + q\Omega L. \tag{6.5}$$

The shear parameter $q = 1.5$ for Keplarian rotation profile adopted in this paper.

6.2.1 Gas Density

In this local model, the continuity equation for the gas volume density ρ is

$$\frac{\partial \rho}{\partial t} + \nabla.(\rho \mathbf{u}) - q\Omega x \frac{\partial \rho}{\partial y} + f_D(\rho) = 0 \tag{6.6}$$

where $\mathbf{u}(u_x, u_y, u_z)$ is the gas velocity relative to the background Keplerian flow, which in our domain manifests itself as an azimuthal flow with linear shear of velocity $\mathbf{u}_0 = (0, -q\Omega x, 0)$. Due to the high-order numerical scheme of the PENCIL code a diffusion term, f_D, is introduced to ensure numerical stability and capture the effects of shocks. If the length of the z domain, L_z is sufficiently large, near the top and bottom of the box, the density can reach very low values that can cause numerical instabilities to develop and propagate throughout the simulation, potentially causing it to crash. In order to minimise these effects a minimum density of $\rho_{min} = 10^{-2}\rho_0$ is imposed throughout the box.

6.2.2 Gas Velocity

The equation of motion for the gas velocity $\mathbf{u}$ relative to the background Keplerian flow $\mathbf{u}_0$ takes the form

$$\begin{aligned}\frac{\partial \mathbf{u}}{\partial t} + (\mathbf{u} \cdot \nabla)\mathbf{u} - q\Omega x \frac{\partial \mathbf{u}}{\partial y} = &-\frac{\nabla P}{\rho} - 2\Omega \hat{\mathbf{z}} \times \mathbf{u} + q\Omega u_x \hat{\mathbf{y}} - \Omega^2 z \hat{\mathbf{z}} \\ &+ 2\Omega \Delta v \hat{\mathbf{x}} - \frac{\rho_p/\rho}{\tau_f}(\mathbf{u} - \mathbf{v}) - \nabla\psi + \mathbf{f}_\nu(\mathbf{u}),\end{aligned} \tag{6.7}$$

where P is the pressure and ψ is the gravitational potential of the gas due to the density perturbation $\rho - \rho_0$. The left hand side of equation 6.7 includes terms from the velocity field $\mathbf{u}$ and the Keplerian flow. The first term on the right hand side of the equation is the force due to the pressure gradient. The second and third terms represent the Coriolis effect/shear induced by the choice of coordinate system. The fourth represents the vertical gravity from the central star. The fifth term mimics a global radial pressure gradient, which reduces the orbital speed of the gas by Δv and is responsible for the inward migration/drift of solids in an unperturbed disc. The main purpose for the inclusion of this term here is to see how the radial drift affects the concentration of particles by spiral density waves. The sixth term describes the drag force exerted on the gas by the dust particles. The seventh term represents the effect of the gravitational potential of the disc. Finally an explicit viscosity term, $\mathbf{f}_\nu$, is included which contains both Navier-Stokes viscosity and a bulk viscosity for resolving shocks.

6.2.3 Entropy

The PENCIL CODE uses entropy, s, as its main thermodynamic variable, rather than internal energy, U, as used by Gammie (2001). The equation for entropy evolution is

$$\frac{\partial s}{\partial t} - q\Omega x\frac{\partial s}{\partial y} + (\mathbf{u}.\nabla)s = \frac{1}{\rho T}\left(2\rho\nu\mathbf{S}^2 - \frac{\rho c_s^2}{\gamma(\gamma-1)t_c} + f_\chi(s)\right) \tag{6.8}$$

where the first term on the right hand side is the viscous heating term and the second term is an explicit cooling term. Here we assume the cooling time t_c to be constant throughout the sheet and take its value to be sufficiently large that the disc does not fragment and achieves a quasi-steady state. The final term on the right hand side, $f_\chi(s)$, is a shock dissipation to maintain stability across shock fronts.

6.2.4 Self-gravity

The gravitational potential terms in equations 6.7 and 4.8 are calculated by inverting the Poisson equation,

$$\nabla^2\psi = 4\pi G\rho' \tag{6.9}$$

using the Fast Fourier Transform method outlined in outlined in Chapter 2. In equation 6.9 the density ρ' represents either the perturbed gas surface density $\rho - \rho_0$ or the particle surface density ρ_p. This Fourier transform technique raises a potential problem due to the periodic nature of the poison solver. The three-dimensional shearing box assumes periodic boundaries in both the x and y directions, as in the two dimensional case, however the introduction of the vertical structure poses a problem for the fully periodic poisson solver employed here, as the z axis is not periodic. Johansen et al. (2007) addressed this in the supplementary material of their paper, where they adopted the fully periodic Poisson solver to study the gravitational collapse of over dense regions of the solid part of the disc produced by MRI turbulence. They performed tests on the simple case of a system of self-gravitating gas, collapsing in one dimension along the z axis. They found that the numerical solution obtained by the PENCIL code was in good agreement with that predicted by analytic theory for high-to medium density region i.e. near the mid plane of the disc, however due to the periodic nature of the simulation began to disagree for the low density regions near the top and bottom of the box. They found that significant deviations from the analytic result due to the periodic nature of the Poisson solver occurred for $|\mathbf{z}| > 2h$. This behaviour is naturally also present in the simulations presented here, however can be more difficult to manage when considering both the gas and dust as self gravitating as discussed in Section 6.3.

6.2.5 Units and Initial Conditions

We normalise our parameters by setting $c_{s,0} = \Omega = \rho_0 = 1$. The time and velocity units are $[t] = \Omega^{-1}$ and $[v] = c_{s,0}$, resulting in the orbital period, $T = 2\pi$. The unit of length is the scale height, $[l] = h = c_{s,0}/\Omega$. We initialise the Toomre-Q

parameter to be 1 in the mid plane of the sheet. This sets the gravitational constant $G = \pi^{-1}$. The gas is initially distributed as a gaussian along the z axis. The box is of length $L_{x,y} = 40G\Sigma/\Omega^2$ in the x and y directions and $L_z = 10G\Sigma/\Omega^2$ in the z direction is divided into a grid of $512 \times 512 \times 128$ cells. The gas velocity field is initially perturbed by some small random fluctuations with the rms amplitude $\sqrt{< \delta \mathbf{v}^2 >} = 10^{-3}$. We take the viscosity and diffusion coefficients to be $\nu = 10^{-2}$ and $\nu_{sh} = D_{sh} = 5.0$.

6.3 Progress to Date

The bulk of the progress to date has revolved around setting up the simulations and getting them to run stably. The major changes introduced in tube shearing box formalism outlined in section 6.2 (other than replacing two dimensional variables with their three-dimensional counterpart) occur in the treatment of the gas density and the gas velocity. The treatment of the gas velocity includes an additional term to account for the vertical component of the central objects gravity. The initial runs performed simply introduced the z component of the disc, no longer treating it as razor-thin. This however created instabilities in the simulations, which resulted in the run either experiencing impractically small timesteps, or outright crashes, depending on the size of the z-domain. These instabilities tend to originate at the top and bottom of the box (high $|z|$) and propagate through the box over time. The instabilities tend to originate from the pressure term involving ρ^{-1} in the gas velocity equation. At high $|z|$, the densities reach very small values as the gas contracts toward the mid plane during the initial burst phase, causing the velocities to increase. In order to prevent these instabilities from arising, a minimum density, ρ_{min}, is imposed throughout the box. Although several values of ρ_{min} are tested, a value of $\rho_{min} = 10^{-2}\rho_0$ appears to be the minimum value of density which can prevent instabilities and allow the code to run.

The current output of these simulations are illustrated in Figures 6.1 - 6.2. These Figures show the surface density off the tax in the box, along with $x - z$ and $y - z$ cross sections of the box, showing the vertical profile of the gas. The first

three figures show the structure of the gas for a box with $t_c = 3\Omega^{-1}$, whilst the second takes $t_c = 10\Omega^{-1}$. The z averaged surface densities of the gas show that the general behaviour of the gas is similar to the two-dimensional case, the short cooling time considered is undergoing fragmentation, whilst the longer cooling time settles into a quasi steady state, forming density waves.

The major obstacle to the progress of this work is evident from the cross sections showing the vertical profile of the gas. Due to the periodic nature of the poisson solver, the disc structure tends to be artificially extended in z due to the self-gravity of the repeated images of the disc above and below the simulation domain. Near the mid plane, these effects are minimal, as the periodic repetition of the disc above and below the box tend to cancel out, and are small due to the separation between the two discs being large. At the top and bottom of the disc these effects become much more pronounced, and if sufficient material reaches the extremities of the z domain, its evolution becomes dominated by artificial effects arising from the periodic poisson solver.

The current goal of this work is to find a simulation domain and resolution which allows the simulations to run, with the majority of the material remaining near the centre of the domain where numerical effects are minimal, for a range of cooling times. As the vertical profile of the gas alters for different cooling times any domain adopted must be able to contain the most vertically extended profile, as altering the simulation domain for different cooling times adds an additional layer of complexity when comparing simulations.

Once an acceptable set of simulation parameters has been identified, there are many properties of self-gravitating discs which can go on to be studied in three dimensions. Other than the obvious investigation of the vertical profile of the disc, several disc properties which have been extensively studied in the two-dimensional case can be explored in three-dimensions. The fragmentation condition and angular momentum transport capabilities of the disc are of great interest to the community at present. For the work presented in this thesis, the introduction of dust particles, their evolution in three-dimensions, and the influence vertical structure in the disc has on the planet formation process is of particular interest.

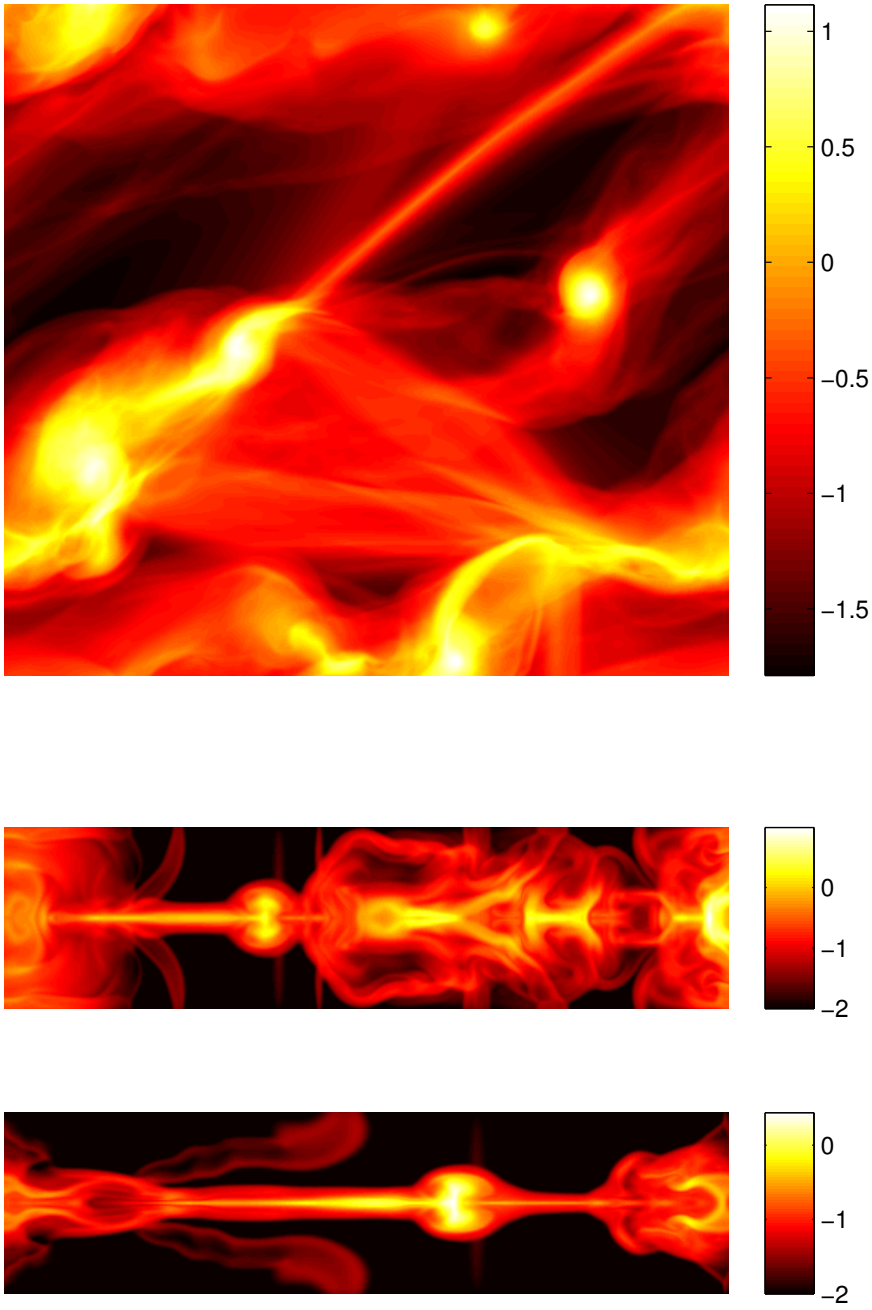

Figure 6.1 *Surface density of the gas in the $t_c = 3\Omega^{-1}$ simulation. The top image shows the $x-y$ plane averaged over z, whilst the bottom two images show $x-z$ and $y-z$ cross-sections.*

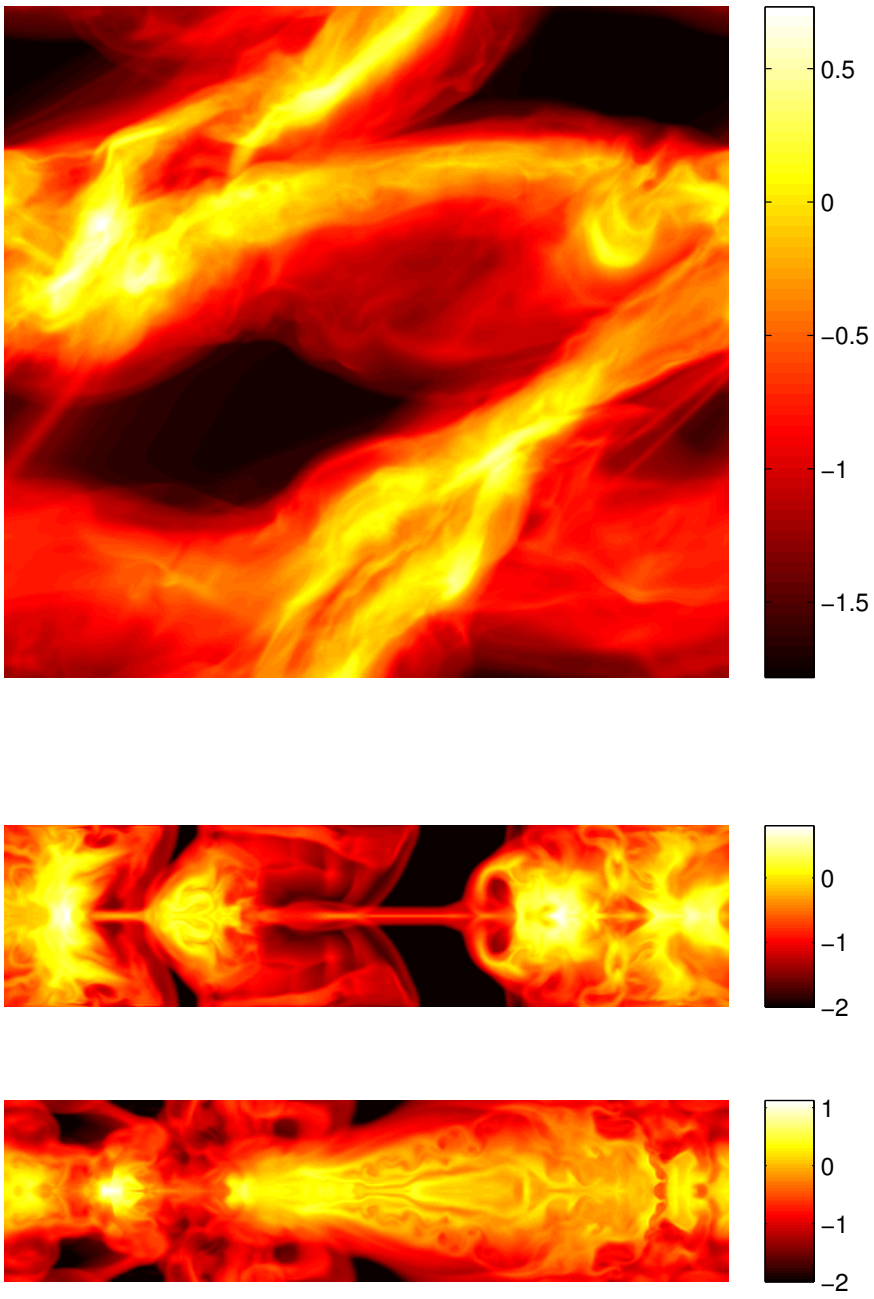

Figure 6.2 *Surface density of the gas in the $t_c = 10\Omega^{-1}$ simulation. The top image shows the $x-y$ plane averaged over z, whilst the bottom two images show $x-z$ and $y-z$ cross-sections.*

Chapter 7

Conclusion & Discussion

As outlined in Chapter 1, the field of planet formation is currently divided into two models which strive to explain the formation of giant planets, the core accretion model, which proposes giant planets form from a core of solid material. Once this solid core reaches a critical mass, ($\sim 10 M_{Earth}$), it begins to slowly accrete gas from the disc onto it's surface, until the accreted envelopes mass is approximately equal to the core's mass, at which point runaway accretion occurs until the disc becomes locally depleted of material. The disc fragmentation model posits that instabilities which develop in massive discs due to their self-gravity can result in the disc breaking apart if the cooling time of the disc is short. The currently favoured theory is the core accretion theory, as it is currently though that the cooling times required for fragmentation are only present at high radii, which struggles to explain the large population of gas giants at extremely small orbital radii (so called 'Hot Jupiter's').

The work presented in this thesis attempts to resolve several outstanding problems with the core accretion model outlined in Chapter 1. The classic core accretion calculation performed by Pollack et al. (1996) outlined the three stage process detailed above. This calculation found that the core accretion process can produce Jupiter mass planets at $\sim$ 5AU in a MMSN over a period of 1-10Myr. This is consistent with typical disc lifetimes, however this calculation assumed the solid component of the disc was a pre-existing reservoir of planetesimal

sized objects, and did not address the problems that arise in the planetesimal formation process. The planetesimal formation process must therefore be rapid for two reasons. For the Pollack et al. (1996) calculation to hold weight, the assumed reservoir of planetesimals must form rapidly, otherwise the disc is likely to dissipate before giant planets are able to form. In addition to this the growth of solid objects from dust grains to planetesimals must be rapid to avoid the rapid infall of intermediate-sized solid objects previously shown. The work performed here provides a possible solution to these problems by demonstrating that whilst the disc is self-gravitating, perturbations due to gravitational stabilities can concentrate particles in density perturbations, allowing the rapid formation of planetesimal sized objects. Chapter 3 showed that dust particles become trapped within a quasi-steady gaseous spiral structure produced by a combined effect of disc self-gravity and cooling. In this case the dust particles' evolution is purely governed by their coupling to the gas via aerodynamic drag. Due to the structure in the gas, the surface density of the solids is locally enhanced depending on the friction time (size) of the particles, and the magnitude of the perturbations in the gas, which is governed by the cooling time of the gas. Dust grains with friction time $\tau_f \sim 1.0\Omega^{-1}$ exhibit the largest concentration in density waves. When this is translated in terms of particle size we find that grain sizes which experience the largest density enhancements depend on the radius in the disc, with larger particles more efficiently trapped at inner radii and smaller at outer radii.

The work performed in Chapter 3 adopted massless 'tracer' particles, in an effort to understand the general behaviour of dust particles without specifying conditions present in a given disc, namely the mass ratio of solids to gas. However the dust in certain cases can reach very high concentrations, the surface density of the dust locally reaching that of the gas for typical dust-to-gas mass ratios ($\Sigma_p/\Sigma_g \sim 10^{-2}$). At this stage it is no longer appropriate to treat the particles as massless, as the particles evolution may become dominated by their own self-gravity, and the back reaction of particles on the gas cannot be neglected either. It is these limitations that prompted the work discussed in Chapter 4. Here the evolution of the particles is explored for massive particles for both a typical disc, ($\Sigma_p/\Sigma_g = 10^{-2}$), as well as a low mass case ($\Sigma_p/\Sigma_g = 10^{-3}$).

Chapter 4 showed that the introduction of the term modelling particle self-gravity

can have several significant effects on the evolution of the disc. The magnitude of these effects depend on the strength of self-gravity within the simulation. In the low mass case where $\Sigma_p/\Sigma_g = 10^{-3}$, the inclusion of the particles self-gravity does not appear to significantly alter the evolution of the solids in the disc from the massless case considered in Chapter 3. In the other case with $\Sigma_p/\Sigma_g = 10^{-2}$, the inclusion of the self-gravity term results in the accumulation of particles which form in spiral density waves contracting further along the crests of the density waves, eventually forming bound clumps of particles. Assuming typical disc parameters, these structures contain a large proportion of the intermediate sized particles, and typically reach masses comparable to large planetesimals. This mechanism provides a method though which the above shortcomings of the core accretion theory can be addressed. In the early stages of the star formation process, whilst the disc is still massive compared to the central star and therefore self-gravitating dust particles can become trapped in spiral density waves in the disc. These local pressure maxima associated with density waves can prevent particles from the rapid inward radial drift that particles experience due to the global pressure gradient within the disc, thus avoiding the loss of solid material due to accretion onto the central object. The concentration of particles within spiral density waves also results in the rapid formation of planetesimal sized objects, typically over a period of ~ 10 orbital periods. For the range of orbital radii considered, this corresponds to a time period of ~ 1000 years, allowing for the formation of gravitationally bound planetesimal mass structures whilst the disc is still self-gravitating. This rapid formation of planetesimals allows for a large reservoir of planetesimals such that assumed by Pollack et al. (1996) to form in a sufficiently short time for the subsequent phases of the core accretion process to proceed within disc lifetimes.

The work presented in Chapter 5 expanded on the results of the first two chapters by studying the particles evolution on smaller scales, using higher resolution simulations. In this regime, small scale structures in the gas emerge, of which anti-cyclonic vortices appear to have the greatest influence on the evolution of the dust particles. These structures tend to result in additional concentration of dust particles in small scale regions within the spiral density waves, further aiding the formation of planetesimal structure within the density waves.

The work presented in this thesis appears to fit into the wider picture of planet formation as follows: In the early stages of the star formation process, whilst the disc is still a sizeable fraction of the stars mass gravitational instabilities tend to result in the formation of density waves in the disc. These density waves are highly efficient at trapping solid objects, the size of which is typically $\sim$ 1m, however the exact size of the particles most effectively trapped depends on the conditions in the disc. Within a given spiral density wave,smaller dust particles tend to gather most effectively around sub structure in the gas, namely regions of negative potential vorticity corresponding to anti-cyclonic vortices. As smaller grains tend to be trapped more effectively at larger radii, this can lead to continual growth as grains secularly migrate inward as a result of drag forces from the gas. Small grains initially at large radii ($\geqslant$ 60AU) can become trapped in density waves and grow through collisions with other particles. This process can continue until the grains reach sizes larger than the optimally trapped size range ($\tau_f \sim 1.0\Omega^{-1}$). At this point a gas over-density can no longer prevent particles from drifting inwards and they start to slowly move inward in the next optimally trapped size range at smaller radii, where they will undergo further rapid growth. If the ratio of dust to gas is sufficiently high, it is likely that the accumulation of solids within spiral density waves will be efficient enough to result in the gravitational collapse of the solid component of the disc, especially around vortex substructure, where the concentration of particles is highest. This process tends to result in a large proportion of smaller solid particles present in the outer regions of the disc ($>$ 10AU) becoming concentrated in gravitationally bound structures over periods of $\sim 10^4 - 10^5$ years, whilst the disc is still in the Class 0/Class I stage. Through this mechanism a large reservoir of planetesimals can form at high radii, subsequently growing to form terrestrial and gas giant planets. Through the migration processes discussed in Chapter 1, these planetesimals and planets can go on to propagate the inner regions of the disc, complementing any mechanisms which dominate the planet formation process at these radii.

Future Work

The next main area of investigation currently being pursued in outlined in Chapter 6. The 3D self-gravitating shearing box presents an opportunity investigate the vertical structure of the disc, and that the effect that vertical modes can have on both the evolution of the disc and the planet formation process. Of particular interest to the work contained in this thesis would be an exploration of the fragmentation condition and the evolution of vortices in the full 3D case, as well as a study of the vertical behaviour of the particles and the effect this has on grain growth and planetesimal formation.

Another interesting area of study would be to investigate the long term evolution of the large accumulations of particles. The current formalism allows for the evolution of particles to be understood until they are gravitationally bound, however as noted in Chapter 5, continues to treat large particle accumulations as an aggregation of smaller particles, and has no means of truly modelling the growth of large solids. By introducing a routine to replace these aggregations with a single objects, which interacts with the gas as a planetesimal should do, the evolution of these large objects can be better understood. By allowing for the creation of these large objects, the later 'oligarchic' growth stage, where terrestrial planets grow via constructive collisions between planetesimals, and even the accretion of gas from the disc onto the planets surface can be modelled and investigated.

Finally, the processes studied here tend to be confined to the outer regions of the disc, at radii less than $\sim$ 10AU, the cooling time of the disc tends to rapidly increase, resulting in the structure associated with gravitational instability becoming far less robust. At this point in the disc, gravitational instabilities cease to dominate the evolution of the disc, and other processes such as MRI begin to play a greater role. Investigating the evolution of the disc at these transitional radii $\sim 5 - 10$AU could yield interesting information about planet formation in the inner regions of the disc, in particular the ability for interior planets to form in situ, rather than migrate inward in the later stages of their evolution.

Bibliography

Andrews S., Williams J., 2005, The Astrophysical Journal, 631, 1134

Andrews S., Wilner D., Hughes A., Qi C., Dullemond C., 2010, The Astrophysical Journal, 723, 1241

Andrews S. M., Williams J. P., 2007, The Astrophysical Journal, 671, 1800

Andrews S. M., Wilner D. J., Hughes A. M., Qi C., Dullemond C. P., 2009, The Astrophysical Journal, 700, 1502

Armitage P. J., 1998, The Astrophysical Journal, 501, L189

Armitage P. J., 2010, Cambridge University Press, Cambridge, UK

Armitage P. J., 2011, Annual Review of Astronomy and Astrophysics, 14, 195

Bai X., Stone J., 2010, The Astrophysical Journal Supplements, 190, 297

Balbus S., Hawley J., 1991, The Astrophysical Journal, 376, 214

Barge P., Sommeria J., 1995, Astronomy & Astrophysics, 295, L1

Beckwith S. V. W., Sargent A. I., 1991, The Astrophysical Journal, 381, 250

Bodo G., Chagelishvili G., Murante G., Tevzadze A., Rossi P., Ferrari A., 2005, Astronomy & Astrophysics, 437, 9

Bondi H., 1952, Monthly Notices of the Royal Astronomical Society, 112, 195

Boss A., 1998, Nature, 393, 141

Brandenburg A., 2003, Advances in Nonlinear Dynamos, p. 269

Brandenburg A., Nordlund A., Stein R. F., Torkelsson U., 1995, The Astrophysical Journal, 446, 741

Chandrasekhar S., 1960, Proceedings of the National Academy of Science, 46, 253

Clarke C. J., 2009, Monthly Notices of the Royal Astronomical Society, 396, 1066

Clarke C. J., Lodato G., 2009, Monthly Notices of the Royal Astronomical Society, 398, L6

Cossins P., Lodato G., Clarke C., 2009, Monthly Notices of the Royal Astronomical Society, 396, 1157

Eisner J., Hillenbrand L., Carpenter J., Wolf S., 205, The Astrophysical Journal, 635, 396

Forgan D. H., Rice W. K. M., Cossins P., Lodato G., 2011, Monthly Notices of the Royal Astronomical Society, 410, 994

Gammie C., 2001, The Astrophysical Journal, 553, 174

Gibbons P., Rice W., Mamatsashvili G., 2012, Monthly Notices of the Royal Astronomical Society, 426, 1444

Godon P., Livio M., 2000, The Astrophysical Journal, 537, 396

Goldreich P., Lynden-Bell D., 1965, Monthly Notices of the Royal Astronomical Society, 130, 97

Goldreich P., Tremaine S., 1978, The Astrophysical Journal, 222, 850

Goodman A., Benson P. J., Fuller G. A., Myers P., 1993, The Astrophysical Journal, 406, 528

Greaves J., Rice W., 2010, Monthly Notices of the Royal Astronomical Society, 407, 1981

Haisch K., Lada E., Lada C., 2001, The Astrophysical Journal, 552, L153

Hartmann L., Calvet N., Gullbring E., DAlessio P., 1998, The Astrophysical Journal, 495, 385

Hartmann L., DAlessio P., Calvet N., Muzerolle J., 2006, The Astrophysical Journal, 648, 484

Hawley J. F., 2001, The Astrophysical Journal, 554, 534

Hawley J. F., Gammie C. F., Balbus S. A., 1995, The Astrophysical Journal, 440, 742

Hayashi C., 1981., Progress of Theoretical Physics Supplement, 70, 35

Hughes A. M., Wilner D. J., Qi C., Hogerheijde M. R., 2008, The Astrophysical Journal, 678, 1119

Ida S., Lin D., 2004, The Astrophysical Journal, 616, 567

Ikoma M., Nakazawa K., Emori H., 2000, The Astrophysical Journal, 537, 1013

Isella A., Carpenter J., Sargent A., 2009, The Astrophysical Journal, 701, 260

Isella A., Testi L., Natta A., Neri R., Wilner D., Qi C., 2007, Astronomy & Astrophysics, 469, 213

Johansen A., Andersen A. C., Brandenburg A., 2004, Astronomy & Astrophysics, 417, 361

Johansen A., Klahr H., Henning T., 2006, The Astrophysical Journal, 636, 1121

Johansen A., Klahr H., Henning T., 2011, Astronomy & Astrophysics, 529, A62

Johansen A., Oishi J. S., Low M., Klahr H., Henning T., Youdin A., 2007, Nature, 448, 1022

Johansen A., Youdin A., 2007, The Astrophysical Journal, 662, 627

Johnson B., Gammie C., 2003, The Astrophysical Journal, 597, 131

Johnson B. M., Gammie C. F., 2005, The Astrophysical Journal, 626, 978

Klahr H., Bodenheimer P., 2003, Proceedings of the Conference on Towards Other Earths: DARWIN/TPF and the Search for Extrasolar Terrestrial Planets, p. 481

Klahr H., Bodenheimer P., 2006, The Astrophysical Journal, 639, 432

Kokubo E., Ida S., 2002, The Astrophysical Journal, 581, 666

Laibe G., Gonzalez J.-F., Maddison S. T., 2012, Astronomy & Astrophysics, 537, A61

Li H., Colgate S. A., Wendroff B., Liska R., 2001, The Astrophysical Journal, 551, 874

Li H., Finn J. M., Lovelace R. V. E., Colgate S. A., 2000, The Astrophysical Journal, 533, 1023

Lin D. N. C., Pringle J. E., 1987, Monthly Notices of the Royal Astronomical Society, 225, 607

Lin D. N. C., Pringle J. E., 1990, The Astrophysical Journal, 358, 515

Lissauer J., 1993, 31, 129

Lithwick Y., 2007, The Astrophysical Journal, 670, 789

Lodato G., Clarke C. J., 2011, Monthly Notices of the Royal Astronomical Society, 413, 2735

Lodato G., Rice W. K. M., 2004, Monthly Notices of the Royal Astronomical Society, 351, 630

Lovelace R. V. E., Li H., Colgate S. A., Nelson A. F., 1999, The Astrophysical Journal, 513, 805

Lynden-Bell D., Pringle J. E., 1974, Monthly Notices of the Royal Astronomical Society, 168, 603

Lyra W., Johansen A., Khlar H., Piskunov N., 2008, Astronomy & Astrophysics, 479, 883

Lyra W., Johansen A., Zsom A., Klahr H., Piskunov N., 2009, Astronomy & Astrophysics, 497, 869

Machida M. N., Matsumoto T., 2011, Monthly Notices of the Royal Astronomical Society, 413, 2767

Mamatsashvili G. R., Chagelishvili G. D., 2007, Monthly Notices of the Royal Astronomical Society, 381, 809

Mamatsashvili G. R., Rice W. K. M., 2009, Monthly Notices of the Royal Astronomical Society, 394, 2153

Mamatsashvili G. R., Rice W. K. M., 2010, Monthly Notices of the Royal Astronomical Society, 406, 2050

Meru F., Bate M. R., 2011, Monthly Notices of the Royal Astronomical Society, 411, L1

Nakagawa Y., Seika M., Hayashi C., 1986, Icarus, 67, 375

Paardekooper S.-J., 2012, Monthly Notices of the Royal Astronomical Society, 421, 3296

Paardekooper S.-J., Baruteau C., Meru F., 2011, Monthly Notices of the Royal Astronomical Society, 415, L65

Pollack J. B., Hubickyj O., Bodenheimer P., Lissauer J. J., Podolak M., Greenzweig Y., 1996, Icarus, 124, 62

Rafikov R. R., 2005, The Astrophysical Journal, 621, L69

Rice W. K. M., Armitage P., Mamatsashvili G., Lodato G., Clarke C., 2011, Monthly Notices of the Royal Astronomical Society, 418, 1356

Rice W. K. M., Armitage P. J., 2009, Monthly Notices of the Royal Astronomical Society, 396, 2228

Rice W. K. M., Armitage P. J., Bate M. R., Bonnell I. A., 2003, Monthly Notices of the Royal Astronomical Society, 338, 227

Rice W. K. M., Forgan D. H., Armitage P. J., 2012, Monthly Notices of the Royal Astronomical Society, 420, 1640

Rice W. K. M., G. L., Pringle J. E., Armitage P. J., Bonnell I. A., 2004, Monthly Notices of the Royal Astronomical Society, 355, 543

Rice W. K. M., G. L., Pringle J. E., Armitage P. J., Bonnell I. A., 2006, Monthly Notices of the Royal Astronomical Society, 372, L9

Rodriguez L., Loinard L., DÁlessio P., Wilner D., Ho P., 2005, The Astrophysical Journal, 621, L133

Safronov V. S., 1960, Soviet Physics Doklady, 5, 13

Shakura N., Sunyaev R., 1973, Astronomy & Astrophysics, 24, 337

Toomre A., 1964, The Astrophysical Journal, 139, 1217

Velikhov E. P., 1959, Journal of Experimental Theoretical Physics (USSR), 36, 1398

Weidenschilling S., 1977, Monthly Notices of the Royal Astronomical Society, 180, 57

Whipple F., 1972, From Plasma to Planets. Wiley, London, p. 211

Youdin A., Johansen A., 2007, The Astrophysical Journal, 662, 613

Zhu Y., Hartmann L., Gammie C., 2009, The Astrophysical Journal, 694, 1045